STRUCTURE-PROPERTY RELATIONSHIPS IN MIXED-METAL OXIDES AND

(OXY)HYDROXIDES FOR ENERGY APPLICATIONS

by

LISA J. ENMAN

A DISSERTATION

Presented to the Department of Chemistry and Biochemistry
and the Graduate School of the University of Oregon
in partial fulfillment of the requirements
for the degree of
Doctor of Philosophy

September 2018

DISSERTATION APPROVAL PAGE

Student: Lisa J. Enman

Title: Structure-Property Relationships in Mixed-Metal Oxides and (Oxy)Hydroxides for Energy Applications

This dissertation has been accepted and approved in partial fulfillment of the requirements for the Doctor of Philosophy degree in the Department of Chemistry and Biochemistry by:

Catherine Page	Chairperson
Shannon Boettcher	Advisor
Georgy Nazin	Core Member
Benjamin McMorran	Institutional Representative

and

Janet Woodruff-Borden	Vice Provost and Dean of the Graduate School

Original approval signatures are on file with the University of Oregon Graduate School.

Degree awarded September 2018

DISSERTATION ABSTRACT

Lisa J. Enman

Doctor of Philosophy

Department of Chemistry and Biochemistry

September 2018

Title: Structure-Property Relationships in Mixed-Metal Oxides and (Oxy)Hydroxides for Energy Applications

Metal oxides and (oxy)hydroxides, particularly those containing two or more metals have many uses as electronic materials and catalyst, especially in energy applications. In this dissertation, the structure-property relationships of these mixed-metal materials are explored in order to understand how these materials work and to guide design of materials with even higher efficiency for a given application. Chapter I introduces the materials and studies undertaken. Chapter II presents a fundamental analysis of the electronic and local atomic properties of mixed-transition-metal aluminum oxide thin films.

The final three chapters focus on water electrolysis for hydrogen production, which is limited in part by the slow kinetics of the oxygen evolution reaction (OER). Nickel-iron and cobalt-iron (oxy)hydroxides have been shown to be the most active in alkaline conditions. Although it is evident that Fe is essential for high activity, its role is still unclear. Chapter III investigates the role of Fe in NiOOH by comparing the effects of Ti, Mn, La, and Ce incorporation on the OER activity of NiOOH in base. Chapter IV evaluates the OER activity and Tafel behavior of Fe^{3+} impurities on different noble metal substrates. Chapter V describes the results of in situ and in operando X-ray spectroscopy

experiments, which shows that the local structure around Fe atoms in Co(Fe)OOH changes during OER while that of Co stays the same. This work adds to the growing body of literature that suggests Fe is essential to the catalytic active site for the OER on transition-metal (oxy)hydroxides.

This dissertation contains previously published and un-published coauthored material.

CURRICULUM VITAE

NAME OF AUTHOR: Lisa J. Enman

GRADUATE AND UNDERGRADUATE SCHOOLS ATTENDED:

University of Oregon, Eugene
Worcester State University, Worcester, Massachusetts
Worcester Polytechnic Institute, Worcester, Massachusetts

DEGREES AWARDED:

Doctor of Philosophy, Chemistry, 2018, University of Oregon
Master of Science, Chemistry, 2015, University of Oregon
Bachelor of Science, Chemistry, 2013, Worcester State University

AREAS OF SPECIAL INTEREST:

Materials Chemistry; Electrochemistry; Catalysis

PROFESSIONAL EXPERIENCE:

Research Assistant, Boettcher Laboratory, University of Oregon, 2014-2018

Teaching Assistant, University of Oregon, 2013-2014
    Organic Chemistry Lab, General Chemistry Lab, General Chemistry Lecture

LEADERSHIP EXPERIENCE:

Executive Board, Women in Graduate Science, University of Oregon, 2016-2018
    Treasurer, Public Relations Chair

Peer-elected Representative, Chemistry and Biochemistry Graduate
Representative Advisory Team, University of Oregon, 2016-2017

Laboratory Safety Officer, Boettcher Lab, University of Oregon, 2015-2017

PUBLICATIONS:

10) Enman, L. J.; Kast, M. G.; Cochran, E. A.; Pledger, E.; Stevens, M. B.; Boettcher, S. W. Transition-Metal-Incorporated Aluminum Oxide Thin Films: Towards Electronic Structure Design in Amorphous Mixed-Metal Oxides. *J. Phys. Chem. C.* **2017**, **DOI:** 10.1021/acs.jpcc.8b00239

9) Cochran E. A.; Park D. H.; Kast M. G.; Enman L. J.; Perkins, C. K.; Mansergh, R. H.; Keszler, D. A.; Johnson, D. W.; Boettcher S. W. Role of Combustion Chemistry in Low-Temperature Deposition of Metal Oxide Thin Films from Solution. *Chem. Mater.* **2017**, *29*, 9480-9488.

8) Woods, K.N.; Plassmeyer, P.N.; Park, D.H.; Enman, L.J.; Grealish, A. K.; Kirk, B. L.; Boettcher, S. W.; Keszler, D. A.; Page, C.J. Low-Temperature Steam Annealing of Metal Oxide Thin Films from Aqueous Precursors: Enhanced Counterion Removal, Resistance to Water Absorption, and Dielectric Constant. *Chem Mater.* **2017**, *29*, 8531-8538.

7) Stevens, M.B.; Trang, C.D.; Enman, L. J.; Deng, J; Boettcher, S. W. Reactive Fe-sites in Ni/Fe (oxy) hydroxide are responsible for exceptional oxygen electrocatalysis activity. *J. Am. Chem. Soc.* **2017**, *139*, 11361–11364.

6) Kast, M. G.; Cochran, E. A.; Enman, L.J.; Mitchson, G.; Ditto, J; Siefe, C; Plassmeyer, P. N.; Greenaway, A. L.; Johnson, D. C.; Page, C. J.; Boettcher, S. W. Amorphous Mixed-Metal Oxide Thin Films from Aqueous Solution Precursors with Near Atomic Smoothness. *J. Am. Chem. Soc.* **2016**, *138*, 16800–16808.

5) Stevens, M. B.; Enman, L. J.; Batchellor, A. S.; Cosby, M. R.; Vise, A. E.; Trang, C. D. M.; Boettcher, S. W. Measurement Techniques for the Study of Heterogeneous Water Oxidation Electrocatalysts. *Chem Mater.* **2016**, *29*, 120-140.

4) Enman, L. J.; Burke, M. S.; Batchellor, A. S.; Boettcher, S. W. Effects of Intentionally Incorporated Metal Cations on the Oxygen Evolution Electrocatalytic Activity of Nickel (Oxy)hydroxide in Alkaline Media. *ACS Catal.* **2016**, *6*, 2416-2423.

3) Burke, M. S.; Enman, L. J.; Batchellor, A. S.; Zou, S.; Boettcher, S. W. Oxygen-evolution-reaction electrocatalysis on transition metal oxides and (oxy)hydroxides: Activity trends and design principles. *Chem. Mater.* **2015**, *27*, 7549-7558.

2) Burke, M. S.; Zou, S.; Enman, L. J.; Kellon, J. K.; Gabor, C. A.; Pledger, E.; Boettcher, S. W. Revised oxygen-evolution-reaction activity trends for first-row transition metal (oxy)hydroxides in alkaline media. *J. Phys. Chem Lett.* **2015**, *6*, 3737-3742.

1) Kast, M. G.; Enman, L. J.; Gurnon, N. J.; Nadarajah, A.; Boettcher, S. W. Solution-Deposited F:SnO$_2$/TiO$_2$ as a Base-Stable Protective Layer and Antireflective Coating for Microtextured Buried-Junction H$_2$-Evolving Si Photocathodes. *ACS Appl. Mater. Interfaces* **2014**, *6*, 22830–22837.

ACKNOWLEDGMENTS

To my advisor, Prof. Shannon Boettcher, thank you for your enthusiasm for science and your never-ending supply of ideas. Your high standards have made me a better scientist. Also thank you to my committee, especially Prof. Cathy Page for contributing to my scientific development.

To my undergraduate professors, Prof. Anne Falke, Prof. Eihab Jaber, and Prof. Joseph Quattrucci, thank you for the chemistry education you gave me, for your advice, and for telling me about this thing called grad school and convincing me it was something I could do.

Importantly I would like to thank all Boettcher lab members past and present for their encouragement, but also constructive criticism. Thank you for making the lab feel more like a family. I would particularly like to thank past Team OER members: Dr. Adam Batchellor and Dr. Adam Smith for their thought-provoking conversations, and especially Dr. Michaela Stevens for challenging me scientifically and for your constant positive encouragement. To Dr. Ann Greenaway, thank you for always being available to talk when I needed it. To Lizzie Cochran and Mike Nellist, thank you for maintaining the spirit of the Boettcher lab. To Ashlee Vise, thank you for your hard work, dedication, enthusiasm, and for being a great mentee. And to Dr. Matthew Kast, the best mentor I have had in my science career, and a great friend, words cannot express my gratitude.

I would like to thank my friends for their emotional support. To Ashley Bernier, thank you for moving across the country with me and for all your support, especially at home those first two years. To Susan Cooper, thank you for being my best friend throughout my PhD experience, your support has saved me from falling apart on many occasions. To all the friends I have made here, especially Andrea, Huiying, Loni, Sam, Hillary, Peter, Brandi, and James, thank you for distracting me from the hard times of graduate school. And to those back home, Jamie, Brianna, Melissa, and Callen, thank you for effortlessly continuing our friendship despite my moving 3,000 miles away.

To my sister, Julia, thank you for always being there for me, especially when things in life got difficult. To my aunt Chrissy, thank you for your never-ending support and understanding. To my mother, thanks for pushing me to be better. And to my dad, thank you for everything: for coaching me, for always telling me how smart I am, for understanding who I am and supporting me even when my path got murky.

TABLE OF CONTENTS

LIST OF FIGURES

xv

Figure   Page

LIST OF TABLES

CHAPTER I

INTRODUCTION

Section "Electronic Structure Design in Amorphous Oxides" contains co-authored material previously published as *J. Phys. Chem. C.* **2018**, **DOI:** 10.1021/acs.jpcc.8b00239 reproduced with permission. Copyright 2018 American Chemical Society. Prof. Boettcher, M. Kast, and I conceived of the project. I performed and directed experiments, collected data, and analyzed data with help from M. Kast, E. Cochran, E. Pledger, and M. Stevens. I wrote the paper with help from Prof. Boettcher and M. Kast along with editorial assistance from all authors.

Section "Effects of Transition-Metal Cations on Nickel (Oxy)hydroxide Activity" contains co-authored material previously published as *ACS Catal.* **2016**, *6*(4), 2416-2423 reproduced with permission. Copyright 2016 American Chemical Society. M. Burke and I conceived of the project. I performed the experiments and analyzed data with help from M. Burke and A. Batchellor. I wrote the paper with help from Prof. Boettcher and editorial assistance from all authors.

Section "Metal Electrode Substrate Effects on FeO_xH_y Activity" contains co-authored unpublished material. Prof. Boettcher and I conceived of the project. I performed experiments and analyzed data as well as directed experiments and analysis performed by undergraduate A. Vise. I wrote the paper with help from Prof. Boettcher and A. Vise along with editorial assistance from all authors. It is prepared in the format of the Journal of the American Chemical Society.

Section "The Role of Fe in the Oxygen Evolution Reaction on $Co(Fe)O_xH_y$" contains co-authored unpublished material. M. Stevens, Prof. Boettcher, and I conceived of the project. I performed experiments along with M. Stevens and M. Nellist with technical assistance from S. Fakra. M C. Toroker and M Dahan performed calculations. I analyzed data and wrote most of the paper with computational sections written by M.

1

Toroker and with editorial assistance from M. Stevens and S. Boettcher. It is prepared in the format for submission to the journal Angewandte Chemie International Edition.

Electronic Structure Design in Amorphous Oxides

Amorphous metal oxides have numerous applications spanning from electronics to catalysis. The ability to rationally design the electronic structure of such materials would thus have significant impact. Previous work has shown that the amorphous structure allows for uniformly incorporating a large number of different metal cations into ultra-smooth thin films. Here we investigate how the atomic structure, electronic structure, and optical absorption properties of amorphous aluminum oxide (a-Al_2O_3) thin films are modulated when metal cations of V, Cr, Mn, Fe, Co, Ni, Cu, Zn, or Ga are added to form $M_yAl_{1-y}O_x$ where y varies from 0.1 to 0.7. We use X-ray absorption spectroscopy (XAS) to analyze oxidation state and local bonding around the incorporated cations (e.g. coordination number), valence-band X-ray photoelectron spectroscopy (VB-XPS) to assess the impact of the cations on the valence band electronic structure, and optical absorption spectroscopy to assess the presence and energies of new unoccupied electronic states (schematically depicted in Figure 1.1.). Cations with partially filled d-orbitals (e.g. Fe^{3+}, Cr^{3+}, Co^{2+}, Ni^{2+}, Cu^{2+}, etc.) add filled 3d electronic states at the valence band edge of a-Al_2O_3 as well as unfilled 3d electronic states within the a-Al_2O_3 band gap. Cations with the d^{10} electronic configuration, such as Zn^{2+} and Ga^{3+}, introduce filled 3d electronic states at energies well below the valence band edge in addition to new unfilled electronic states in the a-Al_2O_3 band gap. Cations with unfilled d-orbitals (e.g. those with a d^0 configuration such as V^{5+} and Cr^{6+}) do not modify the valence band of a-Al_2O_3, but affect the optical properties by inserting unfilled 3d electronic states within the band gap. These results provide guidance for the rational design of the electronic structure of amorphous mixed-metal oxides and are discussed further in Chapter II.
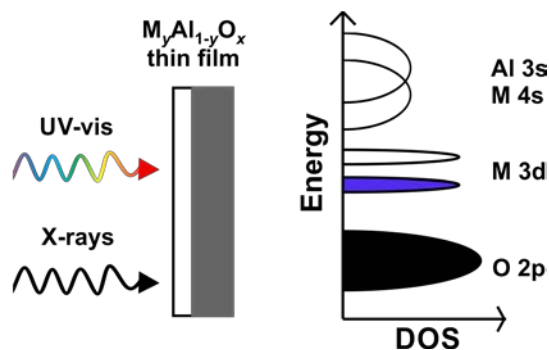
Figure 1.1. Schematic depiction of UV-vis and X-ray spectroscopies used to probe the density of states of transition-metal incorporated aluminum oxide thin films.

Chapter II contains co-authored material previously published as *J. Phys. Chem. C.* **2018**, **DOI:** 10.1021/acs.jpcc.8b00239 reproduced with permission. Prof. Boettcher, M. Kast, and I conceived of the project. I performed and directed experiments, collected data, and analyzed data with help from M. Kast, E. Cochran, E. Pledger, and M. Stevens. I wrote the paper with help from Prof. Boettcher and M. Kast along with editorial assistance from all authors.

Effects of Transition-Metal Cations on Nickel (Oxy)hydroxide Activity

Fe-doped Ni (oxy)hydroxide, $Ni(Fe)O_xH_y$, is one of the most-active oxygen-evolution-reaction (OER) catalysts in alkaline conditions, while Fe-free NiO_xH_y is a poor OER catalyst. One approach to better understand the role of Fe, and enable the design of catalysts with higher activities, is to find other cations that behave similarly and compare the common chemical features between them. In Chapter III, we evaluate the effects of La, Mn, Ce, and Ti incorporation on the OER activity and redox behavior of NiO_xH_y in rigorously Fe-free alkaline solution using cyclic voltammetry and electrochemical quartz-crystal microgravimetry. We use X-ray photoelectron spectroscopy and time-of-flight secondary-ion-mass spectrometry to confirm that measurements are free from relevant levels of trace Fe contamination. We find that only Ce leads to increased activity in NiO_xH_y (about a factor of ten enhancement), but this effect is transient, likely due to phase separation. We further find no clear correlation between activity and the nominal $Ni^{2+/3+}$ redox potential, shown in Figure 1.2, suggesting that the "oxidizing" power of the

3

Ni is not directly correlated with the OER activity. These findings are discussed further in Chapter III highlight the uniqueness of Fe and are consistent with it being the active site in Ni(Fe)O$_x$H$_y$.
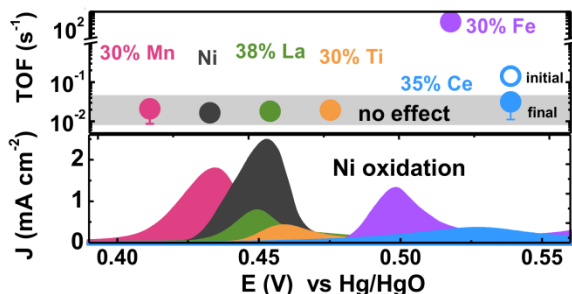
Figure 1.2. Comparison of Ni$^{2+/3+}$ oxidation peak potential and OER turnover frequency (TOF) on Ni$_{1-z}$M$_z$O$_x$H$_y$ thin film electrocatalysts.

Chapter III contains co-authored material previously published as *ACS Catal.* **2016**, *6*(4), 2416-2423 reproduced with permission. M. Burke and I conceived of the project. I performed the experiments and analyzed data with help from M. Burke and A. Batchellor. I wrote the paper with help from Prof. Boettcher and editorial assistance from all authors.

Metal Electrode Substrate Effects on FeO$_x$H$_y$ Activity

FeO$_x$H$_y$ and Fe-containing materials are the some of the most active catalysts for the OER in alkaline solution. However, its activity is highly dependent on the electrode substrate material and/or the elemental composition of the matrix in which it is embedded. A fundamental understanding of these interactions that modulate the OER activity of FeO$_x$H$_y$ is lacking. In Chapter IV, we use cyclic voltammetry and chronopotentiometry to assess the substrate-dependent activity of FeO$_x$H$_y$ on a number of commonly used electrode substrates, Au, Pt, Pd, Cu, and C. We also evaluate the OER activity and Tafel behavior of these metallic substrates in 1 M KOH aqueous solution with Fe^{3+} and other electrolyte impurities. We find that the OER activity of FeO$_x$H$_y$ varies by substrate in the order Au > Pd $\approx$ Pt $\approx$ Cu > C. The trend is likely caused by differences in the adsorption strength of metal-oxo-ion and metallic substrate, where a

stronger adhesion results in decreased charge-transfer resistance at the FeO_xH_y-substrate interface. These results also suggest that the local atomic and electronic structure of $[FeO_6]$ units play an important role in catalysis of the OER as it can be tuned by substrate interactions, and is further discussed in Chapter IV.

Chapter IV contains co-authored unpublished material. Prof. Boettcher and I conceived of the project. I performed experiments and analyzed data as well as directed experiments and analysis performed by undergraduate A. Vise. I wrote the paper with help from Prof. Boettcher and A. Vise along with editorial assistance from all authors. It is prepared in the format of the Journal of the American Chemical Society.

The Role of Fe in the Oxygen Evolution Reaction on $Co(Fe)O_xH_y$

In alkaline conditions, Fe-incorporated Ni- and Co-based (oxy)hydroxides $(Ni(Fe)O_xH_y, Co(Fe)O_xH_y)$ are among the best electrocatalysts for the oxygen evolution reaction (OER). Fe cations are essential for the high activities measured, but the role of Fe in the catalytic mechanism remains controversial. In Chapter V we use operando X-ray absorption spectroscopy (XAS) to demonstrate partial Fe oxidation and a shortening of the Fe-O bond length during oxygen evolution in $Co(Fe)O_xH_y$. Co oxidation is only observed in the absence of Fe. These results support the hypothesis that Fe is the active site in high-activity $Co(Fe)O_xH_y$ OER catalysts, and the partial oxidation is consistent with the idea that only some of the Fe sites are highly reactive. These results are further discussed in Chapter V.

Chapter V contains co-authored unpublished material. M. Stevens, Prof. Boettcher, and I conceived of the project. I performed experiments along with M. Stevens and M. Nellist with technical assistance from S. Fakra. I analyzed data and wrote most of the paper with computational sections written by M. Toroker and with editorial assistance from M. Stevens and S. Boettcher. It is prepared in the format for submission to the journal Angewandte Chemie International Edition.

CHAPTER II

TRANSITION-METAL-INCORPORATED ALUMINUM OXIDE THIN FILMS: TOWARDS ELECTRONIC SRUCTURE DESIGN IN AMORPHOUS MIXED-METAL OXIDES

Introduction

Amorphous and polycrystalline mixed-metal oxides are employed in applications that range from thin-film transistors[1–4] and solar cells,[5,6] to catalysts for reactions including hydrocarbon oxidation,[7–9] hydrogen production via water-splitting,[10] and oxygenate reforming.[11–13] The versatility of mixed-metal oxide materials is due to their wide range of electronic properties, which depend on chemical composition and physical structure (e.g. crystalline vs. amorphous). For example, the band gap of bismuth-containing mixed-transition-metal oxides, used for oxidation catalysis, varies based on the identity of the transition metal(s) due to the dependence of the lowest unoccupied energy levels on empty d-orbitals.[9] Electron-selective contacts to organic photovoltaics have been made by tuning the conduction band position of amorphous In-Ga-O and Ga-Zn-Sn-O.[14] Efficient water oxidation catalysts have nominally amorphous mixed-metal-oxide phases on the surface that are responsible for the catalytic activity.[8,15]

Designing mixed-metal oxides for these, and other, applications requires the ability to systematically vary structural and electronic properties. The fundamental understanding of correlations between composition, local atomic bonding, and electronic structure essential for this goal, however, is lacking – particularly for amorphous and mixed-amorphous-polycrystalline thin films. Much of this knowledge gap is due to the lack of long range order in these systems, which makes typical structural probes (e.g. X-

ray diffraction, XRD) inadequate, necessitating the use of synchrotron techniques (e.g. X-ray absorption spectroscopy, XAS).[16] The electronic structure is also complex for amorphous and multicomponent systems.[17,18] Electron correlation in transition metal oxides can make computation of electronic structure difficult[19] for amorphous materials where large structure units are required for calculations.[20] For such amorphous oxides, the electronic structure might be predicted based on the experimental atomic and electronic structures of the parent crystalline binary oxides. However, the coordination environment in amorphous films can differ substantially from purely crystalline oxides[21–24] and the electronic structure is dependent on the metal cation coordination.[25,26]

Here we aim to understand how the electronic structure of mixed-metal-oxide thin films can be controlled to design new materials. We systematically compare the electronic and local atomic structure of $M_yAl_{1-y}O_x$ thin films, where M = V, Cr, Mn, Fe, Co, Ni, Cu, Zn, or Ga and y varies from 0.1 to 0.7. The materials can be considered mixtures of a wide-band-gap insulating oxide, e.g. amorphous Al_2O_3 (alumina), and metal cations that have varying number of 3d electrons. Alumina is chosen as the host material because it can readily incorporate many different cations as an amorphous film[27] and has a wide band-gap[26] that allows for directly measuring the energetics of the electronic states added into the band gap. Additionally, transition-metal-incorporated alumina is of interest for many applications, e.g. catalysis[12,28–32] and photovoltaics,[33] where the electronic structure determines its utility. We previously showed such multicomponent $M_yAl_{1-y}O_x$ thin films are easily synthesized from solution precursors and are ultra-smooth over a wide composition range.[27] Here we focus on understanding the local atomic and electronic structure of the films, and how they depend on composition. Except for Co, Ni, and Cu at $y \geq 0.2$, the $M_yAl_{1-y}O_x$ films remain amorphous up to $y = 0.4$ or higher. This composition space allows for an assessment of periodic trends based on number of d-electrons and the metal cation oxidation state. The transition metal concentration range also allows for the study of both amorphous alloy and mixed-amorphous-polycrystalline compositions, giving access to multiple coordination environments for most of the transition metals.

We use X-ray absorption spectroscopy to determine the coordination around the transition metal, the metal-oxygen bond length, and the transition metal oxidation state. UV-vis absorption spectroscopy is used to determine the optical charge-transfer band gap and further confirm coordination environment around the transition metals. The electronic structure in the valence band is determined using X-ray photoelectron spectroscopy (XPS). By empirically probing the electronic and local atomic structure, we determine that the d-electron count of the transition metal cation, which is linked with the choice of transition metal, oxidation state, and concentration, influences the final electronic structure and optical properties of the film.

Experimental

Film Deposition. Aqueous precursor solutions were prepared from transition-metal nitrate (or chloride in the case of V) salts and aq. $Al(NO_3)_x(OH)_{3-x}$ solutions, as described previously.[27] The aq. $Al(NO_3)_x(OH)_{3-x}$ solution was prepared via the process described by Wang et al.[34] Briefly, approximately 40 mL aliquots of 1 M aq. $Al(NO_3)_3$ were subject to 1.8 kC of reductive charge (-100 mA for 5 h) while stirring in a glass container using an 80 cm^2 Pt-mesh working electrode, a Pt-coil counter electrode (separated by a glass frit), and a DC power supply. This results in an increase of the pH of the solution, causing oligomerization and formation of soluble "flat" $[Al_{13}(\mu_3\text{-}OH)_6(\mu\text{-}OH)_{18}(H_2O)_{24}](NO_3)_{15}$ clusters, which we will refer to as the f-Al_{13} precursor solution. To account for any evaporation, the f-Al_{13} solution was then standardized to a 1 M [Al] via gravimetric analysis. The f-Al_{13} precursor was then mixed with the 1 M aq. transition-metal nitrate solutions in appropriate ratios to achieve the desired film compositions (the solution metal ratios are maintained in the film, as shown previously).[27]

Substrates for film deposition varied by experiment. 500-µm-thick (100) Si was used for XAS and ellipsometry. For XPS measurements, 500 µm-thick (100) Si substrates were coated with 25 nm of Ti (adhesion layer) followed by 50 nm of Ir via electron beam evaporation prior to film deposition (to minimize charging phenomena). Fused-quartz substrates were used for UV-vis and X-ray reflectivity (XRR) measurements. All substrates were cut into 2×2 cm squares and cleaned via sonication

in aq. detergent solution (Contrad 70, 6.25%) for 10 min. Substrates were then rinsed with 18.2 MΩ·cm water for 30 s and dried for 30 s on a spin coater at 3000 rpm.   To render them hydrophilic, the substrates were treated with O_2/N_2 plasma for 10 min, and finally water-rinsed for 10 s and spin-dried for 20 s at 3000 rpm before deposition. Approximately 250 µL of precursor solution (enough to cover the substrate) was dropped from a plastic syringe through a 0.2 µm filter onto the substrate, which was then spun at 3000 rpm for 30 s. The spun film was immediately placed on an Al block on a hot plate at 150 °C for 5 min to set the film and then moved onto an Al block at 450 °C to anneal for 10 min for multi-layer films or 30 min for single-layer films. To fabricate multi-layer films the substrates were subject to successive water rinses, solution depositions and 150 °C/450 °C annealing steps until the desired number of layers was reached, at which point the film was annealed at 450 °C for 30 min.

X-ray Absorption Spectroscopy. XAS measurements were performed on Beamline 12-BM,B (bending magnet) of the Advanced Photon Source at Argonne National Lab. Data were collected at V, Cr, Mn, Fe, Co, Ni, Cu, Zn, and Ga K-edges. Si(111) was used as a monochromator and the incoming beam was detuned 60-80% for harmonic rejection with a 1.5 mm × 0.5 mm spot size. Samples were approximately 300-nm-thick films deposited on Si(100) substrates and were measured in air at room temperature in total fluorescence mode using a 13-element Ge detector (Canberra). The energy was calibrated by measuring the absorption at the K-edge of metallic foils of the same element (except for the L-edge of Ta used for Ga calibration) in transmission mode directly before and after each set of samples (2-5 samples) to verify there was no shift in the energy axis. The edge energy was selected as the highest point in the first derivative of $\mu(E)$ and shifted to the metal foil value as listed in the Hephaestus software.[35] All sample spectra for a given metal edge were shifted by this same amount before determining E_0 for the sample. The energy of the first peak in the first derivative of $\mu(E)$ (after the pre-edge feature) was taken as E_0 for each sample (Table A.1).

All XAS data was analyzed using the Athena/Artemis software package.[35] Absorption spectra were merged (between two and six scans) and normalized to an edge step of 1.0 using the Athena software. FT-EXAFS spectra were fit using Artemis

software, in which theoretical scattering paths of crystalline oxides (Shcherbinaite-V_2O_5,[36] α-Cr_2O_3,[37] CrO_3,[38] α-Mn_2O_3,[39] α-Fe_2O_3,[40] Co_3O_4,[41] NiO,[42] CuO,[43] hexagonal ZnO,[44] and β-Ga_2O_3[45]) were computed using FEFF6[46,47] with crystal structures obtained from the Inorganic Crystal Structure Database (ICSD). Fits were performed over an R-space of 0.9 – 2 Å in the Fourier transform using k-ranges of 2.5 to 11 Å^{-1} (V, Fe, Co, Ni, Cu, Zn) or 2.5 to 12 Å^{-1} (Cr, Mn, Ga) with a Hanning window and k^2-weighting. EXAFS spectra plotted in k-space can be found in Figure A.14. The amplitude reduction factor, S_0^2, values for each metal edge were calculated from fits to spectra of polycrystalline films (Shcherbinaite-V_2O_5, α-Cr_2O_3, α-Mn_2O_3, α-Fe_2O_3, Co_3O_4, NiO, CuO, hexagonal-ZnO, and β-Ga_2O_3) and were constrained between 0.7 and 1.0. The obtained S_0^2 value was then used in the fits to sample spectra in order to calculate oxygen coordination around each transition metal. The values of the difference in energy alignment between sample and standard, E_0, the difference in path length between sample and standard, ΔR, and the mean square disorder parameter, σ^2, were also allowed to vary in the fits (see Eq. A.1).[35] The number of independent points ranged from 5.3 to 6, determined by the Nyquist criterion.

X-ray Photoelectron Spectroscopy. Valence band XP spectra were collected on a ThermoScientific EscaLab 250 with a monochromatic Al Kα (1486 eV) X-ray source using a 500 μm spot size, 40 eV pass energy and 0.2 eV step size. Core-level spectra (Figures A.3 – A.12) were collected with a pass energy of 20 eV and step size of 0.1 eV. An in-lens electron flood gun was used for charge neutralization. All spectra were shifted so that the adventitious C-H peak was centered at 248.8 eV binding energy.

X-ray Diffraction. XRD patterns (shown in Figures A.1 and A.2) were collected on the same samples used for XAS measurements. Data were collected in a grazing-incidence (GIXRD) geometry on a Rigaku SmartLab with a Cu Kα source. The incident beam angle was 0.5° (relative to sample) and reflected signal was collected with a scintillation point detector over a range of 10 – 70° 2θ in step sizes of 0.1° with a 30 s integration time. Ni foil was used to filter out Cu Kβ radiation.

Thickness Characterization. The thickness of films on fused-quartz substrates used for optical measurements was measured directly using XRR except for films that were too

rough (frequently found for compositions know to phase segregate) to yield Kiessig fringes that could be fit. For these compositions, an identical film was deposited onto a (100) Si substrate and the thickness measured with ellipsometry. XRR was carried out on a Bruker D8-Discover with a Cu Kα source. Spectra were collected from $0 - 6°$ 2θ after sample alignment. The thickness of each sample was determined with Fourier transform fits using GlobalFit software (Rigaku). Ellipsometry measurements were carried out on a Woollam M44 Spectroscopic Ellipsometer. Data were fit with a single Cauchy-model layer to determine the thickness.

Optical Absorption Characterization. Transmittance and reflectance measurements were collected on a Perkin Elmer Lambda-1050 UV/Vis/NIR spectrophotometer utilizing a 150 mm integrating sphere. Deuterium and tungsten halogen light sources were used with a Si photomultiplier tube. The transmittance and reflectance measurements were taken at the transmittance and reflectance ports on the integrating sphere, respectively. This allowed for collection of all transmitted (or reflected) light, including both specular and diffuse components. A Speclatron® reflectance standard was used. The optical absorption coefficient was calculated using

$$\alpha = -\frac{1}{l}\left(\ln\left(\frac{T_s}{1-R_s \cdot C_r}\right) - \ln\left(\frac{T_q}{1-R_q \cdot C_r}\right)\right), \quad\quad\quad \text{(Eq. 2.1.)}$$

where α (cm^{-1}) is the absorption coefficient, l is the film thickness (cm), T_s is the transmittance of a sample, R_s is the reflectance of a sample, C_r is the reflectance correction factor, T_q is the transmittance and R_q is the reflectance of the fused-quartz substrate, respectively.[48]

The C_r parameter accounts for the difference in the collection efficiency of the integrating sphere as a function of the amount of specular and diffuse reflected light. As reported previously a C_r of 0.8 is needed when a Speclatron® reflectance standard is used with samples that are very smooth and whose reflectance is mostly specular.[48] We verified this as a reasonable factor by calculating the absorbance of our fused-quartz substrate with and without using the correction factor. If the correction factor is not used negative non-physical absorbance values are found. This is due to the higher collection

efficiency of an integrating sphere with regards to specular reflected light over diffusely reflected light. Thus the "1-R" term is too small resulting in absorbance that is too low (negative if in a region of the spectrum where no absorption is observed). With the correction factor applied no non-physical negative absorbance is observed. Effective optical band gaps were determined by the energy where the absorption coefficient α was $\geq 10^{-5}$ cm^{-1} to avoid tail state transitions that typically occur below this value.[49]

Results and Discussion

As discussed in the following sections, we find that the transition-metal d-electron count, which dictates the crystal-field stabilization energy (CFSE) and therefore preference for octahedral (O_h) or tetrahedral (T_d) coordination (based on the octahedral site preference energy, OSPE),[50] is the best predictor of the resulting film's structural and electronic properties. The electronic structure of the different transition-metal-incorporated amorphous aluminum oxide (a-Al$_2$O$_3$) thin films can be generalized into four different groups: metal cations with no d-electrons (d^0), those with exactly five d-electrons (d^5, high spin), those with partially filled orbitals (d^n, but not d^5) and cations with completely filled d-orbitals (d^{10}).

From our previous work,[51] the local structure of a-Al$_2$O$_3$ deposited via spin-casting from aqueous f-Al$_{13}$ solutions was shown by ^{27}Al solid-state nuclear magnetic resonance spectroscopy to consist of a mixture of 4-, 5-, and 6-coordinate Al species. The average Al coordination number is about 4.6 over a wide annealing temperature range (400 – 800 °C). Only about 10% of the Al in these films exists as 6-coordinate species. This average coordination gives a low oxygen coordination number, (C_O), consistent with an open amorphous network. C_O is dependent on the metal coordination, C_M, and oxidation state, Q_M, by

$$C_O = \frac{C_M |Q_O|}{|Q_M|},$$ (Eq. 2.2)

where Q_O is the charge on the oxygen anions.[52] Previously we showed that d^n (where n $\neq$ 0, 5, or 10) cations phase segregate from a-Al$_2$O$_3$ into transition metal oxide particles at relatively low concentration (>10% total metal).[27] Here we show that when

12

incorporated into the a-Al_2O_3 matrix at lower concentrations, these d^n cations may adopt a different local coordination or oxidation state from their parent transition metal oxide (i.e. that prepared in this work under the same conditions from the pure transition metal salt, $y = 1$). This effect is presumably driven by the amorphous network in which a low oxygen coordination (C_O) is more energetically favorable for an open network and an amorphous structure.[52,53] This phenomenon makes predictions of the electronic structure for mixed-oxide amorphous films difficult, as most non-computational predictions are based on the assumption that bonding motifs are similar between the parent and the mixed-metal oxides.[54] Transition-metal cations that are d^0, d^5 high-spin, or d^{10} incorporate into a-Al_2O_3 up to much higher concentrations, likely due to their isotropic d-electron configurations (i.e. no CSFE) allowing them to maintain a low coordination number.[27] The average coordination numbers of the transition metal in amorphous films in this work are similar to that of a-Al_2O_3, ~4.5, suggesting that the transition metals are replacing Al atoms in the amorphous structure. Additionally, there is no diffraction from crystalline Al_2O_3 or MAl_2O_4 phases, indicating the films are amorphous alloys. In the next sections we discuss the electronic structure, local atomic structure, and optical properties of each class of metal cations in more detail.

d^0 Transition-Metal Cations. Both $V_yAl_{1-y}O_x$ and $Cr_yAl_{1-y}O_x$ films contain d^0 cations, V^{5+} and Cr^{6+}, respectively, as determined by the position of the metal K-edge as well as V and Cr 2p XPS (Figures A.4 and A.5). The lack of d-electrons on these cations results in a zero crystal field stabilization energy (CFSE) and therefore no preference for T_d or O_h coordination.[55] The V^{5+} and Cr^{6+} cations readily adopt the lower cation coordination of the a-Al_2O_3 matrix (~4.5), allowing the mixed films to remain amorphous up to high concentrations ($y = 0.5$). Fits to the FT-EXAFS data in Figure 2.1b indicate that V^{5+} cations have an average coordination of 4.5 (Figure 2.1c) in $V_yAl_{1-y}O_x$ films, presumably a mix of 4- and 5-coordinate V^{5+}. The presence of 4- and 5-coordinate V is further supported by the XANES data in Figure 2.1a, where the intensity of the pre-edge feature (Figure 2.1a inset) is high for $V_yAl_{1-y}O_x$ films, indicative of a non-centrosymmetric environment. The narrower distribution of V – O bond lengths in $V_yAl_{1-y}O_x$ films (< 0.2 Å), determined from fits to the FT-EXAFS shown in Figure 2.1c, suggests the V

13

geometry is different than in V_2O_5 films, despite the similar coordination number. The ability of V^{5+} cations to incorporate into the a-Al_2O_3 film is maintained up to high concentration, $y = 0.5$, as shown previously.[27] At $y = 0.7$ a crystalline VO_x phase different from V_2O_5 is present[27] (Figure A.2) however, by XAS the film still appears very disordered; the XANES region (Figure 2.1a) of $V_{0.7}Al_{0.3}O_x$ is more similar to amorphous $V_yAl_{1-y}O_x$ films than the crystalline V_2O_5, with no sharp features past the absorption edge.

The unique coordination of V^{5+} cations in $V_yAl_{1-y}O_x$ films compared to V_2O_5 is also apparent from their UV-vis absorption spectra in Figure 2.1e. The UV-vis spectrum of V_2O_5 shows absorption bands centered around 480, 420, 375, and 260 nm, representing transitions from occupied O 2p into empty V 3d orbitals. These appear to correspond to the four d-orbital energy levels created by the crystal field of the square pyramidal geometry of the V^{5+} cation in the Shcherbinaite-V_2O_5 phase.[56] Additionally, the band gap of the V_2O_5 film found here (~ 2.1 eV) agrees well with previous reports.[56,57]

The spectra for $V_yAl_{1-y}O_x$ films, where $y \leq 0.5$, appear to have only two distinct absorption bands, 280 and 225 nm. These likely correspond to O 2p – V 3d transitions into the empty t_2 and e orbitals, respectively, of a tetrahedral V^{5+} cation. The contraction of the d-splitting (as expected in going from square pyramidal to tetrahedral geometry) results in a greater energy difference between the O 2p orbitals and the lowest V 3d orbitals (t_2 in distorted-octahedra and e in tetrahedra). This pair of strong absorption peaks has been seen for tetrahedral V^{5+} in other systems, notably on Al_2O_3/Al(OH)$_3$ surfaces.[58] The broadness of the absorption peaks is likely reflective of the broad range of d-band energy levels due to variation in V-O bond distances and O-V-O bond angles in the disordered amorphous film. It is also notable that the spectrum for $V_{0.7}Al_{0.3}O_x$ more closely resembles those of amorphous $V_yAl_{1-y}O_x$ compositions, again indicating the similar V – O local coordination that is different from that in V_2O_5.

Due to the lack of d-electrons, the valence band position of the $V_yAl_{1-y}O_x$ films remains relatively constant with increasing V content, as shown in Figure 2.1d. The optical band gap (Figure 2.1e), however, decreases substantially upon addition of V at $y =$

14

0.1 to a-Al_2O_3, suggesting modification of the conduction band. This decrease in effective band gap is thus the result of insertion of V 3d orbitals above the O 2p valence band, but below the Al 3s conduction band of a-Al_2O_3. The $V_{0.5}Al_{0.5}O_x$ and $V_{0.7}Al_{0.3}O_x$ films have the same effective band gap which is smaller than that of the amorphous $V_yAl_{1-y}O_x$ films, despite the similar local V coordination, likely due to full delocalization of the V 3d orbitals.

In whole, the data thus show it is possible to systematically tune the conduction band edge position of $V_yAl_{1-y}O_x$ via the concentration of V cations while maintaining an essentially constant valence band position. The conduction band edge position, dictated by the energy of the unfilled 3d orbitals of V, is modulated by the change in orbital overlap of the V^{5+} 3d orbitals with V^{5+} concentration.
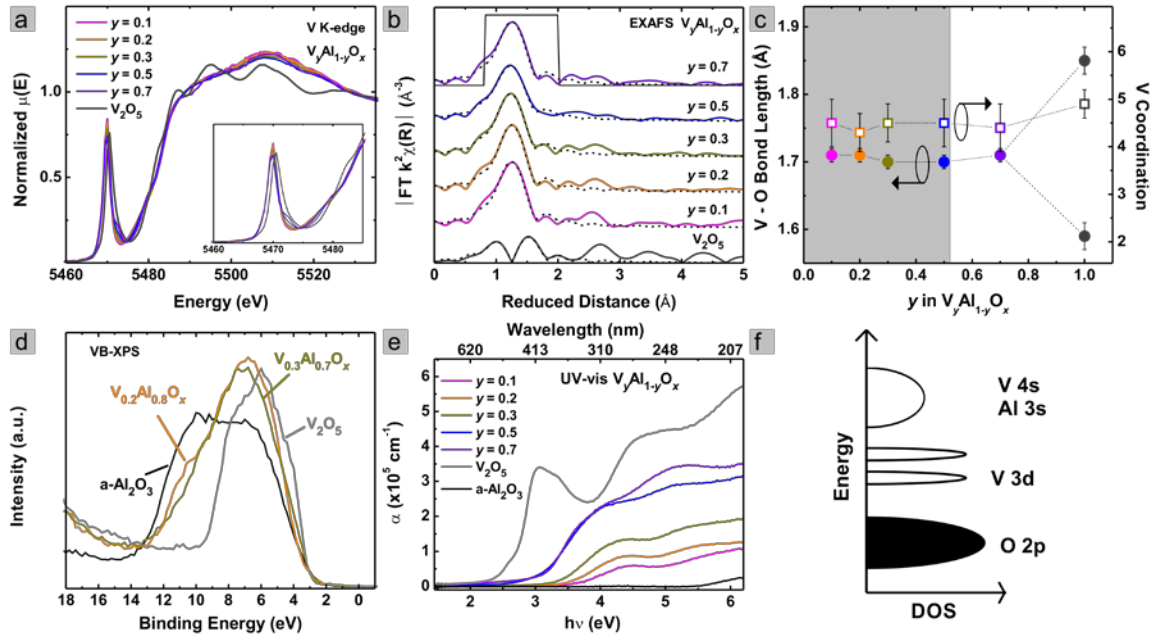
Figure 2.1. Analysis of $V_yAl_{1-y}O_x$ thin films. a) V K-edge XANES, b) FT-EXAFS with fits (dashed lines) to the first coordination sphere (solid black line), c) V-O bond lengths (closed circles) and coordination numbers (open squares) from fits to the FT-EXAFS, d) valence band XP spectra, e) thin film UV-vis spectra, and f) schematic density of states (DOS) diagram of amorphous $V_yAl_{1-y}O_x$ films. The grey shaded region in (d) indicates the amorphous composition range and lines between points are meant to guide the eye. The data show that the conduction band edge – and hence optical band gap – can be tuned by V concentration while the position of the valence band edge is kept constant.

15

In our analysis, we find that $Cr_yAl_{1-y}O_x$ films contain d^0 Cr^{6+} cations as well as d^3 Cr^{3+} cations. The ratio of Cr^{6+} to Cr^{3+} decreases with increasing Cr concentration. The presence of Cr^{6+} despite starting with a Cr^{3+} precursor is likely due to oxidation of Cr^{3+} to $HCrO_4^-$ by molecular oxidation during spin-casting/annealing. The $Cr^{3+}/HCrO_4^-$ reduction potential becomes more negative with increasing pH and decreasing concentration.[59] We find higher concentrations of Cr^{6+} in films that have lower total Cr concentration and a higher precursor solution pH (f-Al_{13} precursor has a higher pH than aq. 1 M $Cr(NO_3)_3$).

The presence of both Cr^{6+} and Cr^{3+} was confirmed by multiple techniques, shown in Figure 2.2. The Cr K-edge in Figure 2.2a gradually shifts to lower energy as y goes from 0.1 to 0.5, indicating a decrease in the average oxidation state of Cr in the films. Additionally, the intensity of the pre-edge feature in the XANES region (Figure 2.2a inset) of $Cr_yAl_{1-y}O_x$ films continually decreases with increasing Cr, indicating a decrease in tetrahedral Cr^{6+} and an increase in octahedral Cr^{3+}.[60] The oxidation states of Cr are further confirmed by Cr 2p XPS (Figure A.5). The FT-EXAFS in Figure 2.2b has two distinct first shell peaks for $y = 0.2 - 0.5$, suggesting there are two different M – O bond lengths; Cr^{6+} has tetrahedral coordination with a short bond length around 1.6 Å, while Cr^{3+} is octahedral with a bond length of about 1.9 Å.[37,38] Absorption bands from both Cr species can also be seen in the UV-vis spectra in Figure 2.2e for films with y ≥ 0.5 (the symmetry-forbidden Cr^{3+} d-d transitions in films with lower Cr concentration are too weak to be observed).[61] The O 2p – Cr 3d transitions of Cr^{6+} are centered around 3.4 and 4.5 eV, while the d – d transitions of Cr^{3+} are centered at 2.0 and 2.6 eV.[62] The energy of Cr^{3+} d-d transitions in $Cr_yAl_{1-y}O_x$ films is similar to crystalline $α-Al_{1-x}Cr_xO_3$.[63,64] As the amount of Cr increases, so does the ratio of Cr^{3+} to Cr^{6+} resulting in overlapping O 2p – Cr 3d transitions. The presence of Cr^{3+} also results in a shift of the valence band maximum to higher energies due to the occupied Cr 3d states as shown in the valence band XP spectra in Figure 2.2d.

Overall, the data on $Cr_yAl_{1-y}O_x$ films show that the electronic structure can be systematically tuned by modulating the valence band edge position through the Cr^{3+}/Cr^{6+}

ratio and the related local coordination geometry. Synthetically, the Cr^{3+}/Cr^{6+} ratio can likely be modified via the precursor transition metal concentration and solution pH.

Figure 2.2. Analysis of $Cr_yAl_{1-y}O_x$ thin films. a) Cr K-edge XANES, b) FT-EXAFS with fits (dashed lines) to the first coordination sphere (solid black line), c) Cr-O bond lengths (closed circles) and coordination numbers (open squares) from FT-EXAFS fits, d) valence band XP spectra, e) UV-vis spectra, and f) schematic DOS diagram of amorphous $Cr_yAl_{1-y}O_x$ thin films showing both Cr^{6+} (T_d) and Cr^{3+} (O_h) coordination. The grey shaded region in (d) indicates the amorphous composition range and lines are meant to guide the eye. The data show how the valence band edge can be tuned to higher energy as the octahedral Cr^{3+} concentration is increased.

d^5 Transition-Metal Cations. The $Fe_yAl_{1-y}O_x$ films contain d^5 Fe^{3+} ions, determined from the energy of the main edge on the Fe K-edge absorption spectra in Figure 2.3a and further confirmed by XPS (Figure A.7). The d^5 electron count and the weak field of the oxygen ligands leads to isotropy in the crystal field, resulting in no difference in CFSE for T_d or O_h coordination. Fitting of the FT-EXAFS of the $Fe_yAl_{1-y}O_x$ films (Figure 2.3b and 3c) indicates that the average oxygen coordination around Fe atoms is ~ 4.5, suggesting more tetrahedral as opposed to octahedral Fe^{3+} ions. T_d coordination is also consistent with the increased intensity of the pre-edge XANES feature (Figure 2.3a inset) compared to α-Fe_2O_3, in which Fe^{3+} has O_h coordination. It is likely that the ability of

17

the Fe^{3+} ion to readily adopt a lower coordination, e.g. T_d, allows the $Fe_yAl_{1-y}O_x$ films to remain amorphous up to high amounts of Fe.[27]

The presence of Fe in $Fe_yAl_{1-y}O_x$ films shifts the UV-vis absorption onset to lower energies compared to a-Al_2O_3, as seen in Figure 2.3e. This decrease in effective band gap is the result of a change in the charge transfer gap from an O 2p – Al 3s transition in a-Al_2O_3 to O 2p – Fe 3d in $Fe_yAl_{1-y}O_x$ films, as the effective band gap estimated from the UV-vis data, 3.0 eV (Figure 2.3e), agrees well with the charge transfer gap reported for α-Fe_2O_3.[65,66] The forbidden Fe^{3+} d – d transitions are likely too weak to be observed in the optical absorption spectra for films with low Fe content,[61] but are visible in $Fe_{0.7}Al_{0.3}O_x$ and α-Fe_2O_3 (although the amorphous nature of the former causes significant broadening of the features). Although d-d transitions are not observed in the optical spectra of $Fe_yAl_{1-y}O_x$ films with low Fe content, VB-XPS in Figure 2.3d shows (via the shift in the valence band edge) that there are filled Fe 3d states at the top of the valence band, above the O 2p states. The addition of filled 3d states above the valence band of a-Al_2O_3 is expected from the five additional valence electrons of Fe^{3+} compared to Al^{3+}.
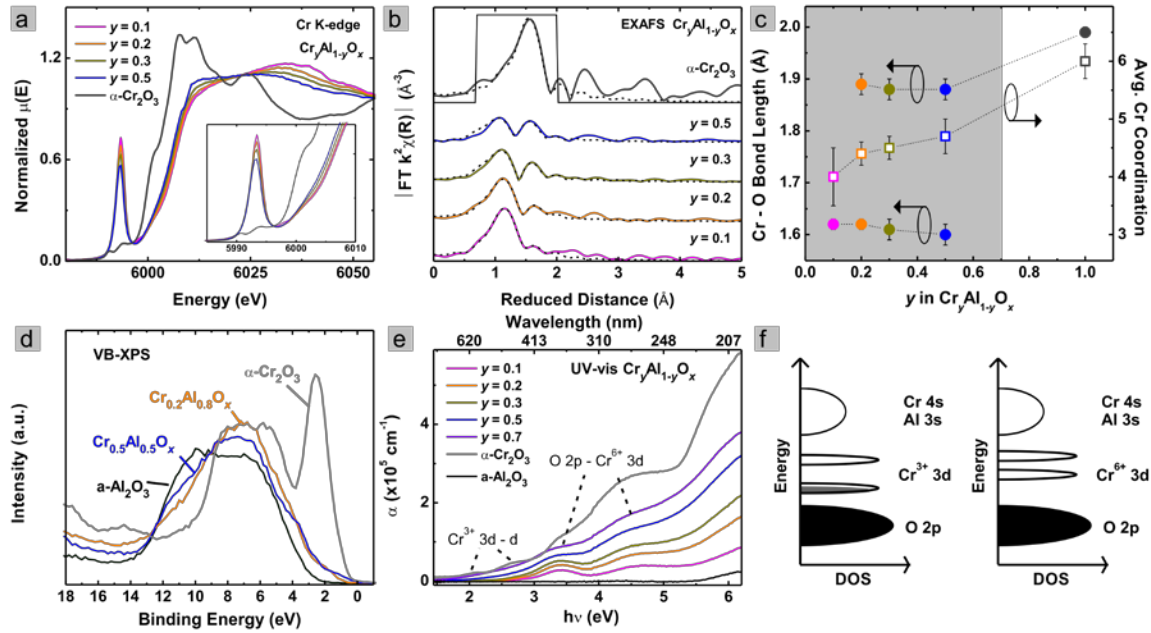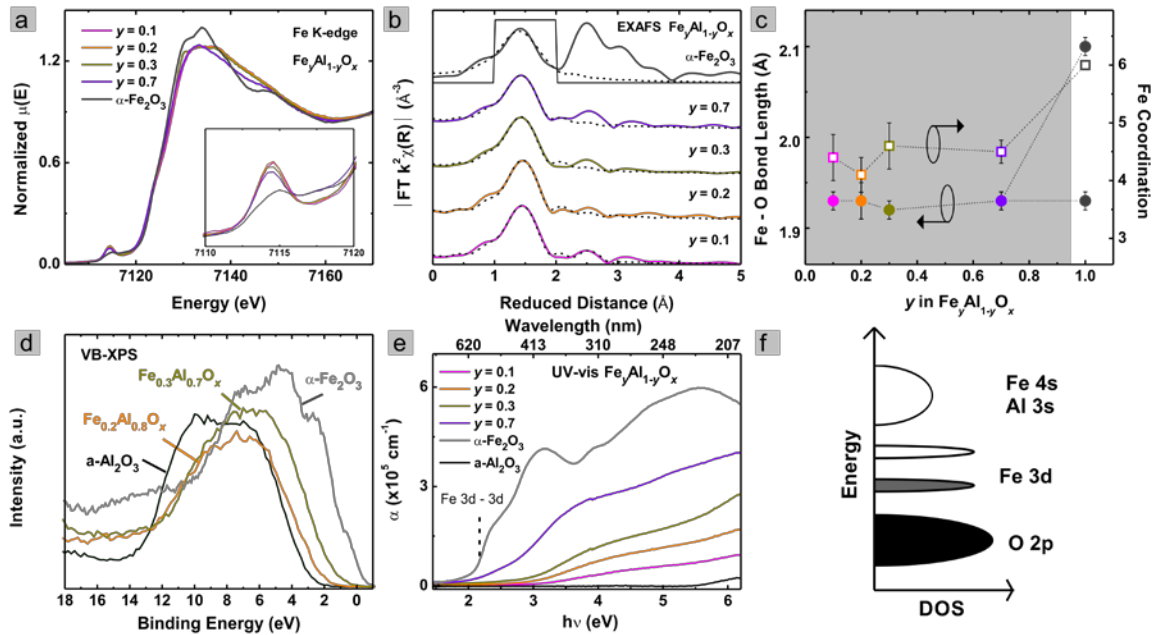

Figure 2.3. Analysis of $Fe_yAl_{1-y}O_x$ thin films. a) Fe K-edge XANES, b) FT-EXAFS with fits (dashed lines) to the first coordination sphere (solid black line), c) Fe-O bond lengths

18

(closed circles) and coordination numbers (open squares) from fits to FT-EXAFS, d) valence band XP spectra, e) UV-vis spectra, and f) schematic DOS diagram of $Fe_yAl_{1-y}O_x$ films. The grey shaded region in (d) indicates the amorphous composition range and lines between points are meant to guide the eye. The data show how Fe is largely tetrahedral in coordination and introduces occupied states at the top of the valence band that tune the VB edge energy along with unfilled states that give rise to visible optical transitions.

$Mn_yAl_{1-y}O_x$ films also contain some cations with a d^5 electron configuration, Mn^{2+}, as determined by the slightly lower energy of the Mn K-edge in Figure 2.4a compared to that of the α-Mn_2O_3 standard. However, a large percentage of Mn in the film exists in the d^4 Mn^{3+} configuration, based on the similarity of the XANES region to the α-Mn_2O_3 spectrum and the shake-up features of the Mn 2p peaks in the XP spectra (Figure A.6).[67] The single peak in the pre-edge, Figure 2.4a inset, for $Mn_yAl_{1-y}O_x$ films where $y \leq 0.4$ suggests that Mn is not present in a centro-symmetric O_h geometry, but is more disordered.[68] This distortion is possibly due to the presence of multiple oxidation states and the amorphous a-Al_2O_3 network lowering the coordination number for Mn. Fits to the FT-EXAFS, shown in Figures 2.4b and 2.4c, indicate a low coordination around Mn atoms, ~ 4.0, however the extracted values may be artificially low due to the high amount of disorder in the local geometry (i.e. bond lengths and coordination number) of Mn atoms.[69,70]

The disorder of the Mn local geometry is also apparent from the UV-vis spectra in Figure 2.4e, where the absorption edge of each spectrum is difficult to determine due to significant tailing. The onset of absorption is at a similar energy (~ 2 eV) to that of $MnAl_2O_4$,[71] however the spectral features in amorphous $Mn_yAl_{1-y}O_x$ films are significantly broader due to multiple Mn and Al geometries and the overall amorphous structure. Crystalline Mn_2O_3 is present for films where $y > 0.4$, but the absorption spectra of these films more closely resemble those of the amorphous $Mn_yAl_{1-y}O_x$ films, indicating much of the Mn is still present in the a-Al_2O_3 phase. The VB-XPS data in Figure 2.4d show an increase in the valence band edge to higher energy, likely due to the addition of filled 3d states from $Mn^{2+/3+}$. Given the d-electron counts of Mn^{2+} and Mn^{3+}, unfilled 3d Mn states are presumably added as well, giving rise to overlapping Mn 3d –

3d and O 2p – Mn 3d transitions that account for the tailing absorption in $Mn_yAl_{1-y}O_x$ films.

This data shows that, like adding Fe^{3+}, the addition of $Mn^{2+/3+}$ adds new filled electronic states at the valence band edge and unfilled states in the band gap of $a\text{-}Al_2O_3$. The data also indicate that precise tuning of the electronic structure of $Mn_yAl_{1-y}O_x$ films is difficult due to the multiple oxidation states and local geometries of Mn cations resulting in many overlapping electronic states.

Figure 2.4. Analysis of $Mn_yAl_{1-y}O_x$ thin films. a) Mn K-edge XANES, b) FT-EXAFS with fits (dashed lines) to the first coordination sphere (solid black line), c) Mn-O bond lengths (closed circles) and coordination numbers (open squares) from FT-EXAFS fits, d) valence band XP spectra, (e) UV-vis spectra, and f) schematic DOS diagram of $Mn_yAl_{1-y}O_x$ films. The grey shaded region in (d) indicates the amorphous composition range and lines between points are meant to guide the eye. The data show that the addition of Mn cations in $Mn_yAl_{1-y}O_x$ adds both occupied and unoccupied states of Mn^{2+} and Mn^{3+} giving rise to broad optical absorption features.

$d^{6,7,8,9}$ *Transition-Metal Cations.* Transition-metal cations that are not d^0, d^5 high spin, or d^{10} contain partially filled degenerate d-orbitals which leads to a greater crystal-field stabilization energy and a strong preference for octahedral vs. tetrahedral coordination. As we have shown previously, these cations tend to readily phase separate to form the binary transition metal oxides rather than an amorphous alloy with $a\text{-}Al_2O_3$.[27]

In the XANES edge analysis of $Co_yAl_{1-y}O_x$ films here, we find Co in both the 2+ and 3+ oxidation states, with increased 2+ content at lower Co concentrations. These oxidation states are also confirmed by Co 2p XPS (Figure A.8). In the binary oxide, Co_3O_4, Co^{3+} ions have a d^6 electron count and an O_h coordination while Co^{2+} ions have a d^7 electron count in a T_d geometry. $Co_yAl_{1-y}O_x$ films with y = 0.1, which are X-ray amorphous (Figure A.1), have Co in a lower average coordination with longer Co – O bond lengths than in Co_3O_4 (shown in Figure 2.5c) consistent with more Co^{2+} in a T_d geometry.[41,72] The higher Co^{2+} content in $Co_{0.1}Al_{0.9}O_x$ films is also evident from the lower energy of the main edge in the XANES region of Figure 2.5a. With higher Co content, Co_3O_4 nanoparticles readily phase segregate from the amorphous alumina network,[27] confirmed by XRD (Figure A.1) and the appearance of the second coordination sphere in the FT-EXAFS in Figure 2.5b.

The optical spectra of $Co_yAl_{1-y}O_x$ films in Figure 2.5e are consistent with the atomic structure of the films. In the $Co_{0.1}Al_{0.9}O_x$ film, the optical absorption onset is shifted to lower energies. The shift is likely due to either O 2p – Co 3d or Co 3d – Al 3s transitions; VB-XPS in Figure 2.5d shows the presence occupied of 3d states above those of O 2p in the $Co_{0.1}Al_{0.9}O_x$ film. The thinness and low Co content of this film prevent the observation of Co^{2+} d – d transitions that are seen in $CoAl_2O_4$.[73] $Co_yAl_{1-y}O_x$ films with higher Co content have an absorption onset at 1.5 eV due to Co^{3+} 3d – Co^{2+} 3d transition while the feature at 2.0 eV is from O 2p – Co 3d transitions.[74] Each film with Co content at y > 0.1 has an absorption spectrum that closely resembles that of the binary oxide, Co_3O_4, indicating that phase-segregated Co_3O_4 nanoparticles dominate the optical response.[74,75]

Figure 2.5. Analysis of $Co_yAl_{1-y}O_x$ thin films. a) Co K-edge XANES, b) FT-EXAFS with fits (dashed lines) to the first coordination sphere (solid black line), c) Co-O bond lengths (c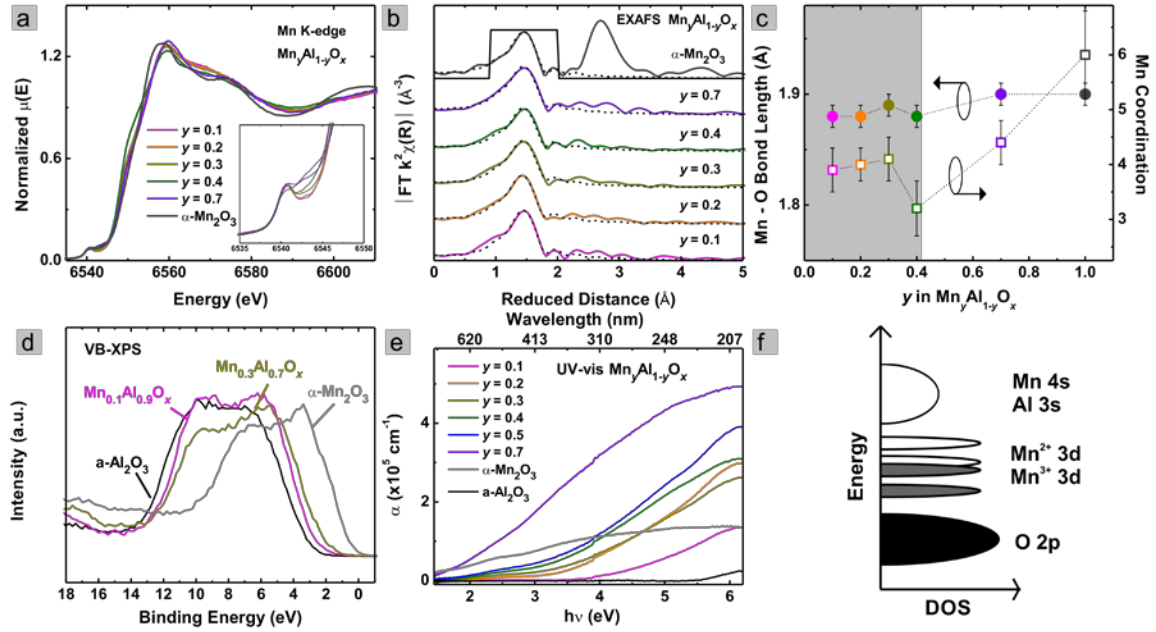losed circles) and coordination numbers (open squares) from EXAFS fits, d) valence band XPS spectra, e) UV-vis spectra, and f) schematic DOS diagram of amorphous $Co_yAl_{1-y}O_x$ films. The grey shaded region in (d) indicates the amorphous composition range. Lines between points are meant to guide the eye. The data show that at $y \leq 0.1$ filled and unfilled 3d states of Co^{2+} are added to the band gap of a-Al_2O_3. At higher concentrations Co_3O_4 particles phases separate and dominate the optical response.

Based on the energy of the Ni K-edge XANES spectra in Figure 2.6a, Ni cations in $Ni_yAl_{1-y}O_x$ films are present in the 2+ oxidation state. The Ni oxidation state is further confirmed by Ni 2p XPS (Figure A.9). At low Ni content, $y \leq 0.1$, the d^8 Ni cations adopt a T_d coordination (i.e. instead of the O_h coordination that would be predicted based solely on the CFSE), apparent from the fits to the FT-EXAFS (Figures 2.6b and 2.6c) and the increased intensity of the pre-edge feature in the XANES region, Figure 2.6a inset. This unique Ni geometry is likely due to the low concentration and the influence of the low coordination of the surrounding a-Al_2O_3 network. Additionally, the Ni – O bond length in the $Ni_{0.1}Al_{0.9}O_x$ film is 2.05 Å, about 0.1 Å shorter than in NiO, consistent with a similar oxidation state, but a lower coordination number. These Ni – O bond lengths are still longer than those of T_d Ni^{2+} in crystalline $NiAl_2O_4$, likely due to the amorphous structure of the films. At this low Ni content, the films are also known to be

amorphous,[27] confirmed by XRD (Figure A.1) and the lack of the second coordination sphere in the FT-EXAFS shown in Figure 2.6b.

At higher Ni content ($y > 0.1$), NiO phase separates from the a-Al_2O_3 (Figure A.1). The phase separation of NiO is also seen in the FT-EXAFS in Figure 2.6b, where the second coordination sphere intensity becomes apparent above 2 Å. Evidence of NiO in the films with Ni content at $y > 0.1$ is also clear from the UV-vis spectra in Figure 2.6e, where the absorption edge shifts to ~3.5 eV, representing O 2p – Ni 3d transitions.[76,77] VB-XPS data in Figure 2.6d show that there are occupied Ni 3d states above the O 2p states for all $Ni_yAl_{1-y}O_x$ films. There are no clear Ni d-d transitions present in the UV-vis spectra, likely because the films are too thin to see these low intensity transitions. Interestingly, the UV-vis spectra of $Ni_yAl_{1-y}O_x$ films containing NiO particles show a different spectral shape than that of pure NiO, with increased absorption at lower wavelengths, beginning at ~4.5 eV. This may indicate that some of the Ni atoms are still present in the a-Al_2O_3 phase, resulting in O 2p – Ni 3d transitions that are higher in energy than those of NiO due to the localization of the electronic states on spatially-separated Ni^{2+} cations. Other evidence of the persistence of Ni in the a-Al_2O_3 phase is that the average Ni – O bond length in Figure 2.6c shows a gradual increase from $Ni_{0.1}Al_{0.9}O_x$ to NiO. An abrupt change to the Ni – O bond length in NiO would be expected with $y > 0.1$ if all the Ni atoms were present as NiO, as is seen for $Co_yAl_{1-y}O_x$ films in Figure 2.5d.
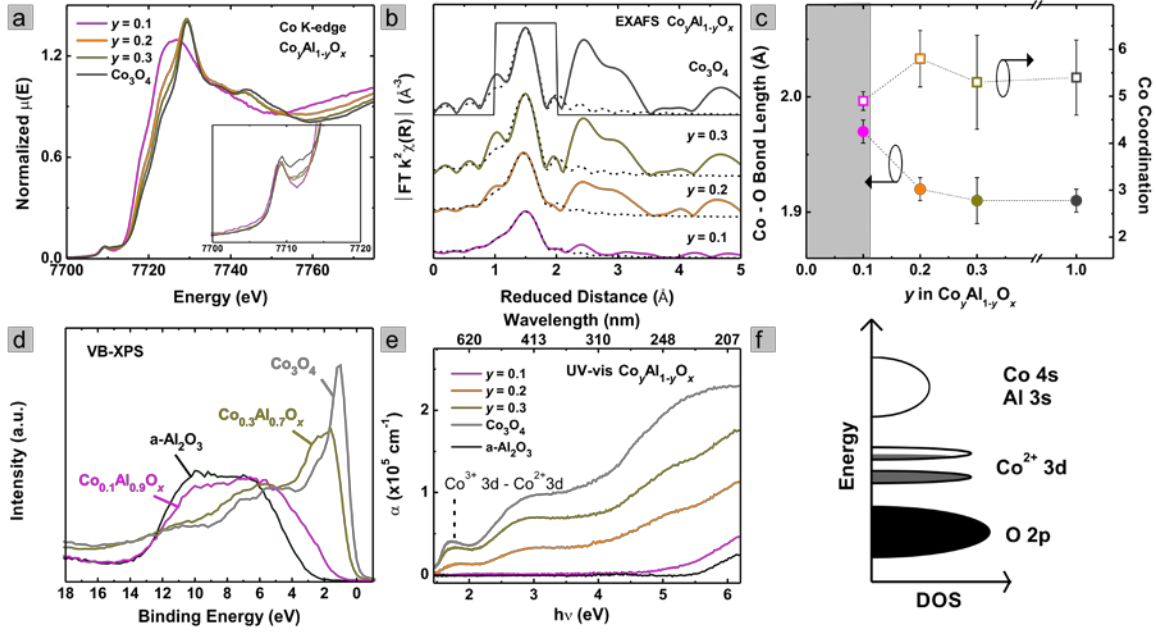
Figure 2.6. Analysis of Ni$_y$Al$_{1-y}$O$_x$ thin films. a) Ni K-edge XANES, b) FT-EXAFS with fits (dashed lines) to the first coordination sphere (solid black line), c) Ni-O bond lengths (closed circles) and coordination numbers (open squares) from EXAFS fits, d) valence band XP spectra, e) UV-vis spectra, and f) schematic DOS diagram of amorphous Ni$_y$Al$_{1-y}$O$_x$ films. The grey shaded region in (d) indicates the amorphous composition range and lines between points are meant to guide the eye. These data show that Ni incorporates as both dispersed Ni^{2+} cations as well as phase-segregated NiO nanoparticles within the Ni$_y$Al$_{1-y}$O$_x$, both giving rise to new optical features and substantial new filled electronic states at the valence band edge.

Based on the energy of the Cu K-edge in Figure 2.7a and the presence of shake-up features in the Cu 2p XPS (Figure A.10), Cu is present as Cu^{2+} in Cu$_y$Al$_{1-y}$O$_x$ films. Similar to films containing Ni or Co, we find Cu$_y$Al$_{1-y}$O$_x$ films are only X-ray amorphous up to low concentrations of Cu, i.e. $y = 0.2$. At $y > 0.2$, tenorite CuO phase separates from the a-Al$_2$O$_3$ (Figure A.1), a slightly higher concentration than our previous work.[27] Unlike Ni or Co, Cu appears to have a slightly larger composition range for forming an amorphous alloy with a-Al$_2$O$_3$, likely due to its lower metal coordination number of ~ 4.2 (Figure 2.7c), and therefore a lower oxygen coordination, C_O. Despite being 4-coordinate, Cu still has a smaller amorphous alloy range than d^0, d^5 or d^{10} cations due to its square planar geometry. This geometry is indicated by the similarity of the XANES region in Figure 2.7a to the tenorite CuO phase, particularly the lack of increase in the

intensity of the pre-edge feature compared to CuO, which would suggest distortion of the square planar geometry.[43]

For $y = 0.1$ the optical absorption edge of $Cu_yAl_{1-y}O_x$ films decreases to 3.5 eV (Figure 2.7e). Simultaneously, there is a shift of the valence band maximum to higher energy, Figure 2.7d, indicating the addition of occupied states to the top of the valence band. The shift of the valence band maximum is approximately equal to the shift of the absorption onset (~1.5 eV), possibly indicating that the new charge-transfer process is from occupied Cu 3d states to unoccupied Al 3s or Cu 4s states. The new absorption process also agrees well with reported values of ligand to metal charge transfer (O 2p to Cu 3d) of CuO.[78] The absorption spectra of amorphous $Cu_yAl_{1-y}O_x$ films are different than crystalline $CuAl_2O_4$,[79] likely due to the different Cu^{2+} and Al^{3+} geometries in the two types of films. At higher Cu contents, $y \geq 0.5$, the optical absorption edge shifts to about 1.5 eV, in agreement with other reports for CuO.[80–82] The transition associated with the absorption edge for CuO has been debated;[82] our data agree well with reported Cu 3d – 3d transitions of square planar Cu in CuO.[78,83]
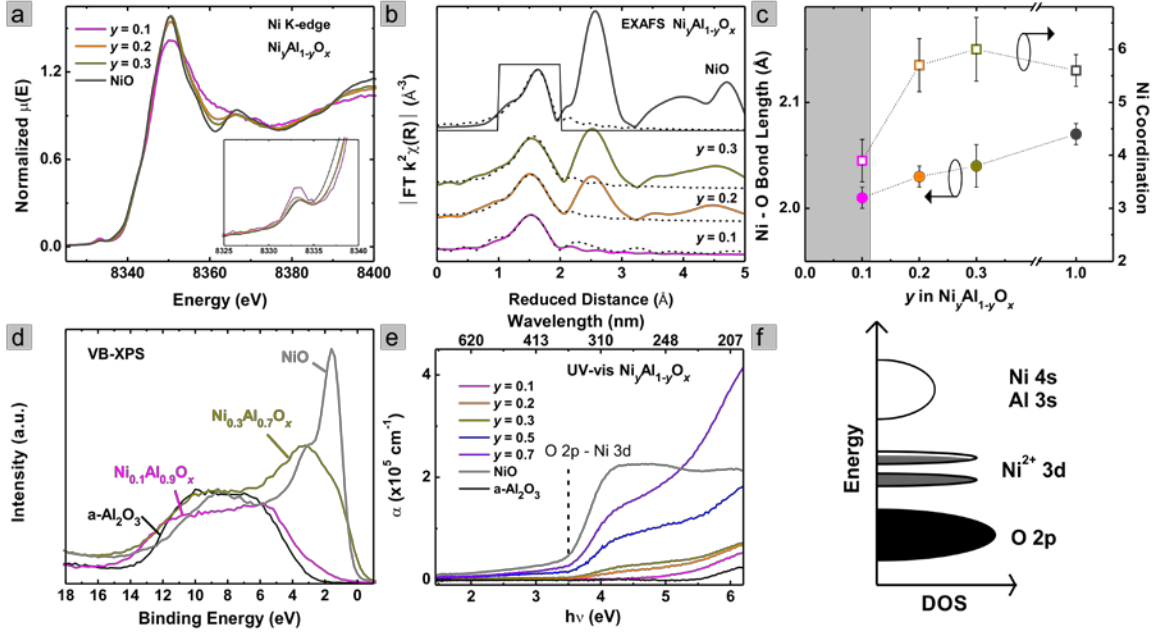

Figure 2.7. Analysis of $Cu_yAl_{1-y}O_x$ thin films. a) Cu K-edge XANES, b) FT-EXAFS with fits (dashed lines) to the first coordination sphere (solid black line), c) Cu-O bond lengths (closed circles) and coordination numbers (open squares) from EXAFS fits, d) valence band XP spectra, e) UV-vis spectra, and f) schematic DOS diagram of $Cu_yAl_{1-y}O_x$ films. The grey shaded region in (d) indicates the amorphous composition range and

25

lines between points are meant to guide the eye. The data show that Cu is maintained in a 4-coordinate square-planar geometry and adds substantial densities of electronic states to the valence band edge that lead to a tunable effective bandgap.

d^{10} Metal Cations. As with d^5 cations, the isotropic d-electron configuration of d^{10} transition metal cations leads to no preference for the octahedral coordination. Therefore, both Zn^{2+} and Ga^{3+} can easily adopt a lower coordination that is conducive to forming an amorphous structure. The presence of Zn^{2+} in $Zn_yAl_{1-y}O_x$ films is confirmed by the Zn K-edge energy in Figure 2.8a as well as Zn 2p XPS (Figure A.11). Zn can incorporate into the a-Al_2O_3 matrix and remain amorphous up to $y = 0.4$ (Figure A.2).[27] This is also demonstrated by the lack of coordination spheres beyond the first shell in the FT-EXAFS in Figure 2.8b. Additionally, the UV-vis spectra for $y \leq 0.4$ show the absorption onset shifts to energies lower than for a-Al_2O_3, but higher than for ZnO, seen in Figure 2.8e. This absorption process for amorphous $Zn_yAl_{1-y}O_x$ films is likely charge transfer from O 2p to Zn 4s orbitals that are localized rather than delocalized as they would be in crystalline ZnO; i.e. there are weak electronic interactions between the spatially well-separated Zn^{2+} ions. The energy of the absorption onset is also different from that of crystalline $ZnAl_2O_4$,[84] presumably due to variations in Zn^{2+} and especially Al^{3+} geometries in the two types of films.

At $y > 0.4$, ZnO particles segregate from the a-Al_2O_3 (Figure 2.8b) and second coordination sphere (Zn-Zn distances) appear in the FT-EXAFS data. The crystalline nature of the ZnO is also apparent in the UV-vis spectra of films with $y > 0.4$ (Figure 2.8e) where the absorption onset shifts to ~ 3.2 eV, consistent with O 2p – Zn 4s charge transfer in ZnO. Similar to $Ni_yAl_{1-y}O_x$ films, there is still increased absorption at lower wavelengths for films containing ZnO particles, likely indicating that some amount of Zn remains in the a-Al_2O_3 phase. At both high and low Zn concentration, the Zn 3d states make no contribution to the occupied states near the top of the valence band, seen in Figure 2.8d. Instead, occupied Zn 3d states are present in the lower valence band of $Zn_yAl_{1-y}O_x$ films. Due to the increased nuclear charge and decreased shielding per electron in the d^{10} configuration, these states are at lower energy than other first row d-orbitals.[85]
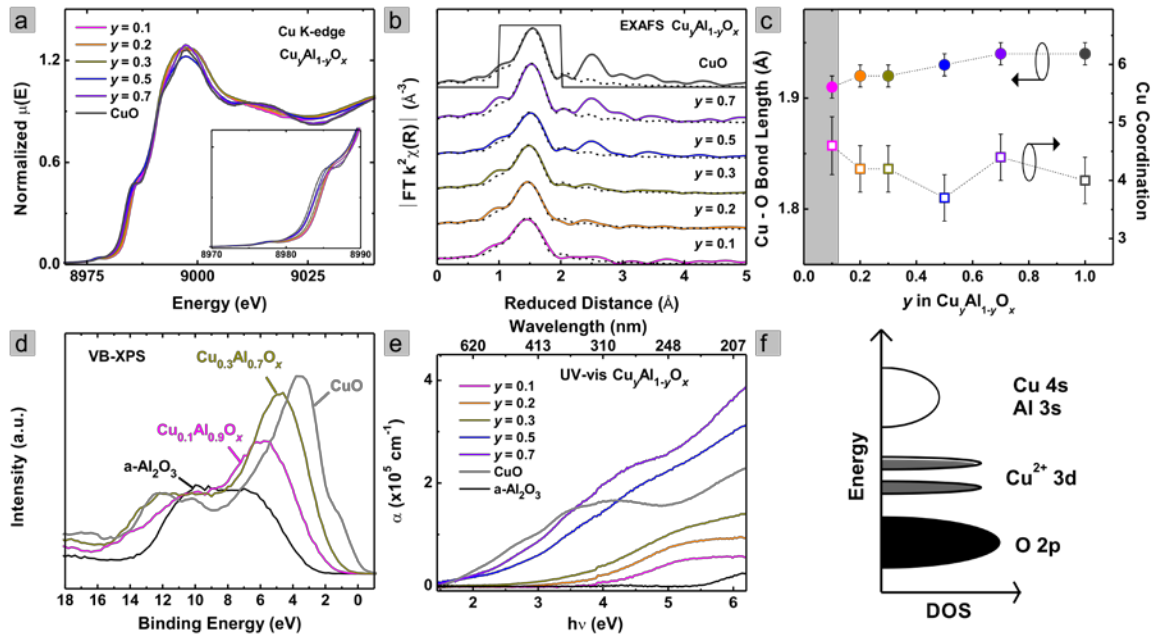
Figure 2.8. Analysis of $Zn_yAl_{1-y}O_x$ thin films. a) Zn K-edge XANES, b) FT-EXAFS with fits (dashed lines) to the first coordination sphere (solid black line), c) Zn-O bond lengths (closed circles) and coordination numbers (open squares) from FT-EXAFS fits, d) valence band XP spectra, e) UV-vis spectra, and f) schematic DOS diagram of $Zn_yAl_{1-y}O_x$ films. The grey shaded region in (d) indicates the amorphous composition range and lines between points are meant to guide the eye.

$Ga_yAl_{1-y}O_x$ films also contain a metal cation with a d^{10} configuration, Ga^{3+}, determined from the Ga K-edge energy in Figure 2.9a and Ga 2p XPS (Figure A.12). Unlike $Zn_yAl_{1-y}O_x$ films, $Ga_yAl_{1-y}O_x$ films remain amorphous at all concentrations of Ga when films are annealed at 450°C. Thermal annealing at 800°C is required to crystallize an all Ga-containing film to β-Ga_2O_3. The amorphous structure of $Ga_yAl_{1-y}O_x$ films is apparent from both XRD (Figure A.2) and FT-EXAFS, shown in Figure 2.9b, where a second coordination sphere cannot be detected. The higher charge on the Ga^{3+} cation compared to the Zn^{2+} cation allows for a lower oxygen coordination, C_O (i.e. the average number of metal cations bound to each oxygen), which likely contributes to the persistence of an amorphous phase. The UV-vis spectra of the $Ga_yAl_{1-y}O_x$ films in Figure 2.9e show that adding Ga up to $y = 0.5$ causes almost no change in the optical absorption onset. This likely indicates that Ga 4s states are localized and similar in energy to the more delocalized Al 3s states. At higher concentration of Ga, the

27

absorption onset shifts closer to that of a-Ga_2O_3, indicating greater delocalization of Ga 4s orbitals.

These data show that the conduction band position of a-Al_2O_3 can be tuned via the concentration of d^{10} cations such as Zn^{2+} and Ga^{3+}, which add unoccupied TM 4s states to the band gap.
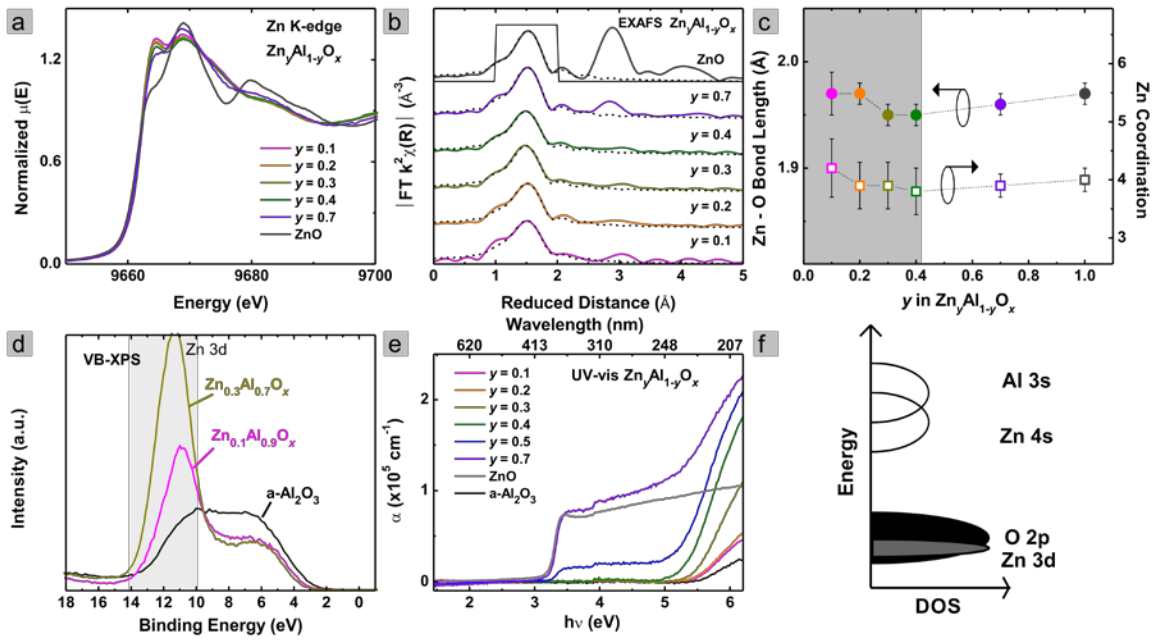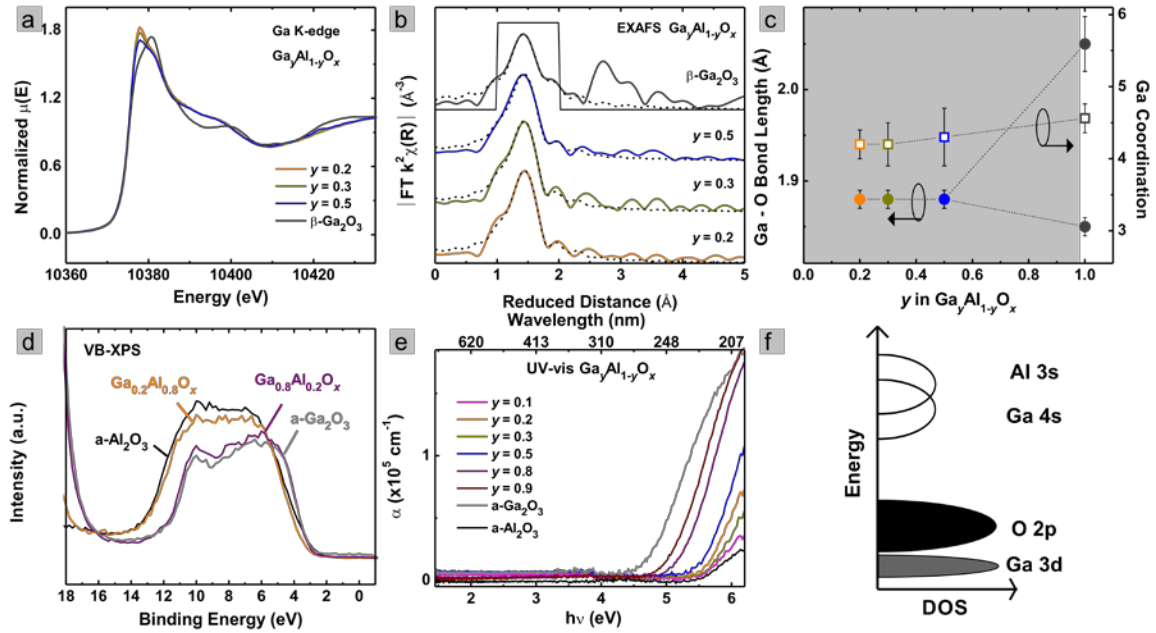

Figure 2.9. Analysis of $Ga_yAl_{1-y}O_x$ thin films. a) Ga K-edge XANES, b) FT-EXAFS with fits (dashed lines) to the first coordination sphere (solid black line), c) Ga-O bond lengths (closed circles) and coordination numbers (open squares) from FT-EXAFS fits, d) valence band XP spectra, e) UV-vis spectra, and f) schematic DOS diagram of $Ga_yAl_{1-y}O_x$ films. The grey shaded region in (d) indicates the amorphous composition range and lines between points are meant to guide the eye.

Tuning the Electronic Structure and Optical Properties

Amorphous and poorly crystalline mixed-metal oxides have garnered much attention recently, in part due to their ability to stabilize metal cations in unique coordination environments that can be useful for applications including catalysis[15,86,87] and controlling charge transport in photovoltaics.[14,88] As interest and utility of these materials grow, it is important to have a guided approach to designing the properties of these materials. From the data presented here, we propose that the chemical properties of the transition metal

cations in mixed-metal oxide thin films can be used to help predict the resulting atomic and, hence, electronic structures.

Number of d Electrons. The d-electron filling of the transition metal can be used to predict the resulting electronic structure and optical properties. Cations with partially filled d-orbitals (e.g. Fe^{3+}, Cr^{3+}, Co^{2+}, Ni^{2+}, Cu^{2+}, etc.) add filled electronic states at the valence band edge of a-Al_2O_3 as well as unfilled electronic states within the a-Al_2O_3 band gap. These added cations in a-Al_2O_3 give rise to strong optical absorption features associated with excitation between the band states of the parent oxide (O 2p and Al 3s) and the new cation states (TM 3d), as well as weaker d-d optical transitions of the incorporated cations. Cations with unfilled d-orbitals (e.g. d^0 configuration such as V^{5+} and Cr^{6+}) do not modify the valence band edge of a-Al_2O_3, but do modify the optical properties by introducing unfilled electronic states below the conduction band of a-Al_2O_3. Cations with the d^{10} electronic configuration, such as Zn^{2+} and Ga^{3+}, introduce new filled electronic states in the valence band, but these are well below the valence band edge in energy. They also introduce new electronic states in the band gap. The energy of these states depends on the concentration of the Zn^{2+} and Ga^{3+}. For example, when Zn^{2+} is at a low concentration the Zn^{2+} cations are well isolated from each other leading to localized 4s-derived electronic states that are much higher in energy than when Zn^{2+} segregates to form ZnO domains in the film.

The d-electron count of a transition-metal cation also serves as a predictor for the crystal field stabilization energy and the octahedral site preference energy, and therefore the ability of the metal to maintain an amorphous structure.[50] When predicting the electronic structure of mixed-metal oxide films made from solution processing, cations with d^0, d^5 or d^{10} electron counts can be incorporated into amorphous main-group metal oxides such as a-Al_2O_3 up to high concentrations, modifying the electronic structure while maintaining the overall amorphous atomic structure. Cations with other d-electron counts incorporated into mixed-metal oxides at high concentrations are likely to form phase-separated transition metal oxides rather than modifying the existing atomic and electronic structure. This result is useful for designing films in which maintaining the amorphous structure and hence ultra-smooth films and interfaces is important for the

application, for example in thin-film semiconducting oxide devices,[3,25] interface layers,[14] or for certain catalytic reactions.[15]

Cation Concentration and Oxidation state. The concentration of the different cations in the films has a large influence on the resulting atomic structure and therefore the electronic structure. At low concentrations of transition metal ions, films are more likely to form solid solutions or alloys that maintain the local structure of the amorphous host material, here a-Al_2O_3. As in the case of low concentration $Co_yAl_{1-y}O_x$ and $Ni_yAl_{1-y}O_x$ films, this may mean the transition metal cation will adopt an oxidation state and/or coordination environment that is different than that of the parent transition metal oxide. For example, in films with $y = 0.1$, Co remains in the 2+ oxidation state with a tetrahedral coordination and in $Cr_yAl_{1-y}O_x$ films more Cr is present as Cr^{6+} (rather than Cr^{3+}) when the total Cr concentration is low. As we have shown, these different local cation coordination environments result in different electronic structure and optical properties.

Exploiting this concentration-dependence of cation oxidation state and local structure could be advantageous for designing thin films with specific electronic structures. For example, Cr^{6+} in CrO_x/Al_2O_3 catalysts has been shown to be more selective for the desired product, isobutene, in oxidative dehydrogenation of isobutane.[89] Catalysts containing Cr^{6+} have also exhibited lower catalytic activity than Cr^{3+} for the same reaction as well as for the combustion of CO and C_3H_6.[90] The ability to control the ratio of Cr^{6+} to Cr^{3+} in these types of catalysts could lead to more-optimal catalytic properties.

Conclusion and Bridge

We have assessed the electronic, optical, and atomic structure of a large range of amorphous and amorphous/polycrystalline mixed-metal oxide thin films. The work forms the basis for applications of such materials, for example in catalysis, as interfacial layers to control charge transport, and more broadly in functional coatings. The ability of the film to maintain an amorphous structure can be predicted based largely on d-electron count of the metal cation. By judicious choice of the metal cations included in the oxide, both the electronic structure and optical properties can be systematically tuned – for

example by adding filled electronic states at the valence band edge, or localized unfilled states in the bandgap of a-Al_2O_3. The results here should also be generalizable to other host oxide systems. For example, both In_2O_3 and Ga_2O_3 can form amorphous structures at low processing temperatures[91,92] and should be amenable to analogous electronic structure modulation by doping with transition metal cations. These oxides have smaller band gaps than Al_2O_3 studied here and therefore offer a different range of applications.

The spectroscopic techniques and methods used in this work are further utilized for characterizing mixed-transition-metal (oxyhydroxides), a similar class of materials. The themes and guiding principles developed in this chapter are likewise used in the following chapters to guide the analysis of these mixed-transition-metal (oxyhydroxides) as oxygen evolution reaction electrocatalysts in aqueous alkaline solution.

CHAPTER III

EFFECTS OF INTENTIONALLY INCORPORATED METAL CATIONS ON THE OXYGEN EVOLUTION ELECTROCATALYTIC ACTIVITY OF NICKEL (OXY)HYDROXIDE IN ALKALINE MEDIA

Chapter III "Effects of Transition-Metal Cations on Nickel (Oxy)hydroxide Activity" contains co-authored material previously published as *ACS Catal.* **2016**, *6*(4), 2416-2423 reproduced with permission. Copyright 2016 American Chemical Society. M. Burke and I conceived of the project. I performed the experiments and analyzed data with help from M. Burke and A. Batchellor. I wrote the paper with help from Prof. Boettcher and editorial assistance from all authors.

Introduction

Solar or electricity driven water electrolysis for the production of hydrogen fuel is a promising renewable energy storage technology.[1–3] The efficiency of water-splitting devices is limited in part by the high kinetic overpotential needed to drive the oxygen-evolution reaction (OER), which is coupled to the production of hydrogen gas.[4–7] The oxidation of water to O_2 proceeds through four electron transfer steps, each of which involves adsorbed intermediates, making the reaction dependent on multiple parameters and the catalytic mechanism difficult to study.[8] Generally, the reaction proceeds through oxygen-based intermediates adsorbed to metal-cation active sites.[9,10] The binding strength of these intermediates to the metal active site is thought to dictate catalytic activity, and thus the M – O bond strength is used as an activity descriptor.[6,11] If the M – O bond is too strong, the OER is rate-limited by product desorption, and if too weak, by precursor or intermediate binding.[10,12] Considerable effort has been made over several decades to find earth-abundant electrocatalysts with optimal M-O bond strengths that can decrease both the OER overpotential and the cost of water electrolysis systems.[13–20]

We have previously identified $Ni(Fe)O_xH_y$ as the most-active known OER catalyst in alkaline media,[13] and found that NiO_xH_y without Fe is a poor OER catalyst (note we use a general formula here so as not to specify a specific oxidation or

32

protonation state).[14,21,22] Further studies in the rigorous absence of Fe impurities of the single-transition-metal (oxy)hydroxides showed new activity trends, $FeO_xH_y > CoO_xH_y > NiO_xH_y > MnO_xH_y$,[22] with Fe present in all high activity OER catalysts, e.g. $Ni(Fe)O_xH_y$ and $Co(Fe)O_xH_y$).[21] $Ni(Fe)O_xH_y$ can be further optimized and deposited with high loading using a pulsed electrodeposition that ensures uniform Fe incorporation and compact morphology with good electrical interconnection[23] and with similar performance to more-complicated composite architectures.[24–27]

One way to better understand the OER activity enhancement upon Fe addition to NiO_xH_y is to study other incorporated cations. If other cations have similar properties to Fe, or analogous electrochemical behavior in NiO_xH_y, this would provide insight into the mechanism of the activity enhancement by Fe. Additional cations may also provide avenues to further enhance activity, electrical conductivity, or chemical stability. Such binary $Ni_{1-z}M_zO_xH_y$ OER catalysts (M is a metal cation) have been studied to identify synergistic effects, particularly for metals such as Co and Fe.[13,28–38] Previous studies also report a decrease in the OER overpotential upon La or Ce addition to NiO_xH_y.[28,34] Corrigan reported that the addition of La or Ce dopants induce a similar or lower overpotential to that of Fe in $Ni_{1-z}M_zO_xH_y$ at 16 mA cm^{-2}.[28]

A challenge in studying other cations in NiO_xH_y is the potential for Fe contamination. Nickel oxides and (oxy)hydroxides have long been studied for OER catalysis,[13,39–42] but, as discussed above, unintentional incorporation of Fe from even the purest commercially available electrolytes is responsible for the high catalytic activity reported.[14,16,43] For example, the increased catalytic activity reported[39,44–46] for β-Ni(OH)$_2$/β-NiOOH relative to α-Ni(OH)$_2$/γ-NiOOH has been shown to be due to Fe impurity incorporation during the aging step to form the β-Ni(OH)$_2$/β-NiOOH phase.[14,47] Due to the ease of Fe incorporation into NiO_xH_y, previous studies on Ni-based catalysts with other intentionally incorporated cations in alkaline conditions may have Fe contamination, convoluting the true trends in activity. The effects of incorporation of other cations into NiO_xH_y must be studied in rigorously Fe-free conditions.

In some previous studies of $Ni_{1-z}M_zO_xH_y$, it has been suggested that an anodic shift of the $Ni^{2+/3+}$ oxidation peak potential is connected to increased OER activity.[14,30,48] One hypothesis is that if it is more difficult to oxidize Ni^{2+}, possibly due to charge

33

transfer to Fe cations, the oxidized Ni cation will be able to better oxidize water.[14,30,49] This "electron-withdrawing effect" hypothesis assumes the host matrix cation (Ni or Co) is the active site. In support of this view, Corrigan and Bendert found that the addition of La and Ce increased the $Ni^{2+/3+}$ oxidation peak potential and decreased the OER overpotential,[28] but the degree to which these samples contain Fe impurities is unclear. CoO_xH_y also incorporates Fe to become more active (on a total-metal-cation basis) with a concurrent anodic shift in the $Co^{2+/3+}$ oxidation peak potential.[15] Recent work, however, has provided compelling evidence that Fe cations are the active sites within Ni/CoO_xH_y matrices and adding Fe largely simply increases the number of active sites.[15,22,50–52] In this case, other cations that increase the $Ni^{2+/3+}$ oxidation potential would not lead to higher activity unless they too are more-active than the Ni sites.

Here we report effects of Ti, Mn, La, and Ce cation incorporation on the OER activity and $Ni^{2+/3+}$ oxidation potential of $Ni_{1-z}M_zO_xH_y$ in Fe-free alkaline solution using cyclic voltammetry in combination with electrochemical quartz-crystal microgravimetry. Metal cations were chosen based on either previous reports of high activity,[26,28,34] i.e. La and Ce, similar d-orbital filling to Fe,[17,18,38,53] i.e. Mn, or anticipated ability to shift the $Ni^{2+/3+}$ oxidation peak to higher potentials without increasing activity,[54,55] i.e. Ti. We prepared mixed $Ni_{1-z}M_zO_xH_y$ films by both solution spin-casting and electrodeposition. While we focus our analysis on the spin-cast films, the same behavior is observed on the electrodeposited films indicating the activity trends are intrinsic to the compositions and not dependent on synthesis method. The thin films (~ 20 nm thick, or a loading of 4 µg cm^{-2}) used allow for estimation of intrinsic activities of the mixed metal hydroxide films with minimal complication from other factors (e.g. electronic conductivity, mass transport, and inefficient catalyst utilization).[13,22,51,56] We show that only Ce enhances the OER activity of NiO_xH_y in 1 M Fe-free KOH, although the enhancement is much less than with Fe and is also transient. We also find no strong correlation between activity and the $Ni^{2+/3+}$ redox potential. These results highlight the uniqueness of Fe and are consistent with Fe being the active site for the OER in $Ni(Fe)O_xH_y$. Understanding the effects of dopants on the activity of OER catalysts will help guide the design of improved catalysts.

34

Experimental

Spin Cast Film Deposition. NiO_xH_y films were fabricated by both spin coating from precursor solutions and from cathodic electrodeposition. Films were spin cast from solutions of 0.1 M $Ni(NO_3)_2 \cdot 6H_2O$ (99.9985% Strem) in 1:1 (v/v) mixture of ethanol and water onto Au/Ti or Pt/Ti 5 MHz AT-cut quartz crystal microbalance (QCM) substrates (1.38 cm^2) from Stanford Research Systems. QCM substrates were sonicated in a solution of Contrad 70 (5% v/v) at 40 °C for 20 min followed by rinsing with water (18.2 $M\Omega \cdot cm$). The electrode surface was then rendered hydrophilic with a 10 min O_2 plasma etch. About 0.25 mL of metal nitrate salt solution was deposited onto the substrates through a 0.1 µm filter and films were spun at 3000 rpm for 30 s. Substrates were then immediately transferred to a hot plate at 150 °C and annealed for 10 min. Spin-cast $Ni_{1-z}M_zO_xH_y$ films with Ti, Mn, La, Fe and Ce were prepared in the same manner by mixing the appropriate amount of $TiOSO_4 \cdot xH_2O$, $Mn(NO_3)_2 \cdot xH_2O$, $Fe(NO_3)_3 \cdot 6H_2O$ $La(NO_3)_3 \cdot 6H_2O$, or $Ce(NO_3)_3 \cdot 6H_2O$ with the $Ni(NO_3)_2$ to obtain added metal concentrations of nominally 10 and 30 at. % (on a total metals basis). The as-deposited mass of each film was obtained by measuring the frequency of the crystal before and after deposition and converting the change in frequency to mass using the Sauerbrey equation[57] $\Delta f = -C_f \times \Delta m$, where Δf is the observed frequency change (Hz), C_f is the sensitivity factor of the 5 MHz AT-cut quartz crystal (56.6 Hz μg^{-1} cm^2) and Δm is the change in mass per unit area (μg cm^{-2}). To ensure viscoelastic effects of film damping were not affecting the validity of the Sauerbrey relationship we measured the crystals' resonance behavior using impedance spectroscopy before and after film deposition in air and in 1 M KOH – the resonator quality factor was unaffected by the addition of the film. We have also previously shown that the mass loadings determined by QCM measurements are consistent with those determined by integration of the Ni redox wave for wide range of film thicknesses.[23] Total metal content was determined by assuming complete $Ni(OH)_2$ formation, accounting for added cations substituting for Ni. Typical films loadings were 4 – 5 μg cm^{-2} which is ~10-20 nm in thickness, based on calculations using the mass loading and density of $Ni(OH)_2$.

Electrochemical Film Deposition. Electrodeposited NiO_xH_y films were deposited directly onto the QCM substrates from 0.1 M aq. $Ni(NO_3)_2$. Deposition was performed in a two-electrode glass cell with a carbon-cloth counter electrode (Fuel Cell Earth) by applying 1 mA cm^2 of cathodic current for 30 to 90 s (the time was varied to achieve the same mass loading as the spin-cast films). $Ni_{1-z}M_zO_xH_y$ films were electrodeposited in the same fashion by mixing the appropriate amount of transition-metal-nitrate salts (or the chloride salt in the case of Fe) in the deposition solution to obtain 10% in the films (see Table B.1) and varying the cathodic current density (-0.1 to -1 mA cm^{-2}) if necessary to obtain full coverage. Ti-incorporated NiO_xH_y films could not be electrodeposited due to formation of a gel-like film with poor adhesion to the electrode surface. The as-deposited mass for each of the electrodeposited films was determined based on the frequency change of the QCM crystal in a beaker of water (18.2 MΩ·cm) measured directly before and after deposition.

Electrochemical Characterization. Following deposition, NiO_xH_y and $Ni_{1-z}M_zO_xH_y$ films were characterized electrochemically by cycling in 1.0 M KOH (semiconductor grade 99.99% trace metal basis) that had been cleaned of Fe impurities using high-purity precipitated $Ni(OH)_2$ as an Fe-absorbent following our reported method.[14] Cyclic voltammograms (CVs) at 20 mV s^{-1} and steady-state chronopotentiometry measurements (Tafel analysis) were recorded using a BioLogic SP200 or SP300 potentiostat in a polymethylpentene three-electrode cell with a Pt-wire counter electrode, Hg/HgO (CH Instruments) reference electrode, and QCM working electrode (Stanford Research Systems). The electrolyte was continuously stirred to remove bubbles from the working electrode surface and high-purity O_2 was continuously bubbled through the solution before and during the measurements. All results shown here have been corrected for uncompensated series resistance of the electrolyte based on electrochemical impedance measurements taken after cycling each film. Uncompensated resistances were 4-7 Ω. Current density was calculated based on the 1.38 cm^2 geometric surface area of Au on the QCM electrodes. Turnover frequencies (TOFs) are calculated based on the average of the forward and reverse current from the CV at a specific overpotential and the total number of metal centers (TOF_{tm}) obtained from microbalance measurements accounting

36

for the percentage of added transition metal. TOF_{tm} reported implicitly assume all metal cations are active sites, and thus represent lower limits. To determine whether all the films had similar internal electrolyte-accessible surface area we compared the integrated charge in the nominally $Ni^{2+/3+}$ redox wave (Figure B.1). Most of the films showed variations of less than a factor of 2 and 75 +/- 25% of the Ni cations electrochemically accessible. The $Ni(Ce)O_xH_y$ films showed the lowest fraction of accessible Ni Cations ~30%, indicating that the TOF_{tm} are slightly under estimated for the $Ni(Ce)O_xH_y$. In situ mass measurements were based on the frequency change of the crystal starting with the point at which the crystal was first immersed in the electrolyte.

Physical Characterization. The morphology of each film was examined by scanning electron microscopy (SEM) on a Zeiss Ultra 55 at 5 keV with an in-lens detector. X-ray photoelectron spectroscopy (XPS) was used to determine the overall composition of the films. XPS was performed on a ThermoScientific ESCALAB 250 using a monochromatic Al Kα (150 W, 20 eV pass energy, 500 µm spot size) or non-monochromated Mg Kα (200 W, 40 eV pass energy) source. An in-lens electron flood gun was used for charge neutralization of the samples. Spectra were analyzed using ThermoScientific Avantage 4.75 software and the binding energy was calibrated using the adventitious C 1s peak at 284.8 eV. Stoichiometries of the films are those obtained from XPS measurements on one representative sample of each composition. Fe impurity concentrations were also determined for NiO_xH_y and $Ni_{0.95}Ce_{0.15}O_xH_y$ films using an ION-TOF Model IV time-of-flight secondary ion mass spectrometer (ToF-SIMS) with a Bi^+ primary ion, O_2 sputter source operating at 1 keV, and a flood gun for charge neutralization, all operating in interlaced mode. Concentrations were calculated based on comparisons to the signal intensity in ToF-SIMS of a spin-cast $Ni_{0.98}Fe_{0.02}O_xH_y$ control film (2% Fe intentionally added in the deposition solution which was confirmed by XPS of the film).

Results and Discussion

Dependence of Film Morphology on Added Cation Identity. SEM imaging of the solution spin-cast films shows similar morphology (Figure 3.1). The films are 10 to 20 nm in

thickness (estimated from the as-deposited mass). The NiO_xH_y, $Ni_{0.9}Mn_{0.1}O_xH_y$, $Ni_{0.93}La_{0.07}O_xH_y$, and $Ni_{0.9}Ti_{0.1}O_xH_y$ films all show a rough, sponge-like morphology, with small cracks revealing the gold substrate underneath the film. The $Ni_{0.85}Ce_{0.15}O_xH_y$ and $Ni_{0.9}Fe_{0.1}O_xH_y$ films have a more platelet-like morphology and better coverage of the underlying substrate. It is unlikely that these small differences account for order(s) of magnitude differences in activity (discussed below). The morphologies of spin-cast $Ni_{1-z}M_zO_xH_y$ films at $z \approx 0.1$ are similar to those at $z \approx 0.3$ (Figure B.2) and they are also similar to the electrodeposited films (Figure B.3). This similarity to the electrodeposited films (which form by local pH gradients driving metal hydroxide precipitation) is explained by the fact that the spin-cast films are annealed only at a low temperature of 150 ºC. This temperature is not sufficient to completely decompose the salt counter ions and form crystalline oxides. Upon immersion of the precursor film in KOH, the hydroxides likely exchange with the remaining precursor counter ions leading to local precipitation in the film of the (oxy)hydroxide phases. Electrochemical cycling likely speeds this transformation process.
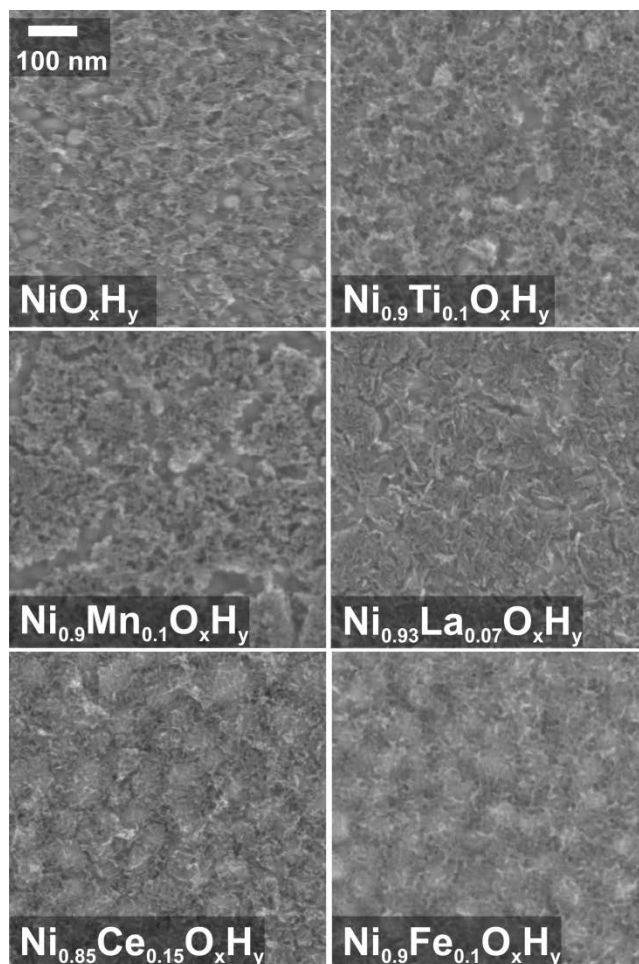
Figure 3.1. SEM images of spin-cast films after 50 cycles between 0.2 and 0.85 V vs. Hg/HgO in Fe-free 1 M KOH at 20 mV s^{-1}.

Effects of Added Cations on OER Activity. The voltammetry in Figure 3.2 shows that Fe has the most pronounced effect on $Ni_{1-z}M_zO_xH_y$ electrochemical behavior. $Ni_{1-z}Fe_zO_xH_y$ has the lowest OER onset potential and the lowest overpotential at 3 mA cm^{-2} at $z \sim 0.1$ and 0.3. The $Ni_{0.7}Fe_{0.3}O_xH_y$ films have the best performance, consistent with previous reports.[14,47,50,58] Besides Fe, Ce is the only other cation tested that significantly increases the OER activity, but this activity decays with time, as discussed below. Ti, Mn, and La have little effect on the activity of $Ni_{1-z}M_zO_xH_y$, which is different than previously reported.[26,28,33,34,38] We have previously shown NiOOH to be sufficiency electrically conductive under OER conditions (0.1 – 0.2 S cm^{-2}), such that the electrical iR drop

39

across the thin films studied here would be negligible. Given that the films here are largely composed of NiOOH, we thus expect the observed differences in electrochemical behavior to not be due to differences in film electrical conductivity.
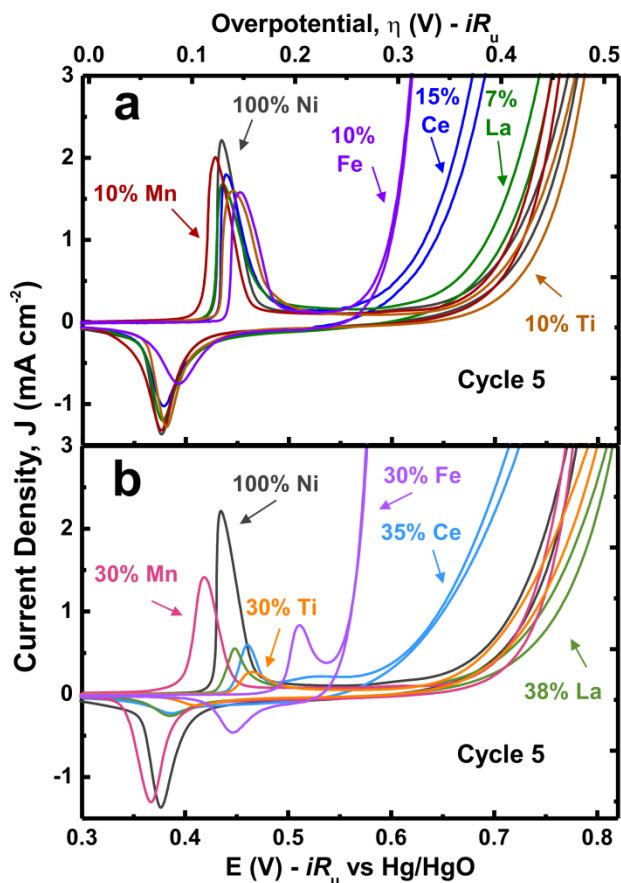
Figure 3.2. Voltammetry of spin-cast $Ni_{1-z}M_zO_xH_y$ films, where M is a metal cation, at approximately a) $z \approx 0.1$ and b) $z \approx 0.3$ in Fe-free 1 M KOH at 20 mV s^{-1}. For the initial cycle 1 scans, see Figure B.4.

In Figure 3.3, the OER activities of the different films are quantified at an overpotential of 400 mV. The activity is calculated as a total metal turnover frequency (TOF_{tm}), which we define as moles of O_2 per mole of metal per second. Here, both Ni and added metal cation are included in the moles of metal for the TOF_{tm} calculation, and the number of moles is determined from the in situ mass from the QCM working electrode. The moles of O_2 are determined from the amount of current, through

40

Faraday's constant and assuming a four electron transfer, taken from the average of the forward and reverse scan of the cyclic voltammetry at 20 mV s^{-1} in 1 M KOH. We note that this is not a steady-state TOF_{tm}, but it is reasonable for comparisons of the films to each other. Figure 3.3 shows that the activities of $Ni_{0.85}Ce_{0.15}O_xH_y$ and $Ni_{0.65}Ce_{0.35}O_xH_y$ films are initially (i.e. after cycle 5) about a factor of 8 and 4 higher than that of NiO_xH_y, respectively. However, after 50 cycles, the performance decreases, and the activity of $Ni_{0.85}Ce_{0.15}O_xH_y$ is only a factor of 2 higher than NiO_xH_y and $Ni_{0.65}Ce_{0.35}O_xH_y$ is statistically equivalent to NiO_xH_y. This decrease in activity over the course of 50 cycles for $Ni(Ce)O_xH_y$ films is double that of the other films, which, on average, decay in activity by only a factor of 2. By contrast, $Ni_{1-z}Fe_zO_xH_y$ films retain their activity throughout 50 cycles. The activity enhancement from Ce incorporation into NiO_xH_y is a transient effect. The same is observed for the electrodeposited $Ni(Ce)O_xH_y$ films. This is consistent with the work of McCrory et al.,[33,34] which shows a decrease in the OER current density of electrodeposited $Ni(Ce)O_xH_y$ over time, but different in that we find high initial activity for $Ni(Ce)O_xH_y$.
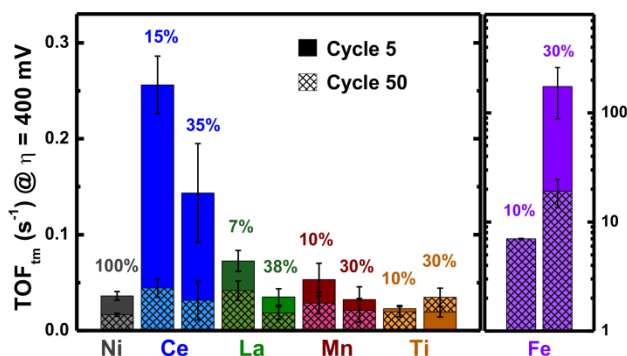
Figure 3.3. OER turnover frequency of spin-cast films at 400 mV overpotential at cycle 5 (solid) and cycle 50 (pattern) in Fe-free 1 M KOH from voltammetry data collected at 20 mV s^{-1}. In the case of $Ni_{0.9}Fe_{0.1}O_xH_y$ there is no activity decrease over 50 cycles and the error bars small and not visible on this scale . TOF_{tm} are calculated assuming all metal cations are active (and thus are lower limits) and the OER current is taken as the average of the forward and reverse scans. Values reported are the average and error bars are the standard deviation of 3 samples. Note the different scale on the y-axis for $Ni_{1-z}Fe_zO_xH_y$ films.

Transient Activity Enhancement from Ce Addition. At 15% concentration, Ce initially decreases the overpotential for the OER on $Ni_{0.85}Ce_{0.15}O_xH_y$, with an OER onset

potential only 40 mV higher than that of $Ni_{0.9}Fe_{0.1}O_xH_y$ (Table B.2). However, the current does not rise as sharply for $Ni_{0.85}Ce_{0.15}O_xH_y$ films (see Figure 3.2) resulting in decreased performance at higher overpotentials compared to $Ni_{0.9}Fe_{0.1}O_xH_y$. Unlike 30% Fe addition to $Ni_{1-z}M_zO_xH_y$, higher Ce concentration (~35%) does not result in further performance improvement and in fact decreases it compared to 15%. These results are inconsistent with those of Corrigan and Bendert, who report a lower overpotential at 16 mA cm^{-2} for $Ni(Ce)O_xH_y$ than $Ni(Fe)O_xH_y$.[28] The results are consistent with McCrory et al.[33,34] who showed that $Ni(Ce)O_xH_y$ has a higher overpotential at 10 mA cm^{-2} compared to NiO_xH_y, but exhibit higher current densities at lower overpotentials (~350 mV) on glassy carbon electrodes. We show that initially both $Ni_{0.85}Ce_{0.15}O_xH_y$ and $Ni_{0.65}Ce_{0.35}O_xH_y$ are more active than pure NiO_xH_y. After 50 cycles only $Ni_{0.85}Ce_{0.15}O_xH_y$ remains more active, by about a factor of 2 (Figure B.5). Continued cycling would likely decrease the OER activity of $Ni_{0.85}Ce_{0.15}O_xH_y$ until it is equal to or lower than that of NiO_xH_y, as observed during the steady-state Tafel analysis (Figure 3.4a).

Mechanisms of Ni(Ce)O_xH$_y$ Deactivation.   In order to understand the cause of the transient enhancement from Ce addition, $Ni(Ce)O_xH_y$ films were characterized by XPS before and after 50 CVs in 1 M KOH. One hypothesis is that gradual dissolution of Ce from the $Ni(Ce)O_xH_y$ films may be the cause of the decrease in activity with cycling. However, the as-deposited and post-electrochemistry films have comparable Ce concentrations (by XPS), 18% and 15% relative to Ni, respectively. The lack of Ce dissolution is also corroborated by the minimal change in film mass after 1 h under OER conditions (Figure 3.4b). Ce is not expected to be highly soluble under alkaline OER conditions based on thermodynamic Pourbaix diagrams, which show CeO_2 as the predominant phase.[59,60]
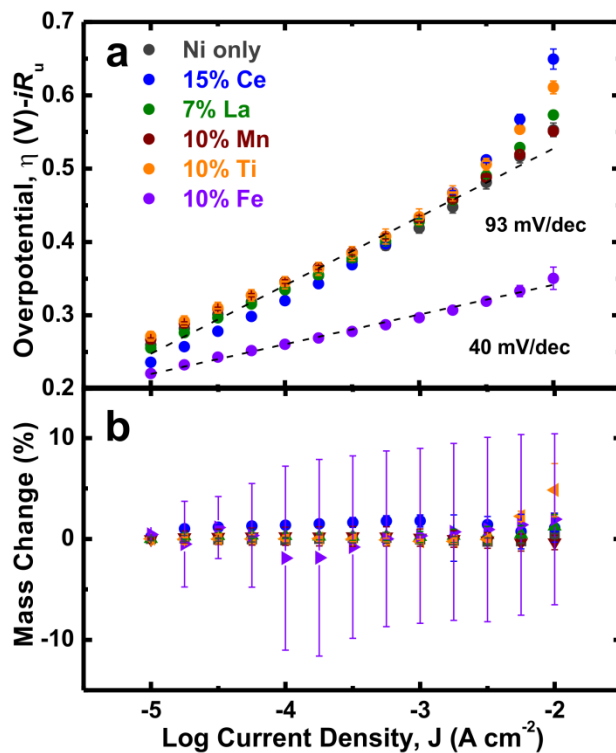
Figure 3.4. a) Tafel plots for spin cast $Ni_{1-z}M_zO_xH_y$ films along with b) in situ mass change over the course of hour-long Tafel measurements. Each chronopotetniometry step, starting at low current density, is held for 3 min with the exception of the first two steps, which are held for 10 min each. Dashed lines are meant to guide the eye and be representative of the Tafel slopes calculated. Data points are the average and error bars are the standard deviation of 3 individual samples. Some error bars are smaller than the symbols. Actual Tafel slopes are listed in Table B.3 and individual plots shown in Figure B.6.

Another hypothesis for the decaying activity of $Ni(Ce)O_xH_y$ films is CeO_2 phase segregation in the film during electrochemical measurements such that active sites relying on Ni-O(H)-Ce motifs are eliminated. There is evidence to support this hypothesis from the O 1s XP spectra of the $Ni(Ce)O_xH_y$ films. The as-deposited films (Figure B.7) show only hydroxide character where-as after cycling the films with Ce exhibit oxide character, evident from the O 1s peak shape and binding energy in the XP spectra (Figure 3.5). This suggests that the Ce^{3+} ions (which are present in the deposition solution and as-deposited films, Figure B.8) are better distributed in the $Ni(OH)_2$ lattice at the start of electrochemical characterization. After cycling, phase-segregated CeO_2 nanoparticulates in the $Ni(OH)_2$ film may form, which have been reported before for

43

related Ni-based films.[61,62] Haber et al. found that CeO_2 segregated from $NiCoFeO_x$ in mixed $NiCeCoFeO_x$ films, although we note that those films were annealed at higher temperatures (300 °C) than here (150 °C) and thus are composed primarily of oxides.[63] Of all the films studied, $Ni(Ce)O_xH_y$ has the most oxide character (Figure 3.5). Since CeO_2 is not apparent in the as-deposited films, phase segregation (likely driven by Ce^{3+} oxidation) is probably responsible for the decrease in performance of the $Ni(Ce)O_xH_y$ with cycling. More analytical work is needed to confirm this hypothesis, for example by synchrotron x-ray absorption measurements, as traditional analyses by electron microscopy or diffraction are challenged by the largely amorphous and disordered thin-film structures.

We also note that our hypothesis on Ce-enhancement is different than that of Haber et al., where the nominally high OER activity of $NiCeCoFeO_x$ films was attributed to the presence of CeO_2 nanoparticles.[63] However, those films show CeO_2 phase segregation as-deposited and also have high concentrations of Fe. The electrodeposited $NiCeCoFeO_x$ films in that work (which are less likely to have CeO_2 phase segregation as-deposited) show a similar decrease in activity during cycling, consistent with our hypothesis that phase segregation of CeO_2 accounts for the transient OER activity of $Ni(Ce)O_xH_y$ films.
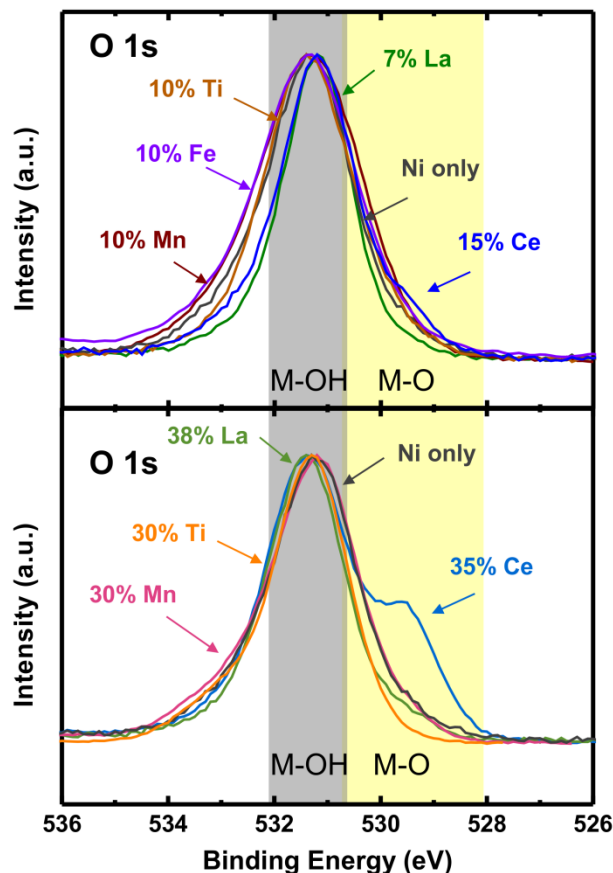
Figure 3.5. O 1s XP spectra for $Ni_{1-z}M_zO_xH_y$ films after 50 cycles in Fe-free 1 M KOH at 20 mV s^{-1} showing the increased oxide character of $Ni(Ce)O_xH_y$ films compared to the other mixed metal films. The grey shading indicates the range of metal hydroxide O 1s binding energy and the yellow shading indicates that of metal oxides.[64]

Effects of Ti, Mn, and La on NiO$_x$H$_y$ OER Activity. In contrast to the three and one order(s) of magnitude activity enhancement from Fe and Ce, respectively, the Ti, Mn, and La cations have little effect on the OER activity of NiO$_x$H$_y$. Addition of 7% La results in only a 20 mV decrease of the OER onset potential compared to NiO$_x$H$_y$ (Table B.2). The performance of the $Ni_{0.93}La_{0.07}O_xH_y$ catalyst is considerably worse than that reported by Corrigan,[28] but slightly better than that reported by McCrory et al.[33,34] The OER activity of $Ni_{0.93}La_{0.07}O_xH_y$ films are about a factor of two higher than NiO$_x$H$_y$ at both cycle 5 and 50. Addition of 38% La results in a decrease in OER performance with the films exhibiting higher overpotentials than NiO$_x$H$_y$ films at all current densities.

45

Addition of Mn to NiO_xH_y did not result in a significant increase in OER activity, consistent with some previous reports for electrodeposited films,[22,28] but in contrast to that of Diaz-Morales et al.[38] With ~10% Mn there is only a slight decrease in overpotential. As with La and Ce, a higher concentration of Mn, ~ 30%, results in decreased performance compared to NiO_xH_y. This is in contrast to higher concentrations (~30%) of Fe, which lead to improved OER activity.

Unlike the other added cations, incorporation of 10% Ti resulted in higher overpotentials and lower activity than NiO_xH_y films, shown in Figures 3.2 and 3.3, respectively. Interestingly, higher amounts of Ti slightly increased performance, with $Ni_{0.7}Ti_{0.3}O_xH_y$ films exhibiting higher activity than $Ni_{0.9}Ti_{0.1}O_xH_y$ films, but not higher than NiO_xH_y films. Unlike the other films tested, $Ni_{0.7}Ti_{0.3}O_xH_y$ films increase in activity with cycling. We attribute this to the denser nature of the as-deposited film (likely due to crosslinking from the reactive Ti precursor) blocking access to some of the Ni sites. With cycling, the film becomes hydrated and more-permeable to electrolyte, allowing for catalytic participation from more of the metal sites. This hypothesis is supported by the fact that the charge in the $Ni^{2+/3+}$ wave increases with cycling for $Ni_{0.7}Ti_{0.3}O_xH_y$ films (Figure B.9).

Analysis of Fe Impurities. A number of experiments were performed to show that the results presented here are due to the intentionally incorporated cations in NiO_xH_y rather than Fe impurities that could originate from precursors salts or electrolytes. All compositions were found to be free of Fe contamination by XPS (Mg Kα excitation) after electrochemical characterization (Figure B.10). Spin-cast NiO_xH_y and $Ni_{0.85}Ce_{0.15}O_xH_y$ films were further checked for Fe contamination using ToF-SIMS and were found to contain 0.025 and 0.05% Fe, respectively, relative to total metal content. The same films showed no Fe by XPS, confirming the lower sensitivity limit of ToF-SIMS. We do not believe that this small difference in Fe content between the two catalysts accounts for the ten-fold OER activity difference.[14,43] First, the transient nature of the activity enhancement from Ce suggests that it is not due to the presence of Fe, because the Fe enhancement is stable. Second, Corrigan conducted an analysis of Fe impurities in Ni oxide electrodes and did not find a tenfold activity enhancement until >1% Fe.[43] Third,

the Tafel slopes of $Ni(Ce)O_xH_y$ films are not lower than that of NiO_xH_y. We also note that trace Fe has been shown to dramatically activate Au substrates for OER, but we do not see any activation of the Au substrate (Figure B.11), indicating it is not affecting our results.[14,15,51,65] We found the same increased OER activity of $Ni(Ce)O_xH_y$ compared to NiO_xH_y on Pt substrates (which are not enhanced by Fe impurities)[51] suggesting that substrate activation of the catalyst material is not playing a significant role in the observed trends (Figure B.12). We also find that CeO_x alone mildly activates Au for OER, but is substantially less active than $Ni(Ce)O_xH_y$ or NiO_xH_y (Figure B.13).

Tafel Behavior and Stability. Steady-state Tafel analysis was performed on the films with 10% added metal cations as well as the pure NiO_xH_y (Figure 3.4a). Only the addition of Fe lowers the Tafel slope of NiO_xH_y. We find $Ni_{0.9}Fe_{0.1}O_xH_y$ has a slope of ~40 mV dec^{-1}, which is consistent with other reports[23,58] for ~10% Fe in NiO_xH_y. NiO_xH_y alone has a higher Tafel slope of ~93 mV dec^{-1}. This suggests a difference in the rate-limiting step of oxygen evolution on $Ni_{0.9}Fe_{0.1}O_xH_y$ and NiO_xH_y catalyst films.[66,67]

The other cations (La, Ti, Mn, and Ce) have little effect on the Tafel slope. For La, Ti, and Mn, the Tafel slope is not statistically different from that of NiO_xH_y. Determining the Tafel slope of $Ni_{0.85}Ce_{0.15}O_xH_y$ is complicated due to the rapidly decreasing activity (Figure B.6). $Ni_{0.85}Ce_{0.15}O_xH_y$ is marginally better than NiO_xH_y at low overpotentials, but worse at high overpotentials (Figure 3.4a). Because the Tafel data was collected from low to high overpotential these results are explained by the instability of the $Ni_{0.85}Ce_{0.15}O_xH_y$ discussed above.

The chemical stability of the films was determined by monitoring the film mass during chronopotentiometry steps of the Tafel analysis (Figure 3.4b) as stability during cycling is difficult to ascertain due to movement of ions/ solvent into and out of the film during oxidation/reduction (Figure B.14). All the films were stable and insoluble during the ~1 h of chronopotentiometry measurements. NiO_xH_y along with La, Mn, and Ce-incorporated films have a mass change of less than ± 3%. The $Ni_{0.9}Fe_{0.1}O_xH_y$ films were more variable, but exhibited an overall mass change of ± 10%. We note that the differences in mass change could be the result of variable amounts of NO_3^- (and SO_4^{2-} for

Ti films) left in the films after spin coating, which may not be fully removed before the Tafel analysis as well as Ni^{2+} ions left in the 1 M KOH after cleaning with $Ni(OH)_2$.

Cation Influence on Electronic Structure. It has been hypothesized that an electron withdrawing effect on NiO_xH_y, either by added cations or a noble metal substrate, increases the ability of NiO_xH_y to catalyze water oxidation.[14,30,39] For example, one hypothesis for Fe enhancement is that charge transfer from Ni to Fe makes it more difficult to oxidize NiO_xH_y (evident from the anodic shift of the $Ni^{2+/3+}$ oxidation peak) therefore giving it more oxidizing power and faster OER kinetics.[14,30] The formal potential $E^{0'}$ for the Ni redox wave may thus be a activity descriptor. Recently, Haber et al. correlated the Tafel slope of catalysts in the $Ni-Fe-Co-Ce-O_x$ composition space to the redox potential of the catalysts, likely a combination of the $Co^{2+/3+}$ and $Ni^{2+/3+}$ redox potentials.[48] However, the lower Tafel slopes found for catalysts with higher redox potentials may only be due to Fe incorporation which is known to both lower the Tafel slope and anodically shift the redox peak for both Ni and Co based catalysts.[14,15,28,43]

Figure 3.6 shows TOF_{tm} for each $Ni_{1-z}M_zO_xH_y$ catalyst versus the formal potential $E^{0'}$ of the Ni redox wave, where $E^{0'}$ is taken as the average of the anodic and cathodic peak potentials, E_{pa} and E_{pc}. There is no strong correlation between $E^{0'}$ and TOF, with the exception of Fe showing both increased $E^{0'}$ and TOF_{tm}. The data show that 10% Fe induces an 18 mV anodic shift of the formal potential along with two orders of magnitude increase in activity. At 30% total metal, cations such as Ce and Ti induce similar anodic peak shifts, 13 and 36 mV, respectively, but do not result in comparable increases in activity. This suggests that the electronics of the Ni cation, as reported by the formal potential of the Ni couple, are not affecting the OER activity. This result is consistent with Ni not being the active site in $Ni(Fe)O_xH_y$. We do note that the measured formal potentials can be influenced by kinetic and ion-transfer resistances in the film, which add some uncertainty to the above analysis.

The fact that the $Ni^{2+/3+}$ redox potential is not a good descriptor of catalytic activity suggests that Fe or Ce may be the OER active site in the doped films. Ce, like Fe, shows 3+/4+ redox activity. We find that increasing Fe content in $Ni_{1-z}Fe_zO_xH_y$ films from 10 to 30% results in increased activity, consistent with Fe acting as the active site

within the NiO_xH_y matrix. Increasing Ce content from 10 to 30% decreases activity. This is likely explained by a low solubility of Ce^{4+} in NiO_xH_y, due to the difference in cation size.
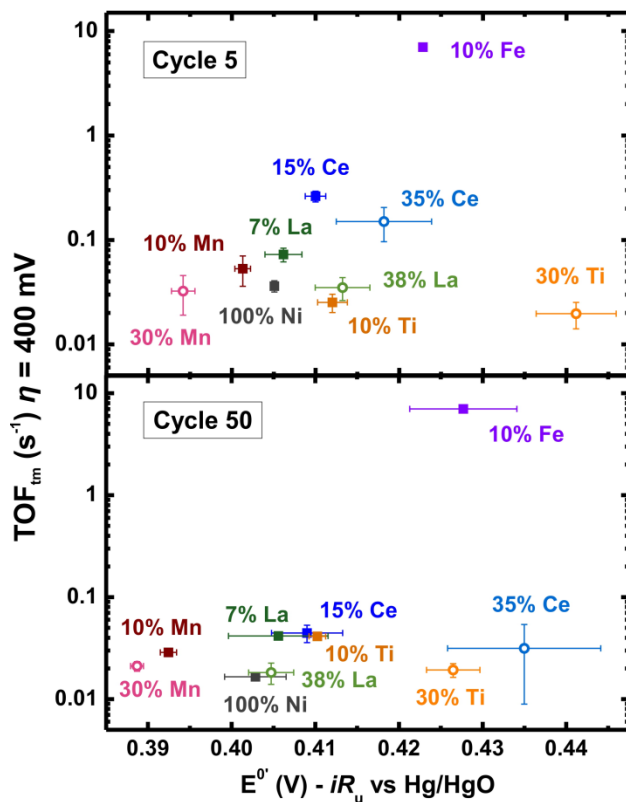
Figure 3.6. TOF_{tm} vs. $E^{0'}$ of $Ni^{2+/3+}$ for $Ni_{1-z}M_zO_xH_y$ after 5 (top) and 50 (bottom) cycles in 1 M Fe-free KOH at 20 mV s^{-1} at low concentrations (closed squares) and higher concentrations (open circles) of added cations. The formal potential, $E^{0'}$, is taken as the average of the cathodic and anodic peak potentials for the $Ni^{2+/3+}$ redox wave.

Comparison of Film Preparation Methods. In heterogeneous electrocatalysis, activity is often dependent on synthesis method due to changes in surface area or electrical connectivity.[13,23,56] We investigated if activity trends determined for spin-cast $Ni_{1-z}M_zO_xH_y$ films also hold for their electrodeposited counterparts of similar composition. The OER activity, electrochemical cycling behavior and morphology are similar for the electrodeposited and spin-cast films (Figures B.3 and B.15-17). The solution spin-casting method likely contributes to the similarities between spin-cast and electrodeposited films,

as discussed in Section 3.1. The low annealing temperature of the spin-cast films, 150°C, prevents formation of the oxide phases. The as-deposited films have more hydroxide character than spin-cast films annealed at higher temperatures above 300 ºC,[13] which is evident from the $Ni^{2+/3+}$ oxidation wave that remains largely unchanged throughout 50 cycles for most of the spin-cast films (Figure B.5). These low-temperature spin-cast hydroxide films are thus easier to convert to the (oxy)hydroxide phases that are the active phase present during the OER.[50,68–70] They also have the advantage over the electrodeposited films of precise composition and thickness control.

We note that for both preparation methods the degree of cation mixing is unknown due to the difficulty in obtaining local structural data in thin, disordered films from conventional x-ray diffraction. However, because these films are electrolyte-permeated at the molecular level, added cations should be electrochemically accessible. The short (10 min) low-temperature (150 ºC) processing makes complete phase segregation during synthesis unlikely. Additionally, the observed electronic changes to the NiO_xH_y films with added cation (i.e. changes in the $Ni^{2+/3+}$ redox wave) suggest interaction between cations on the molecular level. Further studies such as X-ray absorption measurements are needed to understand local structural differences which may affect catalytic activity.

Conclusion and Bridge

We studied $Ni_{1-z}M_zO_xH_y$ films, where M is Ti, Mn, Fe, La, or Ce, and found that only Fe increases the OER electrocatalytic activity. Although adding Ce induces a ten-fold OER activity increase for NiO_xH_y, the enhancement decays quickly. Ti, Mn, and La cations have almost no effect on NiO_xH_y catalytic activity. The results also inform the discussion of which cation(s) are the active site for the OER. We showed that there is no strong correlation between the formal potential of the $Ni^{2+/3+}$ redox couple and the electrocatalytic OER activity, suggesting that Ni site electronics are not of primary importance to the OER mechanism. This is consistent with Fe being the active site in $Ni(Fe)O_xH_y$. We also demonstrate that these conclusions are intrinsic to the $Ni_{1-z}M_zO_xH_y$ by comparing films fabricated with two different deposition methods, solution spin-casting and electrodeposition. In sum, our results illustrate the apparently unique effects

of Fe cations, and point to other $Ni_{1-z}M_zO_xH_y$ compositions as analogous systems for understanding the mechanisms behind those synergistic effects.

Given that Fe appears to be uniquely important in transition metal (oxy)hydroxide electrocatalysts for the OER, further studies of its properties are warranted. In the following Chapter further investigation of the intrinsic activity of FeO_xH_y will be performed to understand the exceptional activity of Fe and Fe-incorporated catalysts.

CHAPTER IV

ELECTRODE SUBSTRATE DEPENDENCE OF IRON (OXY)HYDROXIDE ELECTROCATALYTIC ACTIVITY FOR THE OXYGEN EVOLUTION REACTION

Chapter IV contains co-authored unpublished material. Prof. Boettcher and I conceived of the project. I performed experiments and analyzed data as well as directed experiments and analysis performed by undergraduate A. Vise. I wrote the paper with help from Prof. Boettcher and A. Vise along with editorial assistance from Boettcher and M. B. Stevens. It is prepared in the format of the Journal of the American Chemical Society.

Introduction

The oxygen evolution reaction (OER, in aqueous alkaline solution: $4OH^- \rightarrow O_2 + 2H_2O + 4e$) is a source of efficiency loss for several renewable energy technologies including water electrolysis and CO_2 reduction.[1–4] Significant effort has been made to understand and design electrocatalysts for this reaction. Iron (oxy)hydroxide (denoted as FeO_xH_y due to potential-dependent oxidation and protonation state) is one of the most intrinsically-active earth-abundant single-metal materials for catalyzing the OER in base, however, its activity is highly dependent on conductivity, electrode substrate, and structure.[5–11] Additionally, when Fe is embedded into NiOOH or CoOOH, the OER activity is even higher.[6,12,13] These effects are poorly understood and a better understanding would allow for more rational design within the field of OER electrocatalysis.

Understanding electrode substrate interactions with the OER catalyst is important for determining the intrinsic activity of a catalyst.[14] We have shown that the OER activity of FeO_xH_y at low overpotentials (350 mV) is nearly two orders of magnitude higher on Au substrates compared to Pt substrates.[5] Computational efforts by Bell et al. have shown that an Fe atom atop an Au_2O_3 matrix is more active than pure Au_2O_3,[15]

which is not surprising given the intrinsic activity of FeO_xH_y.[6] There has been no investigation in the literature so far of the unique relationship between FeO_xH_y and Au/Au_2O_3 compared to other noble metals and their oxides.

The enhancement of the OER activity of other transition metal (oxy)hydroxides (Mn, Co, Ni, NiFe) by Au and other noble metals (Pt, Ag, Cu, Pd) has been investigated previously.[16–25] For example, Bell et al. showed enhanced OER activity of Au-supported Ni and Co oxides, which they attributed to charge transfer from transition metal to the highly electronegativity Au substrate.[26,27] Additionally, they found that the activity of CoO_x correlated with the electronegativity of the metal substrate in the order Au > Pt > Pd > Cu > Co. Jaramillo and coworkers have shown that MnO_x embedded with noble metal nanoparticles (Au, Pt, Pd, Ag) is more active than MnO_x on glassy carbon due to an increase in the amount of Mn^{IV}, observed by X-ray absorption spectroscopy (XAS).[28,29] In this work, the activity of MnO_x with noble metal nanoparticles varied in the order Au ≈ Pd > Pt > Ag, in contrast with the electronegativity trend found by Bell.

Investigation of the effects of metal substrate on the OER activity of FeO_xH_y is necessary for several reasons. Firstly, it is possible that studies of other noble-metal enhancement of transition metal oxides are affected by Fe impurities, which have been shown to readily incorporate into Ni, Co, and Mn oxides/oxyhydroxides.[6,12,13,30] Secondly, the two orders of magnitude difference in OER activity between Au and Pt-supported FeO_xH_y is much higher than other transition metals, indicating a different enhancement mechanism may be in effect. Finally, since noble metals are often used as substrates for heterogeneous electrocatalysis, it is important to understand the effects of Fe impurities on these substrates in order to make accurate measurements of intrinsic activities of catalytic materials.

Here we use cyclic voltammetry (CV) and chronopotentiometry to assess the OER activity of FeO_xH_y on different substrates (Au, Pt, Pd, C, and Cu) in 1 M or 0.1 M KOH. CV was also used to examine the effects of electrolyte impurities on the activity of the substrates themselves. We show that the enhanced OER activity of FeO_xH_y on Au electrode substrates is unique, likely due to a greater adsorption strength that also leads to better charge transport at the Au-FeO_xH_y interface. Additionally, we show that the

presence of transition metal impurities in KOH electrolyte greatly increase the OER current of Au electrode substrates, making it a questionable substrate choice for fundamental studies of thin film OER catalysts.

Experimental

Electrode Fabrication. The electrodes had surface areas of ~ 0.1-1.0 cm^2 and were constructed by depositing 25 nm of Ti adhesion layer and 50 nm of Au, Cu, Pd, or Pt onto glass microscope slides. Au and Pd were deposited via thermal evaporation and Ti, Pt, and Cu by electron beam evaporation (Amod, Angstrom Engineering). The films were connected to Sn-Cu wire via Ag paint (Ted Pella). Epoxy (Loctite Hysol E-60HP or 9640) covered any exposed wire and Ag paint. The entire perimeter and back of slide was covered with hot glue to prevent leaching of Fe from glass or epoxy components.[31] The C electrode was purchased from CH Instruments (glassy carbon, 3 mm diameter). FeO_xH_y films were deposited onto the metal electrodes from aqueous solutions containing 0.1 M $FeCl_2$ (Alfa Aesar, 98%) and 0.05 M $NaNO_3$ (Mallinckrodt) for 20 seconds at -0.2 mA cm^{-2} according to previous procedures.[5]

Electrochemical Characterization. All electrodes and films were analyzed by CV at 20 mV s^{-1} and steady-state chronopotentiometry measurements (Tafel analysis) using a BioLogic potentiostat (SP300 or SP200) in a polymethylpentene 3-electrode cell with a Pt-wire counter electrode and Hg/HgO reference electrode (CH Instruments). Tafel analysis was completed from low to high current densities (first two steps held for 10 minutes and all consecutive steps were held for 3 minutes). Two CVs and an impendence measurement were taken before the first step and after the last step. Throughout electrochemical characterization, O_2 was bubbled and a magnetic stir bar was used to prevent bubbles from accumulating on the electrode surface. Electrochemical characterization was carried out in four types of 1 M KOH except for Cu electrodes which were analyzed in 0.1 M KOH due to lower Cu solubility at this electrolyte concentration. ACS Grade KOH was purchased from Alfa Aesar. Semiconductor-grade (SC) KOH electrolyte was purchased from Sigma Aldrich, (semiconductor grade 99.999% trace metal basis). Fe-free electrolyte was SCG KOH cleaned of Fe impurities using $Ni(OH)_2$ following our previously reported method.[13] Fe-spiked electrolyte was

achieved by adding 1 ppm of $Fe(NO_3)_3$ (Ricca, ICP-MS standard, 1000 ppm Fe) to SC grade KOH during the first CV cycle for each film. All data were corrected after collection for uncompensated series resistance based on impedance measurements taken before and after cycling. Uncompensated series resistance ranged from $3 - 15\ \Omega$ in 1 M KOH and $25 - 45\ \Omega$ in 0.1 M KOH. All potentials are given in overpotential, referenced to the thermodynamic potential for the OER, E_{OH^-/O_2} , taken as 1.23 V anodic of the hydrogen evolution reaction potential at a Pt electrode in H_2-saturated 1 M or 0.1 M KOH.

X-Ray Photoelectron Spectroscopy (XPS). XP spectra were collected on a Thermo EscaLab 250 using a monochramtic Al Kα X-ray with a 20 eV pass energy and 0.1 eV step size. Data on Cu samples were collected with a non-monochromatized Mg Kα source with a 40 eV pass energy and 0.2 eV, due to Cu Auger interference at the Fe 2p binding energy region. An electron flood gun was used during all measurements for charge neutralization. The binding energy scale for each sample was calibrated by setting the C-H peak in the C 1s spectra to 284.8 eV.

Results and Discussion

Electrolyte Impurities. It is known that electrolyte impurities can affect the catalytic ability of OER catalysts,[12,13,30] but relatively little attention has been given to impurity effects on the underlying electrode substrate.[15,32] We tested commonly used electrode substrates (Au, Pt, C, Pd, and Cu) in KOH electrolyte of different purity. We find that some substrates are more affected by electrolyte impurities than others, shown in Figure 4.1, where electrolyte impurities increase in the order Fe-free < SC < ACS. Cu appears to be the least affected by solution impurities, as it has the same OER current at 450 mV overpotential in all three electrolytes, Table 4.1, although this is likely due to the lower electrolyte concentration, 0.1 M rather than 1 M. Pd substrates are also little affected by solution impurities; the OER current at 450 mV overpotential for a Pd electrode is the same in both Fe-free and ACS grade and double in SC grade. The OER current of a Pt electrode roughly doubles each time as electrolyte purity decreases. The insets in each of the CVs in Figure 4.1 show that the capacitive regions on each of the substrates vary little

between the different electrolytes. Additionally, differences in electrochemically active surface areas are unlikely to contribute to the activity trends as they are similar (Figure C.1).

The C electrode is least affected by solution impurities and has the lowest OER current at 450 mV overpotential in all three types of electrolyte tested here. However, the lack of activity increase in metal ion-contaminated electrolyte likely implies weak adhesion/adsorption of metal oxide (MO_x) species to the glassy carbon surface. This poor adhesion has been demonstrated previously to affect charge transfer in catalysts intentionally deposited onto glassy carbon as an electrode substrate.[16,33,34] Au is the most affected by solution impurities, with its OER current increasing by roughly an order of magnitude as the electrolyte purity decreases. The onset of OER is as low as 325 mV in ACS grade and 400 mV in SC grade 1 M KOH. The order of magnitude increase in OER current density from Fe-free to SC grade suggests a strong interaction between Au and Fe, since only Fe impurities are removed in the cleaning process. The interaction between Au and Ni impurities, however, is surprisingly weak; OER current in Fe-free KOH is lower than all substrates, despite the presence of residual Ni impurities from the cleaning procedure.[13,31,32] The large increases in OER current density for an Au electrode as metal ion impurities increase indicates a greater MO_x adsorption strength and better charge transfer between Au and adsorbed MO_x species.
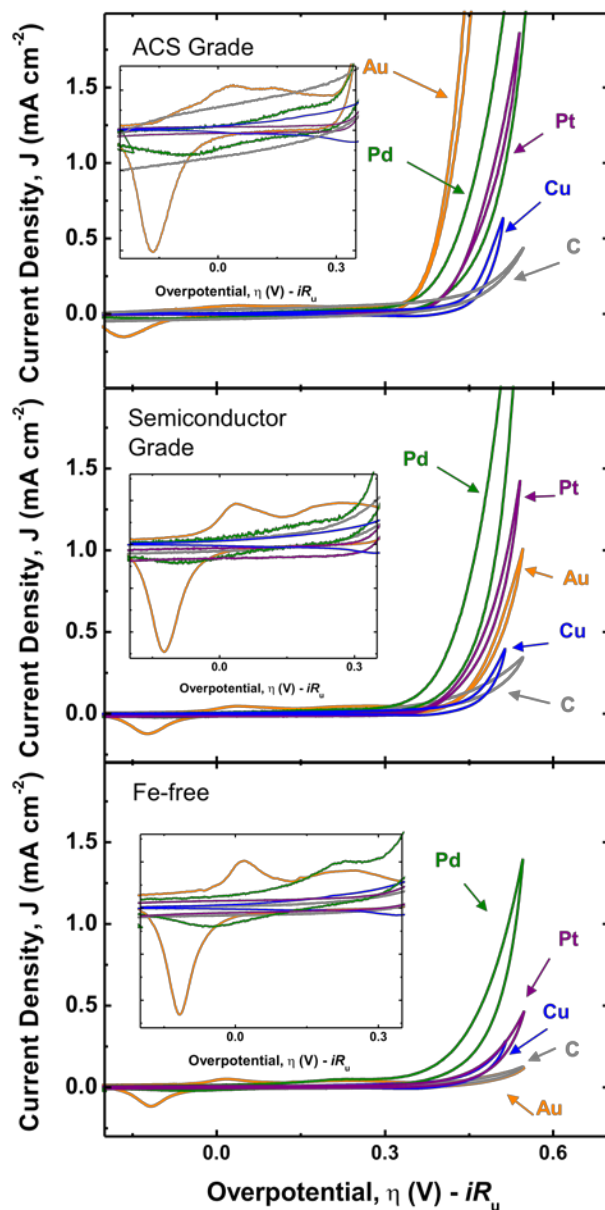
Figure 4.1. Cyclic voltammetry at 20 mV s^{-1} of electrode substrates in A) ACS grade, B) semiconductor grade, and C) Fe-free KOH. Cycle 5 of 50 is shown for each material which is representative of at least three replicates. All CVs were run in 1 M KOH except Cu in 0.1 M KOH.

57

Table 4.1. OER current density at 0.45 V vs E_{OH^-/O_2} for electrodes in KOH electrolyte of different purity.

Current Density at η = 450 mV					
	Type of 1 M KOH				
Electrode Substrate	Fe-free	Semiconductor grade (99.99%)	ACS Grade	1 ppm Fe	SCG FeO$_x$H$_y$ film
Au	0.040 (0.006)	0.20 (0.07)	1.8 (0.6)	33 (4)	8 (2)
C	0.032 (0.009)	0.042 (0.005)	0.11 (0.02)	0.5 (0.4)	0.24 (0.08)
Cu*	0.086 (0.002)	0.08 (0.02)	0.08 (0.03)	4 (1)	0.6 (0.2)
Pd	0.34 (0.02)	0.72 (0.07)	0.3 (0.1)	2.9 (0.3)	2.0 (0.8)
Pt	0.09 (0.01)	0.20 (0.09)	0.41 (0.02)	0.8 (0.1)	4.5 (2)

Substrate Dependence of FeO$_x$H$_y$ OER Activity. Due to the chemical instability of FeO$_x$H$_y$ at high pH and anodic potentials, determining the intrinsic OER activity on different substrates is inherently difficult.[5] Here, we test the substrate dependence of the OER activity of FeO$_x$H$_y$ in two different ways: 1) by adding 1 ppm of Fe(NO$_3$)$_3$ to the electrolyte solution to effectively deposit a monolayer of FeO$_x$H$_y$ on the electrode surface and 2) by intentionally depositing a thin film ($\sim$ 1 μg cm^{-2}) of FeO$_x$H$_y$ on the electrode surface. In general, we find the same trends for both Fe-deposition methods indicating we are measuring the intrinsic activity of FeO$_x$H$_y$ on each substrate.

In both Fe-deposition methods we find that the OER activity of FeO$_x$H$_y$ on a given substrate increases in the order C < Cu $\approx$ Pt $\approx$ Pd < Au, shown in Figure 4.2. The OER current density at 450 mV overpotential of each deposition method is greater than the bare electrodes in ACS grade KOH, indicating that we are indeed measuring FeO$_x$H$_y$ on the substrates and not the bare substrates themselves. FeO$_x$H$_y$ on Au has a low onset potential for the OER, $\sim$ 300 mV by $\sim$ 100 mV. Figure 4.2 shows the OER activity of FeO$_x$H$_y$ on glassy carbon substrates in lower than all the other substrates tested here. The overpotential at 1 mA cm^{-2} of FeO$_x$H$_y$ on C is 100 mV higher than on Pt, Pd, or Cu

and more than 200 mV higher than on Au. This discrepancy has likely made fundamental studies of FeO$_x$H$_y$ challenging and is further compounded in high-loading studies where low conductivity of FeOOH limits charge transport.[5]
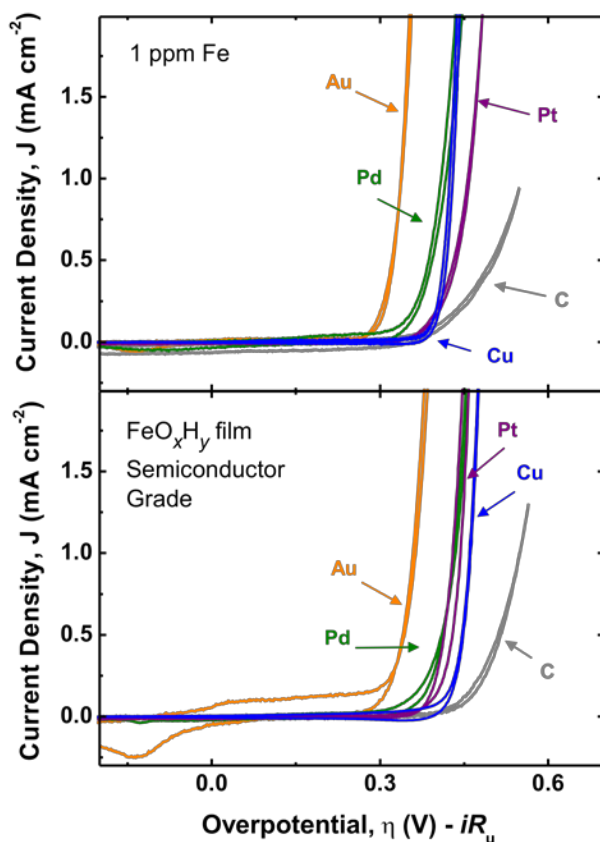
Figure 4.2. Cyclic voltammetry at 20 mV s^{-1} for FeO$_x$H$_y$ on different substrates deposited from (top) 1 ppm Fe(NO$_3$)$_3$ in KOH and (bottom) 0.1 M FeCl$_2$ in 0.5 M NaNO$_3$. Cycle 5 of 50 is shown for each and is representative of at least three replicates. All CVs were run in 1 M SC grade KOH except Cu in 0.1 M SC grade KOH.

The presence of Fe on the surface for the measurement is also further confirmed by contrasting the Tafel slopes of FeO$_x$H$_y$ from both deposition methods to that of the bare electrodes in Fe-free KOH, Figure 4.3. The Tafel slopes, shown in Figure 4.3, are similar for the two deposition methods, although there is some variability. The Tafel slopes found in 1 M KOH with 1 ppm Fe are likely to be closer to the true value, as there was a constant amount of Fe present in solution and the error bars at each point are smaller in Figure 4.3. The higher variability in Tafel measurements for the cathodically-

deposited FeO_xH_y may indicate that these films do not adhere as well to the substrate as FeO_xH_y adsorbed from solution.

The Tafel slopes of FeO_xH_y on Cu and Au substrates are similar, ~ 45 mV dec^{-1} (regardless of Fe-deposition method) indicating the OER mechanism and rate-determining step may be the same. FeO_xH_y on Pt and Pd also have similar Tafel slopes, ~ 60 mV dec^{-1} indicating similar OER mechanisms on both these substrates. Doyle and Lyons have also found Tafel slopes of 45 and 60 mV dec^{-1} for FeOxHy grown on metallic Fe electrodes in NaOH under different solution and cycling conditions.[11] This suggests that Tafel slopes found here for FeO_xH_y on different substrates is due to differences in the FeO_xH_y atomic structure on those substrates. The Tafel analysis on C substrates has high variability in both FeO_xH_y deposition methods, but low variability (smaller error bars) in the Fe-free Tafel measurements, likely due to poor adhesion of MO_x species to the glassy carbon surface. The accurate determination of the Tafel slope for FeO_xH_y on glassy carbon is therefore difficult and the results here should be taken with caution.
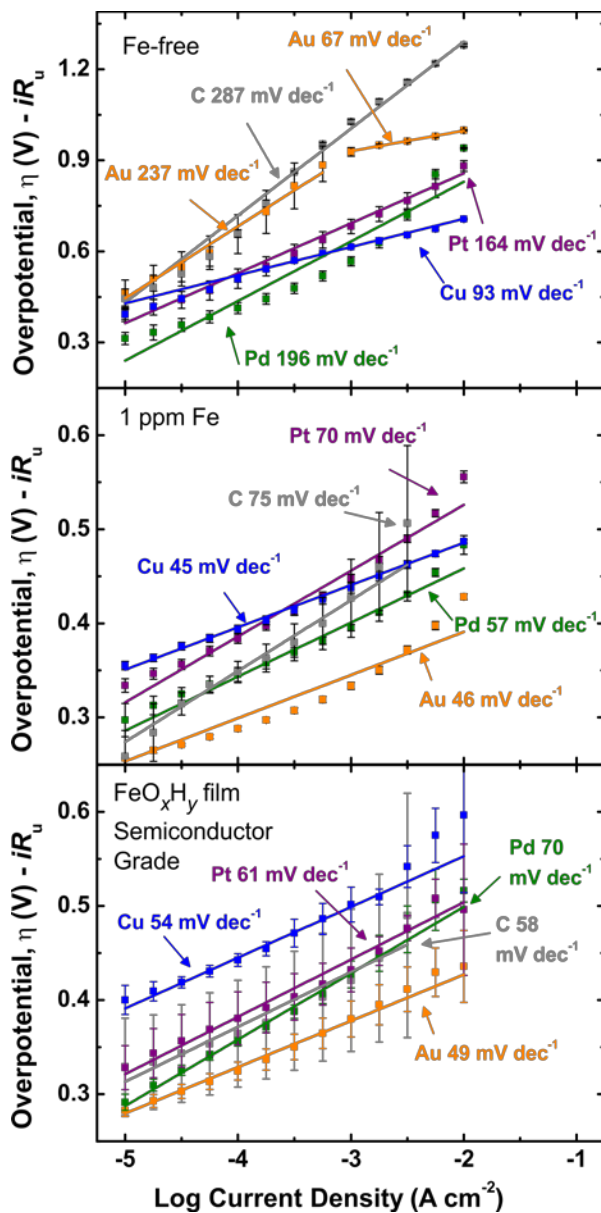
Figure 4.3. Tafel analysis of different electrode substrates in (top) Fe-free KOH, (middle) KOH with 1 ppm Fe, and (bottom) in semiconductor grade KOH with FeOxHy films deposited on the electrode surface.

Au Enhancement of FeOxHy Activity. It is clear from the data presented here that the enhancement of the OER activity of FeO_xH_y from Au is both large and unique. This is consistent with other reports of Au enhancing the OER activity of NiO_x,[13,21,24,26] MnO_x,[28,29,35] and CoO_x[17,20,24,25,27,36] catalysts, indicating a strong interaction between Au and first-row transition metal oxides/(oxy)hydroxides. The cause of the enhancement from Au is suggested to be the increased oxidation state of the transition metal (Mn, Fe,

61

Co, Ni) due to the electron-withdrawing ability of Au. Indeed, Au has a high electronegativity, but comparison with other highly-electronegative elements shows no correlation between substrate electronegativity and OER current of FeO_xH_y catalyst (Figure C.2). This suggests there is an additional factor contributing to the OER activity enhancement from Au.

The electron-withdrawing ability of the substrate is dependent on the electronegativity of the substrate, but also the ability to transfer charge at the interface between substrate and catalyst. Studies comparing NiO_xH_y and $Ni(Fe)O_xH_y$ on GC and Au substrates have shown that $Ni^{2+/3+}$ oxidation is more complete on Au than GC substrates,[16,33] indicating better charge transfer at the interface. The improved charge transfer at the Au-transition metal oxide interface is likely due to an increased strength of adsorption or adhesion of the oxide to the Au surface. This increased adhesion strength is confirmed by XPS analysis after performing electrochemistry in KOH with 1 ppm Fe, shown in Figure 4.4. Despite that fact that electrochemical analysis indicates OER activity from FeO_x species, after removing the electrodes from solution and rinsing with H_2O, Fe is only present on Au and Cu substrates, not Pt or Pd (Figure 4.4). This is evidence of strong adhesion of FeO_xH_y to the Au surface, and the Cu surface as well. The lower current density from Cu substrates despite strong FeO_xH_y adhesion can be attributed to the lower efficiency of the OER in 0.1 M KOH compared to 1 M KOH.
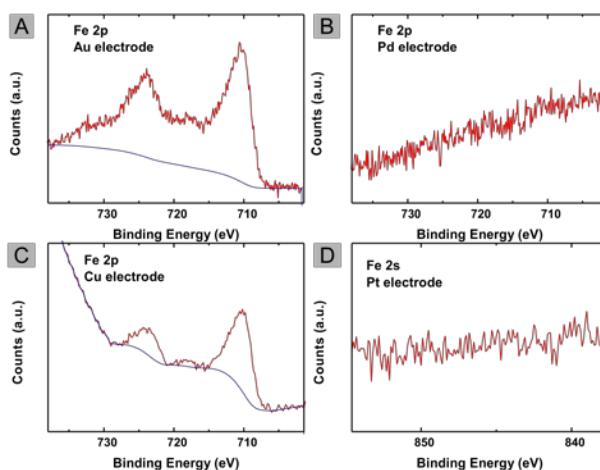
Figure 4.4. Fe XP spectra on A) Au, B) Pd, C) Cu, and D) Pt electrodes after cycling in KOH spike with 1 ppm Fe. Au, Pt, and Pd electrode spectra were collected with an Al

Kα source and Cu with Mg Kα due to Cu Auger peak at Fe 2p binding energy. The Fe 2s region is shown for Pt electrode due to overlap with Fe 2p and Pt 3s.

Interestingly, we also find that of the metallic substrates, the Au surface is the only one to undergo completely reversible oxidation in solution. Redox features can be seen for all substrates except for C (Figures 4.1, 4.2, and C.3), and XPS analysis after electrochemistry shows evidence of substrate oxidation for Cu, Pd, and Pt, Figure 4.5. The Au surface, while it clearly undergoes oxidation and reduction, evident from the redox features in Figures 4.1 and 4.2, returns to a completely metallic state with no evidence of residual oxide.
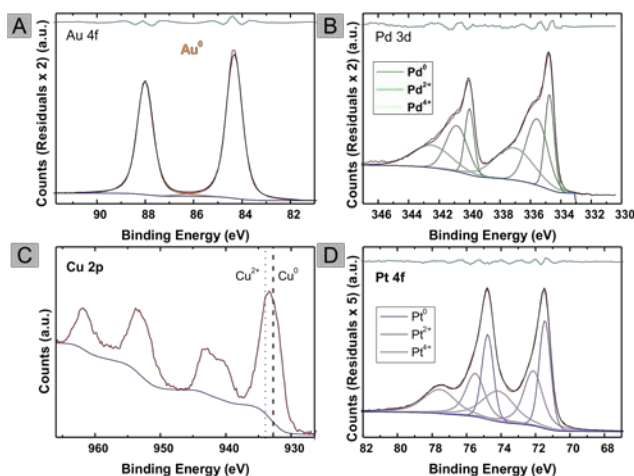
Figure 4.5. Metal electrode XP spectra for A) Au, B) Pd, C) Cu, and D) Pt substrates. Au, Pd, and Pt were collected with Al Kα and Cu with Mg Kα sources.

Conclusion and Bridge

The OER activity of FeO_xH_y has been shown here to vary based on electrode substrate material in the order Au > Pd ≈ Cu ≈ Pt > C. The differences in activity are likely due to differences in the strength of adhesion of FeO_xH_y to the electrode substrate. The variation in adsorption strength lead to differences in charge transport at the FeO_xH_y-electrode interface, contributing to the observed activity trend. The electrode substrate material also likely affects the atomic structure of FeO_xH_y and is responsible for differences in activity. Further investigation into differences in the atomic and electronic structure of FeO_xH_y on different electrode substrates in operando would necessary to confirm this hypothesis.

The sensitivity of the OER activity of FeOxHy on different substrates and in different matrices (eg. NiOOH explored in Chapter III) suggests it is important for the active site in OER catalysis. To further investigate the role of Fe in the active site for OER catalysis, in operando experiments on CoFeO$_x$H$_y$ are performed and analyzed in the next chapter, Chapter V.

CHAPTER V

OPERANDO X-RAY ABSORPTION SPECTROSCOPY SHOWS FE OXIDATION IS CONCURRENT WITH OXYGEN EVOLUTION IN COBALT-IRON (OXY)HYDROXIDE ELECTROCATALYSTS

This chapter contains co-authored unpublished material. M. Stevens, Prof. Boettcher, and I conceived of the project. I performed experiments along with M. Stevens and M. Nellist with technical assistance from S. Fakra. M C. Toroker and M Dahan performed calculations. I analyzed data and wrote most of the paper with computational sections written by M. Toroker. Editorial assistance was provided by M. Stevens and S. Boettcher. It is prepared for submission to the peer-reviewed journal Angewandte Chemie International Edition.

Introduction

The efficiency of the oxygen evolution reaction (OER), particularly in alkaline solution, limits several prospective renewable energy-conversion technologies.[1–3] In order to improve the efficiency, a better understanding of catalysts for this reaction is necessary. In alkaline conditions, Fe-incorporated Ni- and Co-based (oxy)hydroxides (Ni(Fe)O_xH$_y$, Co(Fe)O_xH$_y$) are some of the best catalysts for the OER, but still operate at higher overpotentials than their HER catalyst counterparts.[4,5] Understanding the mechanism for activity enhancement upon Fe incorporation would lead to the rational design of better catalysts.

Operando XAS has been used previously to probe atomic and electronic structure of catalysts during the OER.[6–12] Friebel et al.[6] determined that in Ni(Fe)O_xH$_y$ the Fe – O bond length during the OER was similar to that of NiOOH, which is shorter than in FeOOH. Using this structural information, they performed DFT calculations to show that catalysis on Fe – O sites has a lower theoretical overpotential than on Ni – O sites, indicating that Fe was likely the active site. Despite the Fe – O bond shortening, they claim no oxidation of Fe to Fe^{4+}. Conversely, Chen et al.[13] find evidence of Fe^{4+} in

Ni(Fe)O_xH$_y$ during the OER using Mössbauer spectroscopy. Hunter et al.[14] have shown evidence of Fe^{6+} during OER catalysis in non-aqueous electrolytes.

Co(Fe)O_xH$_y$ is structurally and electrochemically similar to Ni(Fe)O_xH$_y$.[15,16] Both are comprised of layers of edge-sharing MO(H)$_6$ octahedra and show increased OER activity and a more-positive (nominal) $M^{2+/3+}$ reduction potential upon Fe-incorporation. Smith et al.[9] examined amorphous photochemically-deposited $Fe_{100-y}Co_yO_x$ films using operando electrochemical XAS and observed oxidation of Co, but not Fe during the OER. Gong et al.[11] found that CoO_x with Fe^{3+} ions adsorbed from solution was more active than co-deposited $Fe_{4.4}Co_{95.6}O_x$. Operando XAS suggests oxidation of Co during the OER to a similar extent for both samples. Fe oxidation was not found in either sample, but adsorbed Fe^{3+} exhibited a lower oxygen coordination and was concluded to be responsible for the sample's higher activity. Under-coordinated Fe-sites or edge-sites have also been hypothesized to be the active site in Ni(Fe)O_xH$_y$[13,17–19] and CoOOH.[20,21]

Here we use operando XAS to study Co(Fe)O_xH$_y$. We find clear evidence for Fe oxidation and Fe – O bond shortening at OER relevant potentials, consistent with the hypothesis that Fe is the active site[22]

Experimental

Electrochemical Cell Fabrication. Si$_3$N$_4$ windows (2 x 2 mm, 1 μm thick) embedded in Si (5 x 5 mm, 200 μm thick) were purchased from Norcada. The windows were then treated with an O$_2$/N$_2$ plasma for 10 min to promote adhesion. Ti (30 nm) and Au (25 nm) were then deposited sequentially on the windows via evaporation with an electron-beam and thermal source, respectively (Amod, Angstrom Engineering). Electrical connection to the Au surface was made using Sn-Cu wire (McMaster-Carr) and Ag paint (Ted Pella). The windowed-electrode was then embedded in a 60-mL polypropylene using hot glue. All metal components except the Au surface were covered in hot glue to prevent contact with solution. A new cell was fabricated for each sample tested.

Catalyst Film Deposition. Films were deposited from 0.1 M transition metal aqueous solutions (18.2 M·cm H$_2$O). Co(NO$_3$)$_2$ (Alfa Aesar, 98%) and FeCl$_2$ (Alfa Aesar, 98%)

were used as the Co and Fe sources respectively. All Co and Fe compositions in the text are referenced to the deposition solution ratios as characterization of the deposited films was not possible. Previous deposition under similar conditions shows that the Fe content in lower in the films than in the deposition solution by ~ 5%.[15] N_2 was bubbled through the solution for 20 min before addition of $FeCl_2$. Using a carbon cloth counter electrode, -1 mA cm^{-2} was applied to the working electrode for 30 s to precipitate a Co or Co-Fe hydroxide film on the electrode surface. The use of electro-chemical precipitation leads to highly porous films where nearly every Co/Fe cation is exposed to the electrolyte[15]; these films are easily completely transformed into the active oxyhydroxide phase under OER conditions making them superior samples for study compared to oxide phases where only the surface is electrochemically active.[4,23–25] The deposition solution was immediately emptied from the cell to prevent dissolution of the deposited film and rinsed with water. Films were cycled in 1 M KOH (10 mV s^{-1}) to confirm film deposition from -0.3 to 0.4 V vs E_{OH^-/O_2}. Electrochemical cells with deposited films were then shipped to the Advanced Light Source (ALS) for combined electrochemical-XAS experiments.

Electrochemical Characterization. Electrochemical analysis was performed using a Biologic SP-200 potentiostat in 1 M KOH (Sigma Aldrich, 99.99% trace metals) with an Hg/HgO reference electrode and Pt counter electrode. Co-cleaned KOH was used for CoO_xH_y films.[15] Chronoamperometry measurements were performed at potentials negative of the $Co^{2+/3+}$ reduction wave, positive of the oxidation wave, and during OER, for the duration of the XAS measurements. Cyclic voltammetry at 10 mV s^{-1} was performed before and after XAS measurements on each sample. All potentials in Appendix D and in Chapter V are reference in overpotential, vs E_{OH^-/O_2}.

XAS Measurements. XAS was performed at beamline 10.3.2 (bending magnet) at the ALS with a ring current of 500 mA. A Si(111) monochromator was used to monochromatize the incident beam, I_0. The energy axis was aligned using a glitch in I_0 near the main edge which was calibrated on Co (7708.78 eV edge) and Fe (7110.75 eV edge) foils measured in transmission mode using an ionization chamber. The $CoFeO_xH_y$ samples were oriented at a 45° angle from the incident beam and fluorescence signal from the films was detected using a 7-element UltraLEGe detector (Canberra) at a 90°

angle from the incident beam. XAS data was collected under ambient conditions in the electrochemical cell while a constant potential was applied to the working electrode.

XAS Data Analysis. All absorption spectra, $\mu(E)$, were deglitched and corrected for detector dead time using the LABVIEW software at beamline 10.3.2. Further data reduction and fourier transformed extended X-ray absorption fine structure (FT-EXAFS) fitting was performed using IFEFFIT-based Athena and Artemis software programs.[26] For each measurement, between 5 and 10 scans were merged to obtain the final spectrum. All spectra were edge step normalized using pre and post-edge backgrounds. The edge energy, E_0, was set to 1.0 and determined by the energy of the highest peak in the first derivative of $\mu(E)$. FT-EXAFS spectra were fit using Artemis software. Theoretical scattering paths were calculated using FEFF6[27,28] for $CoOOH$[29] (ICSD #56288). Fits were performed over an R space range of 0.9 – 2.0 Å in the Fourier transform using k ranges of 2.0 to 11.0 Å^{-1} (Fe) or 2.0 – 11.5 Å^{-1} (Co) with a Kaiser-Bessel window.

Results and Discussion

Cyclic voltammetry of the $CoFeO_xH_y$ films in Figure 5.1 shows that the addition of Fe improves the OER activity of CoO_xH_y and shifts the nominal $Co^{2+/3+}$ reduction potential anodic, consistent with previous work.[15] In this way, the $Co(Fe)O_xH_y$ system is similar to that of $Ni(Fe)O_xH_y$. An important difference, however, is that the nominal 2+/3+ reduction potential is well-separated from the onset of OER current in the $Co(Fe)$ system while in the $Ni(Fe)$ system the OER onset current occurs at a potential near the 2+/3+ oxidation wave for high Fe content. Thus for the $Co(Fe)$ system we can compare XAS spectra for Co and Fe in a potential range prior to the OER, but where the sample is already in the oxidized "active" oxyhydroxide state, with spectra where the catalyst remains in the active oxyhydroxide state but is now at potentials sufficient to drive the OER (see dotted lines in Figure 5.1). This comparison is complicated in the $Ni(Fe)$ system where the oxidation of Ni is often coincident with the onset of OER current.[30]
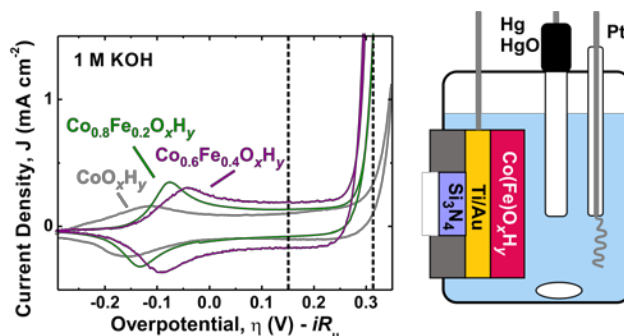
Figure 5.1. A) Cyclic voltammetry data on $Co(Fe)O_xH_y$ films collected at 10 mV s^{-1} immediately prior to XAS data collection. Vertical dashed lines represent potentials at which chronoamperometry was performed while collecting operando XAS measurements. B) Schematic of electrochemical cell used for operando electrochemical-XAS data collection. Incident X-rays and outgoing fluorescence from the catalyst went travelled through the 1 μm Si₃N₄ window and the Ti (30 nm)/Au (25 nm) layers.

For Fe-free CoO_xH_y, the Co K-edge energy at an overpotential of 0.1 V vs. E_{OH^-/O_2} (anodic of the Co oxidation wave but cathodic of the OER current onset) indicates that Co is mostly present as Co^{3+} (Figure D.1A). This is consistent with conversion from the hydroxide to oxyhydroxide phase during the $Co^{2+/3+}$ oxidation wave. Comparison of the X-ray absorption near edge spectroscopy (XANES) data collected at a potential negative of the reduction wave (-0.3 V) to $Co(OH)_2$ and CoOOH show that only a small fraction of the Co can be reduced back to Co^{2+} and that the oxyhydroxide structure dominates rather than the hydroxide (Figure D.1C), consistent with previous reports.[15] Based on the higher K-edge energy shown in Figure 5.2A, a small amount of oxidation occurs (0.5 eV increase in edge energy) when the catalyst potential is stepped from an overpotential of 0.1 V to 0.4 V where OER occurs. There is no change in the pre-edge feature. This oxidation likely represents a fraction of Co being oxidized from Co^{3+} to Co^{4+} (Figure D.1A), consistent with other reports that show presence of Co^{4+} during the OER.[23,31,32] It is possible that these oxidized Co sites represent those performing the OER, perhaps at reactive edge sites.[17,18,21]

Upon Fe addition, Co oxidation during the OER is suppressed, evidenced by the lack of change in the Co K-edge energy when stepping the potential to OER conditions (Figure 5.2B and 5.2C). There is thus little to no Co^{4+} present in mixed $Co(Fe)O_xH_y$ films during the OER. This is further confirmed by the slightly higher (0.3 eV) Co K-edge energy of

CoO_xH_y during the OER compared to $Co(Fe)O_xH_y$ (Figure D.1B). However, the pre-edge feature shown in the inset of Figures 5.2B and 5.2C does increase intensity during OER, suggesting a distortion of the CoO_6 octahedra that increases the transition probability. This distortion is likely caused by changes to the Fe – O environment during the OER, which will be discussed below.
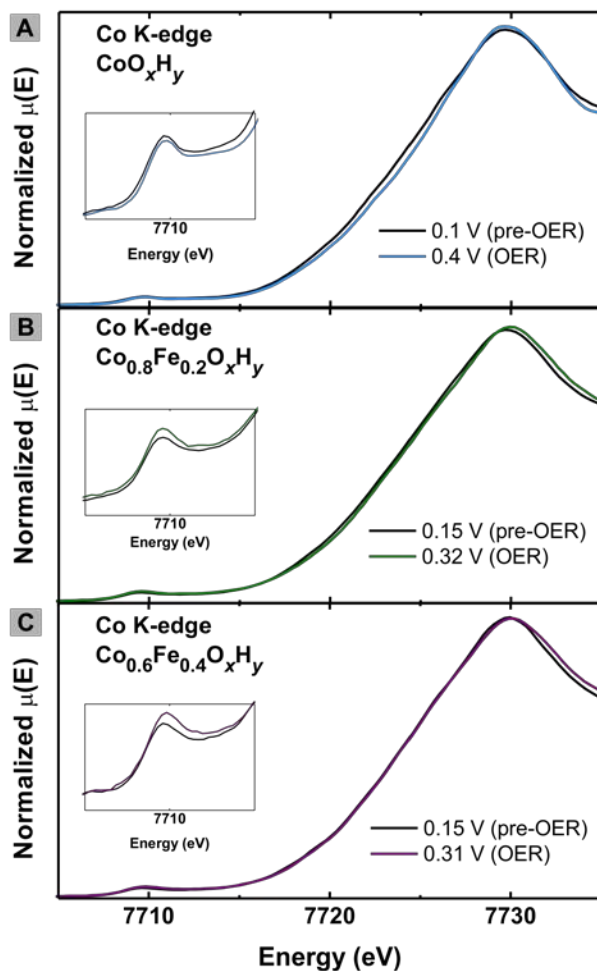
Figure 5.2. Operando Co K-edge XANES data collected under applied electrochemical potential for A) CoO_xH_y, B) $Co_{0.8}Fe_{0.2}O_xH_y$, and C) $Co_{0.6}Fe_{0.4}O_xH_y$ films. Pre-OER spectra were collected at potentials higher than the nominal $Co^{2+/3+}$ oxidation wave and prior to OER onset. OER spectra were collected at potentials necessary to maintain 3 – 4 mA cm^{-2} of OER current density.

Fe K-edge spectra on $Co(Fe)O_xH_y$ films collected at an overpotential of 0.15 V (anodic of the nominal $Co^{2+/3+}$ oxidation wave, but prior to the onset of OER) show that Fe is nominally Fe^{3+} in the films. This edge position is higher than at -0.3 V vs. E_{OH^-/O_2}

70

(cathodic of the $Co^{2+/3+}$ reduction peak) the indicating that Fe is also oxidized in the $Co^{2/3+}$ redox wave (Figure D.2A-B). In the OER region, Fe^{3+} is further oxidized (Figures 5.3A and 5.3B); the Fe K-edge energy shifts positive by 0.7 eV relative to at 0.15 V vs. ε_{O_2/OH^-} (prior to the OER onset) and is also similarly higher in energy than the α-Fe_2O_3 and γ-FeOOH standards (Figure D.2C). This increase in Fe edge energy upon driving OER represents oxidation of only a fraction of the Fe^{3+} sites. XAS spectra from $La_{1-x}Sr_xFeO_{3-\delta}$ show that a change in Fe oxidation state from Fe^{3+} to Fe^{4+} results in an increase in K-edge energy of ~ 1.3 eV. The increase in Fe K-edge energy could also be the result of oxidation of Fe sites to Fe^{6+}, which has recently been suggested to be the active site in $Ni(Fe)O_xH_y$,[14] however Fe^{6+} sites would be highly reactive and are unlikely to be present in substantially high concentrations. Balasubramanian et al.[33] have reported Fe oxidation in anodically polarized NiOOH similar to that found here. The smaller than expected Fe K-edge shift was attributed to the higher degree of covalency in the Fe(IV) – O bond resulting in charge transfer back to Fe.[34] The fact that incomplete oxidation of Fe^{3+} is observed may be because only a fraction of Fe (perhaps at reactive edge/defect sites) are participating in catalysis.[11,17,18]
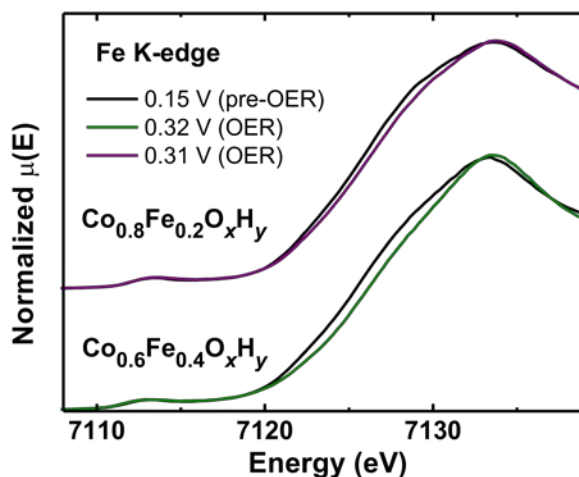
Figure 5.3. Operando Fe K-edge XANES data collected under applied electrochemical potential for A) CoO_xH_y, B) $Co_{0.8}Fe_{0.2}O_xH_y$, and C) $Co_{0.6}Fe_{0.4}O_xH_y$ films. Post-oxidation spectra were collected at potentials higher than the nominal $Co^{2+/3+}$ oxidation wave and prior to OER onset. OER spectra were collected at potentials necessary to maintain 3 – 4 mA cm^{-2} of OER current density.
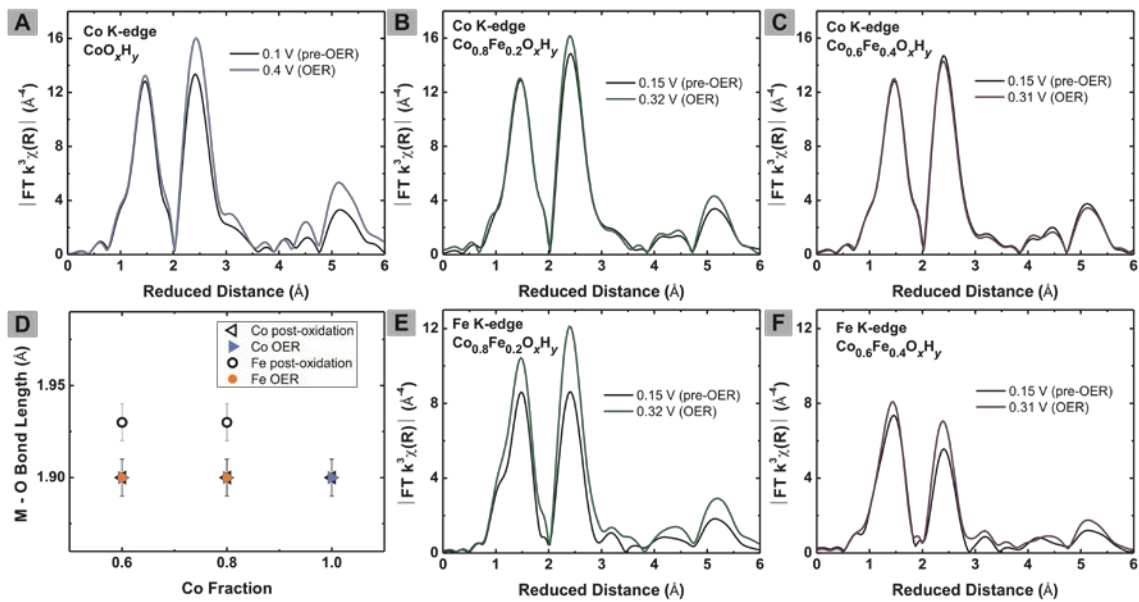
Figure 5.4. FT-EXAFS data for Co(Fe)O$_x$H$_y$ films at pre-OER and OER potentials in 1 M KOH. D) Metal – oxygen bond lengths for Co(Fe)O$_x$H$_y$ films before (pre-OER) and during the OER determined from FT-EXAFS fitting analysis.

We fit the Fourier transformed extended X-ray absorption fine structure (FT-EXAFS) (Figure 5.4) data to evaluate the metal-oxygen bond lengths (Figure 5.4D). We find no change in Co – O bond length when stepping the potential from 0.1 – 0.15 V vs E_{O_2/OH^-} to the OER regime at 0.3 – 0.4 V vs E_{O_2/OH^-}. At both potentials the Co – O bond length is 1.90 Å, with or without Fe present. This is as expected for Co(Fe)O$_x$H$_y$ films since there is no change in the Co oxidation state. For Fe-free CoO$_x$H$_y$, there is no apparent change in the Co – O bond length change despite the oxidation of Co observed by the positive shift in the Co K-edge. This is likely because the fraction of Co changing oxidation state is small. Conversely, the Fe – O bond length changes during the OER, shortening from 1.93 Å at 0.15 V vs ε_{O_2/OH^-} (prior to OER but more anodic than the Co oxidation wave) to 1.90 Å during the OER. This average Fe – O bond length is shorter than in Fe phases such as α-Fe$_2$O$_3$ (2.03 Å)[35] and γ-FeOOH (2.04 Å)[36], indicating that Fe is dispersed in the CoOOH matrix. While all Fe – O bonds are shortened during the OER, only a fraction of the Fe sites undergo oxidation, likely the reactive sites.[18]

The observed bond distance and oxidation state changes at the proposed active Fe sites were also studied with first principles calculations. We used Density Functional Theory +U (DFT+U) implemented in the VASP simulation package[37–39] to calculate the free energies required for the OER mechanism[40] shown in Figure 5.5 (see Appendix D for details). For Fe-doped CoOOH, the Fe-O average bond when the surface is adsorbed with water (*OH$_2$ intermediate) is ~1.95 Å and reduces to ~1.90 – 1.94 Å when OER proceeds through *OH and *O intermediates. This correlates to an increase in the calculated Fe oxidation state from +3 to nominally +4/+5. In contrast, the Co-O bond lengths in Fe-doped CoOOH both near and far from the active site do not change for the different OER intermediates maintaining an average value of ~1.91 Å. In the case of pure CoOOH, the Co-O bond lengths vary between 1.9 and 1.92 Å for the different intermediates as the Co oxidation state changes from +3 for the *OH$_2$ intermediate to nominally +4 for the *OH and *O intermediates. While there are certainly substantial differences between the simple structures and reaction mechanisms used for the DFT+U calculations and experiment, the central result that the Fe bond length and oxidation change for the different OER intermediates appears consistent.
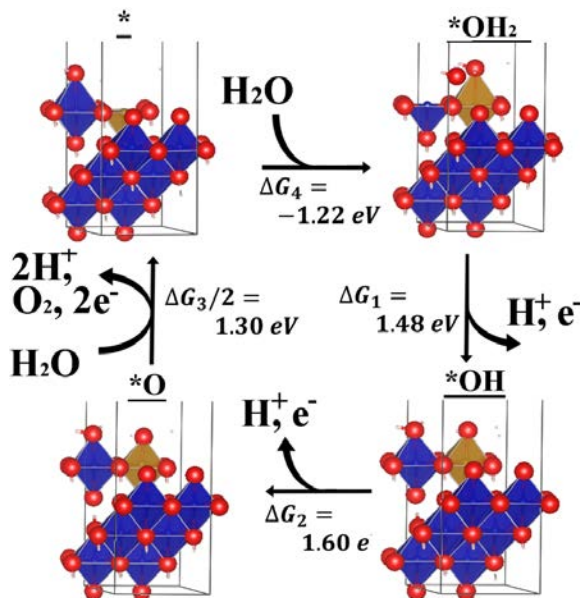
Figure 5.5. Schematic OER mechanism for Fe-doped CoOOH. The values for the free energies of reaction intermediates are indicated. Red, blue, brown, and white spheres represent O, Co, Fe, and H atoms. Created with VESTA visualization software.[41]

The experimental findings of this work also agree well with theory. The higher activity of $Co(Fe)O_xH_y$ compared to CoO_xH_y films has been demonstrated by considering the mechanisms proposed by Selloni and Norskov. In both cases, lower overpotential was demonstrated on Fe-doped CoOOH compared to pure CoOOH. Additionally, calculations also predicted a shortening of the Fe – O bond length during the OER, consistent with our experimental observations. Our results are also consistent with the experimental and theoretical study by Friebel et al. on NiFeOxHy, which is likely relevant due to the structural and electronic similarities to CoFeOxHy. Their DFT analysis showed lower overpotential on Fe-sites embedded in a NiOOH matrix, where the Fe – O bond lengths were the same as those for Ni – O.[6]

Most other studies have not reported an increase in Fe oxidation state along with potential-dependent shortening of the Fe – O bond in $Co(Fe)O_xH_y$, or $Ni(Fe)O_xH_y$, OER catalysts in alkaline solution. This could in part be due to differences in catalyst preparation. The Fe sites in catalyst films here are well-integrated into the CoOOH structure, evidenced by the similarity of the M – O and M – M shell distances in the FT-EXAFS (Figure 5.4). Since CoOOH is electronically conductive at all potentials, unlike FeOOH, the Fe sites in $Co(Fe)O_xH_y$ could be expected to undergo potential-dependent structural changes. The samples used for previous studies on $Co(Fe)O_xH_y$ may include oxide phases or separated Fe-phases that reduce the amount of electrochemically accessible $Co(Fe)O_xH_y$, making the changes seen here difficult to detect.[9,11,24,25] Interestingly, our potential-dependent Fe – O bond lengths are similar to those of Fe^{3+} ions adsorbed on CoO_xH_y, reported by Gong et al., which showed a decrease of the Fe – O bond length from 2.01 to 1.94 Å when changing the potential from open-circuit to OER conditions.[11] However in that case no concurrent oxidation of Fe was observed and bond length changes due to Co or Fe oxidation during the $Co^{2+/3+}$ oxidation wave rather than OER were not separated. Calvillo et al. has reported surface Fe oxidation on $Co_xFe_{3-x}O_4$ spinels at OER potentials after extended cycling.[25] Balasubramanian et al. reported Fe oxidation and Fe – O bond shortening ex situ in anodically polarized $Ni(Fe)O_xH_y$ films.[33]

74

Conclusion

      These data taken together support the hypothesis that Fe – O species are the active site in $Co(Fe)O_xH_y$ films. The films contain Fe^{3+} at all potentials prior to the onset of OER. Upon driving $Co(Fe)O_xH_y$ into the OER regime, Fe^{3+} is further oxidized while Co^{3+} observed at potentials just cathodic of the OER is not. In Fe-free CoO_xH_y Co^{3+} is oxidized during OER; indicating a fundamentally different mechanism compared to the $Co(Fe)O_xH_y$. Structurally, there are no differences in Co – O environment upon Fe addition, but large changes in activity, making it further unlikely that Co is the active site in the more-active $CoFeO_xH_y$. Finally, the small amount of oxidation observed for both Co in CoOxHy and Fe in Co(Fe)OxHy indicates that only a fraction of these sites undergo oxidation, suggesting that some sites are more reactive than others.

APPENDIX A

CHAPTER II SUPPORTING INFORMATION
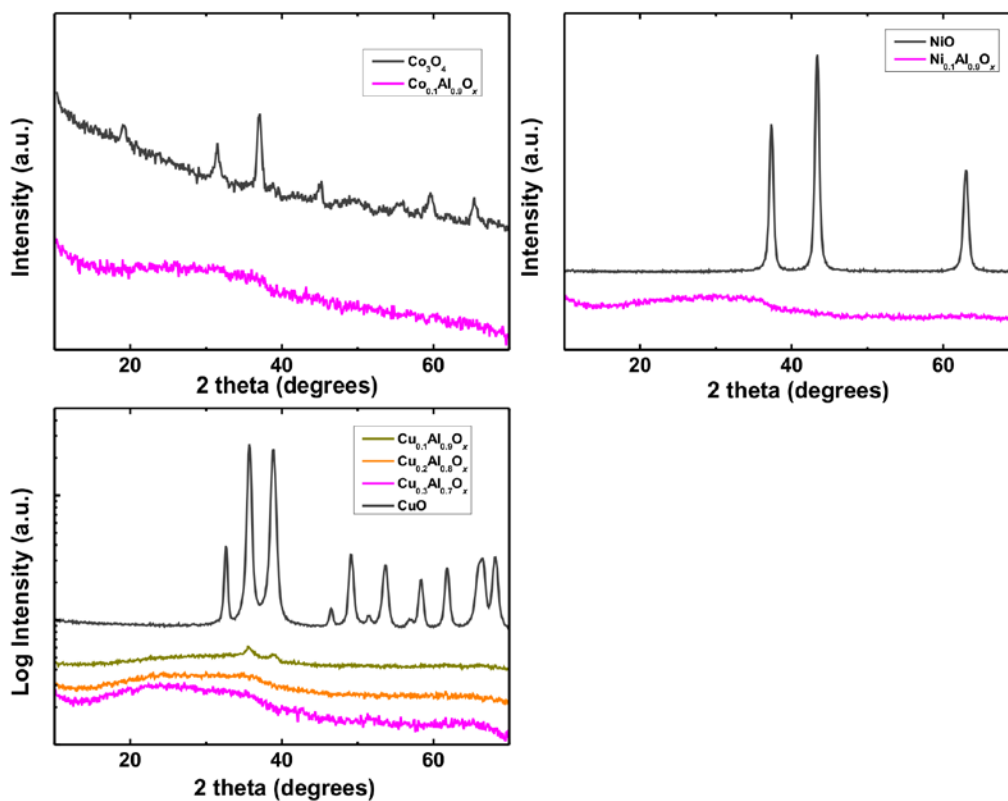
Figure A.1. GIXRD patterns for $M_yAl_{1-y}O_x$ films where M is not d^0, d^5, or d^{10}. Diffraction patterns were collected on the highest M-containing amorphous composition and on the Al-free MO_x films to ensure crystallinity.
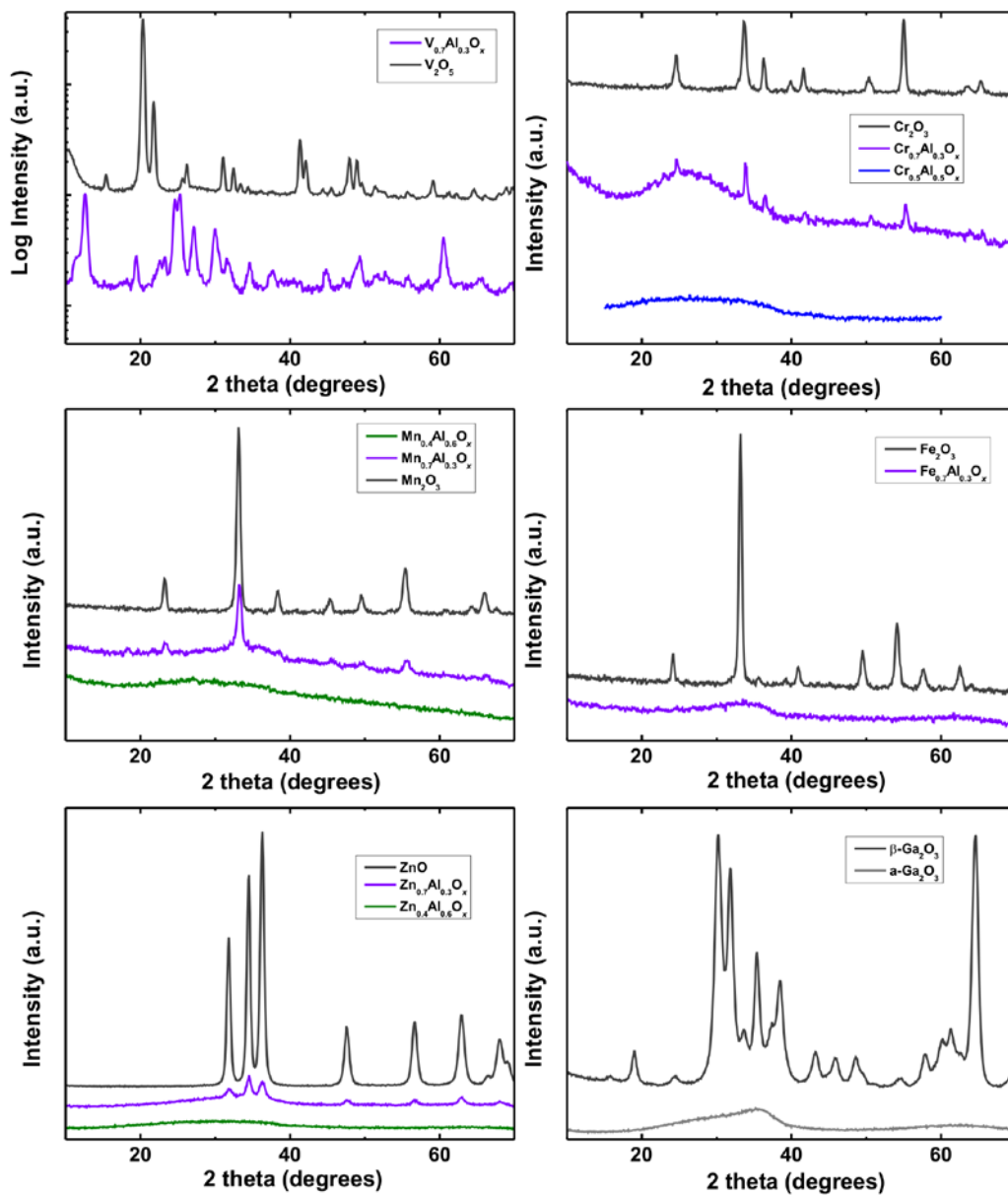
Figure A.2. GIXRD patterns from $M_yAl_{1-y}O_x$ films where M is d^0, d^5, or d^{10}. The highest M-containing amorphous composition and lowest M-containing crystalline composition studied are shown.
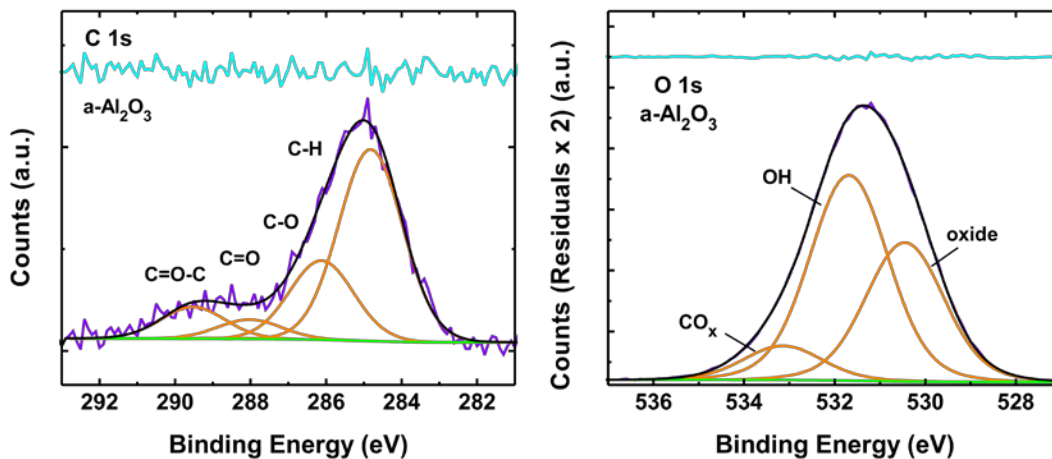
Figure A.3. C 1s and O 1s XP spectra of a-Al$_2$O$_3$ film with fits. The binding energy was calibrated by setting the C-H peak to 284.8 eV.
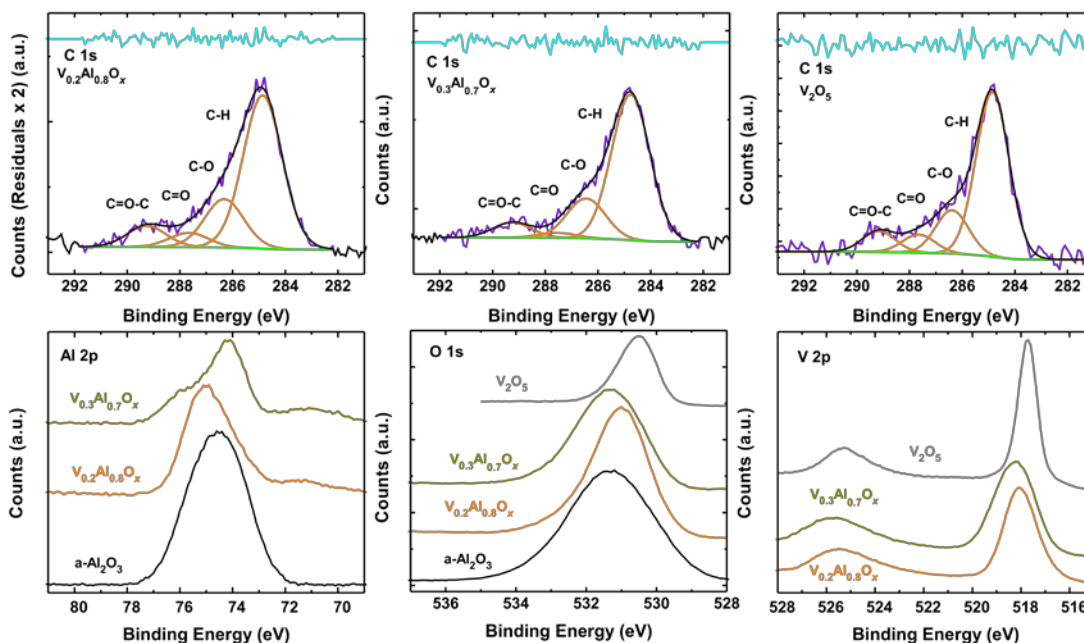
Figure A.4. XP spectra of V$_y$Al$_{1-y}$O$_x$ films C 1s (top), Al 2p, O 1s, and V 2p (bottom). The binding energy was calibrated by setting the C-H peak of each film to 284.8 eV. The V 3s peak (located at 66 eV for metallic V) can be seen on the low binding energy side of the Al 2p peak for films containing V.[1] The binding energy of the V 2p$_{3/2}$ peak is indicative of V^{5+} species.[2] The broadness of the V 2p peaks for films containing Al likely indicate the lack of uniform V coordination environment.
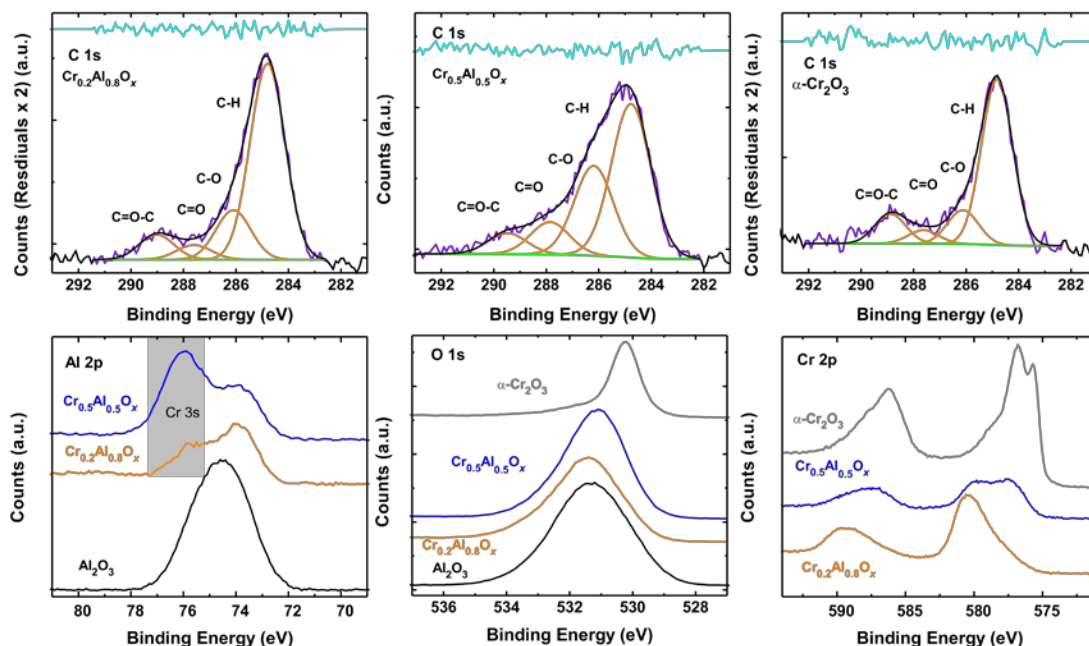
Figure A.5. XP spectra of $Cr_yAl_{1-y}O_x$ films C 1s (top), Al 2p, O 1s, and Cr 2p (bottom). The binding energy was calibrated by setting the C-H peak of each film to 284.8 eV. The Cr 3s peak (located at 75 eV for Cr^0) can be seen on the high binding energy side of the Al 2p peak for films containing Cr. The Cr 2p spectra for films containing Al indicate the presence of both Cr^{3+} and Cr^{6+} species.[3] The Cr 2p spectrum for α-Cr_2O_3 agrees well with previous reports.[4]
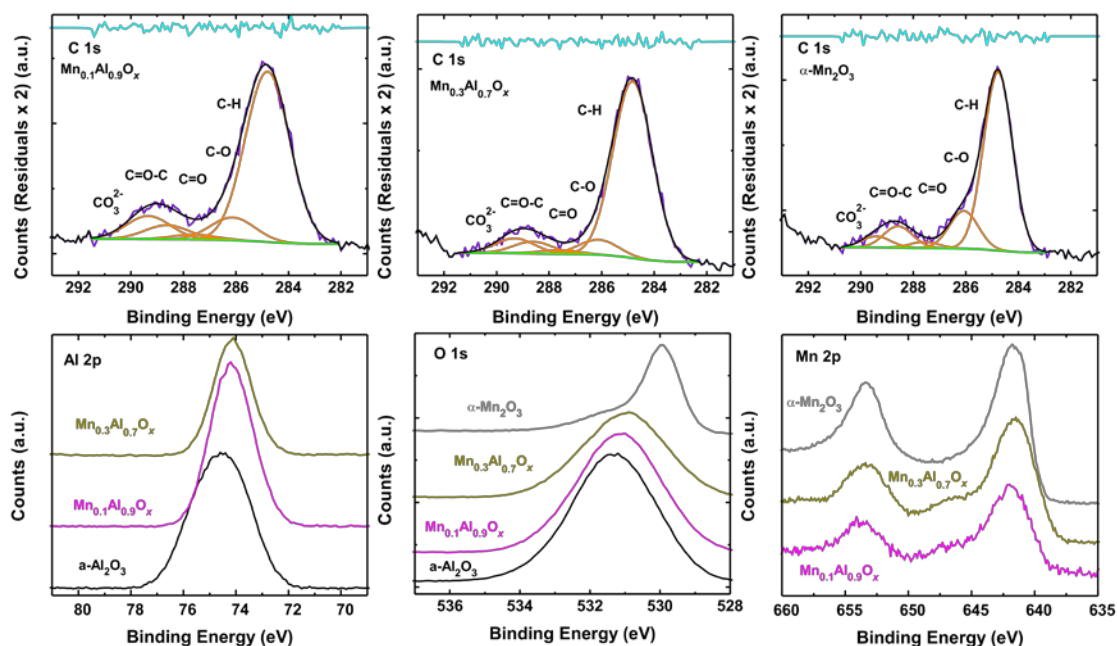
Figure A.6. XP spectra of $Mn_yAl_{1-y}O_x$ films C 1s (top), Al 2p, O 1s, and Mn 2p (bottom). The binding energy was calibrated by setting the C-H peak of each film to

79

284.8 eV. The presence of shake-up features in the Mn 2p spectra of films containing Al indicate the presence of Mn^{2+} in addition to Mn^{3+}.[5]
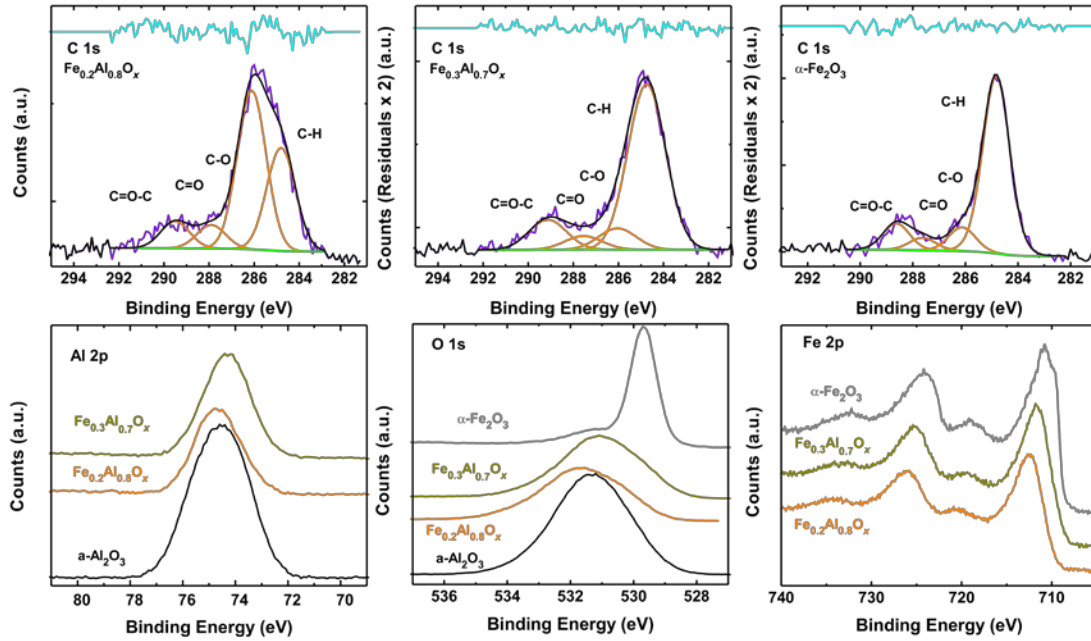
Figure A.7. XP spectra of $Fe_yAl_{1-y}O_x$ films C 1s (top), Al 2p, O 1s, and Fe 2p (bottom). The binding energy was calibrated by setting the C-H peak of each film to 284.8 eV. The difference in energy between the main 2p peaks and their shake-up features is indicative of Fe^{3+} rather than Fe^{2+}.[6]
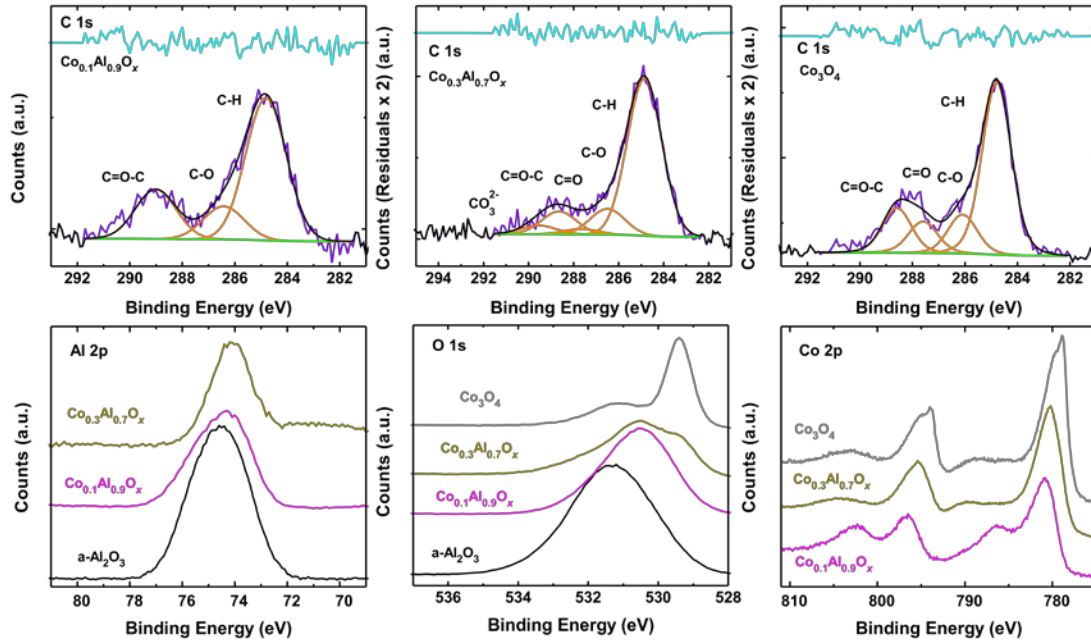
Figure A.8. XP spectra of $Co_yAl_{1-y}O_x$ films C 1s (top), Al 2p, O 1s, and Co 2p (bottom). The binding energy was calibrated by setting the C-H peak of each film to 284.8 eV. The position of the shake-up features in the Co 2p spectrum of the $Co_{0.1}Al_{0.9}O_x$ film indicates Co is present as Co^{2+}. Co 2p spectra for films with Co content greater than $y = 0.1$ are indicative of Co_3O_4.[5]
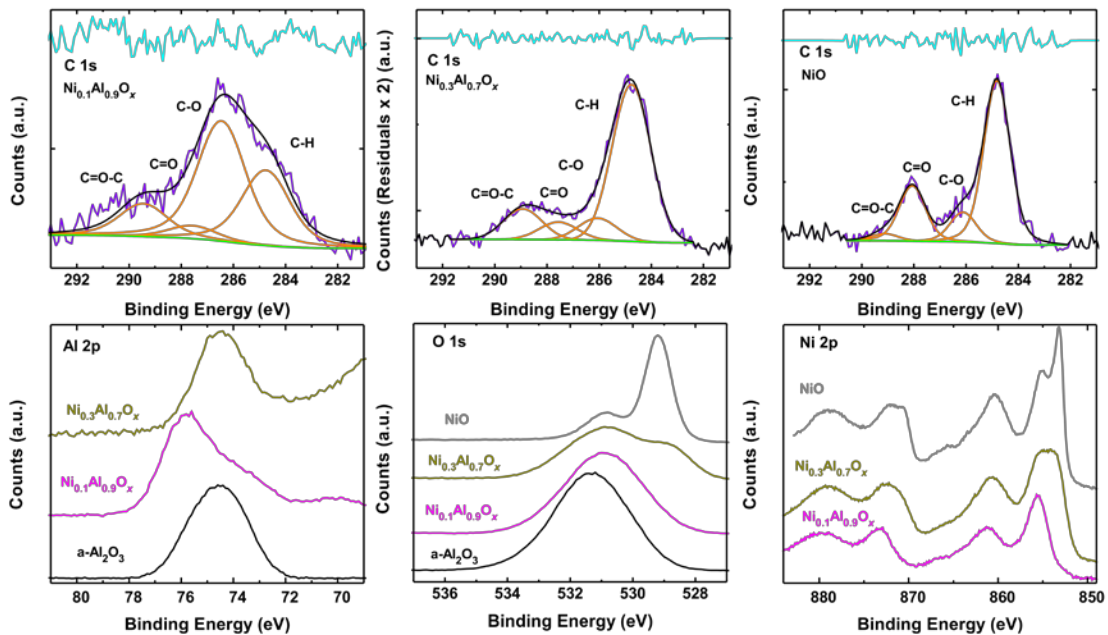
Figure A.9. XP spectra of $Ni_yAl_{1-y}O_x$ films C 1s (top), Al 2p, O 1s, and Ni 2p (bottom). The binding energy was calibrated by setting the C-H peak of each film to 284.8 eV. Ni 3p peaks (located at 67 eV for Ni^0) can be seen on the low binding energy side of the Al

81

2p peak for films containing both Ni and Al.[1] The binding energy of the Ni $2p_{3/2}$ peak further confirms that Ni is present as Ni^{2+}.[7]
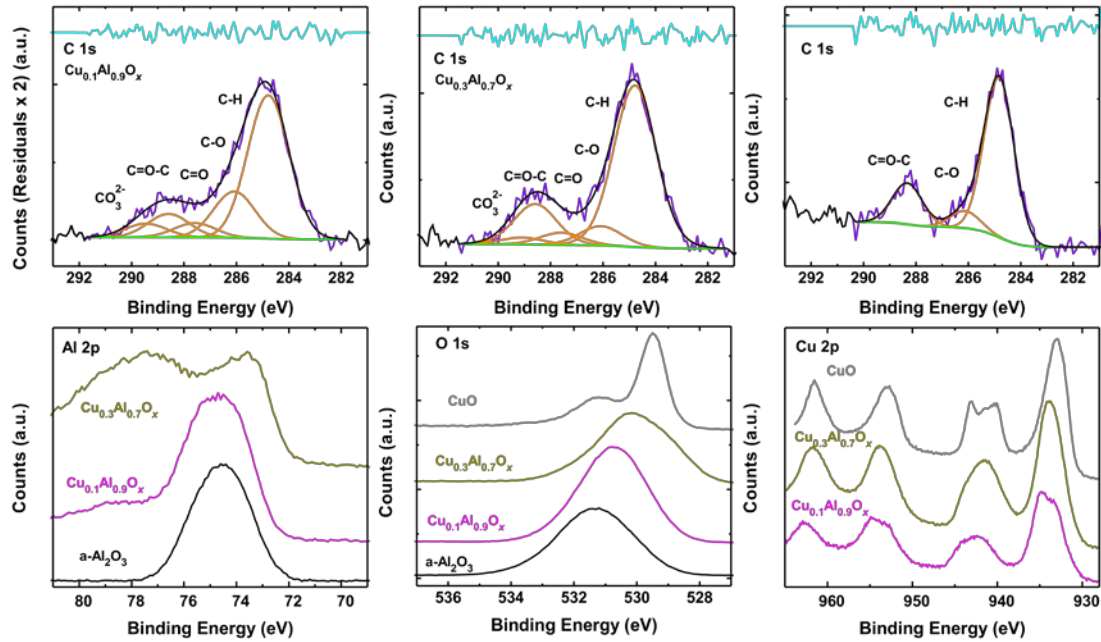
Figure A.10. XP spectra of $Cu_yAl_{1-y}O_x$ films C 1s (top), Al 2p, O 1s, and Cu 2p (bottom). The binding energy was calibrated by setting the C-H peak of each film to 284.8 eV. Cu 3p peaks (located at 77 and 75 eV for Cu^0) can be seen on the high binding energy side of the Al 2p peak for films containing both Cu and Al. The presence of shake-up features in the Cu 2p XP spectra indicate the presence of Cu^{2+}.[2]
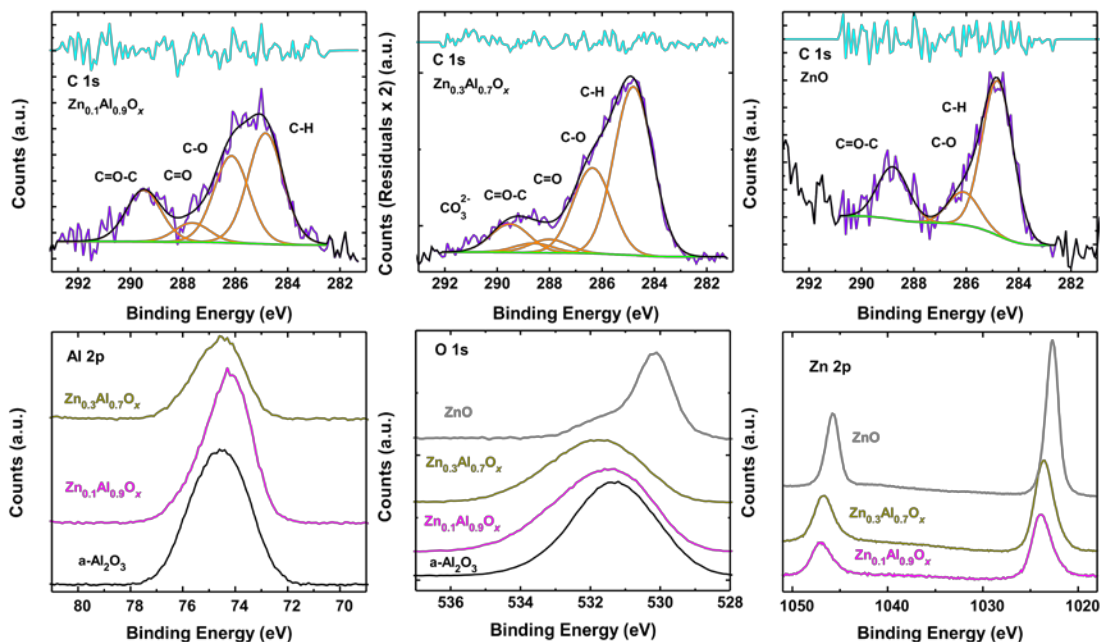
Figure A.11. XP spectra of $Zn_yAl_{1-y}O_x$ films C 1s (top), Al 2p, O 1s, and Zn 2p (bottom) XP spectra of $Zn_yAl_{1-y}O_x$ films. The binding energy was calibrated by setting the C-H peak of each film to 284.8 eV.
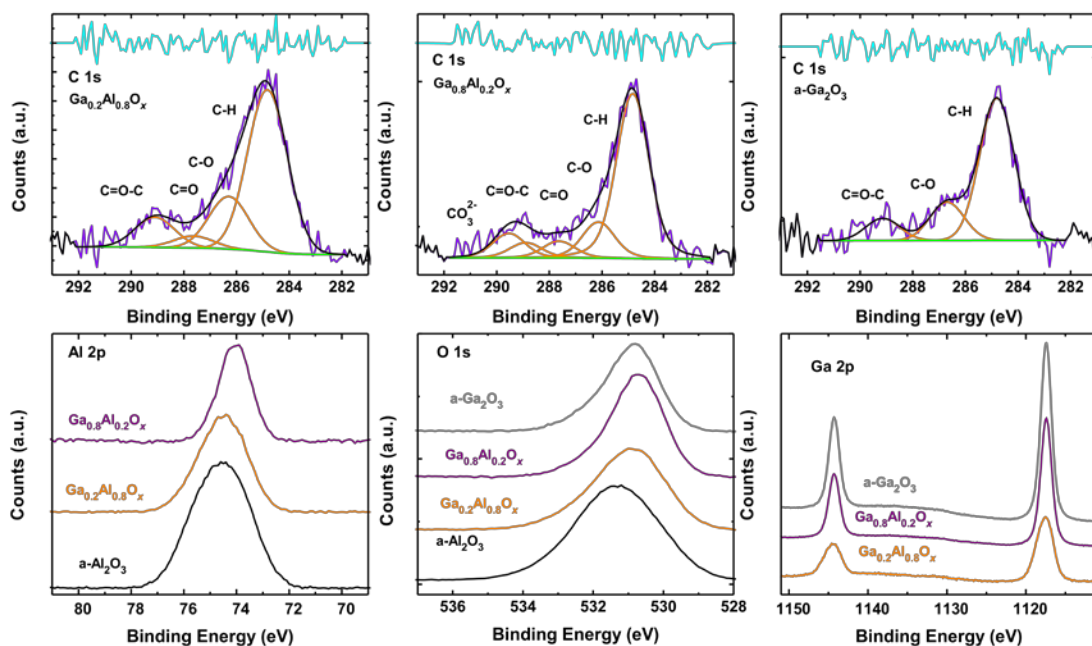
Figure A.12. XP spectra of $Ga_yAl_{1-y}O_x$ films C 1s (top), Al 2p, O 1s, and Ga 2p (bottom). The binding energy was calibrated by setting the C-H peak of each film to 284.8 eV. The binding energy of the Ga $2p_{3/2}$ peaks indicate that Ga is present as Ga^{3+}.[1]

83
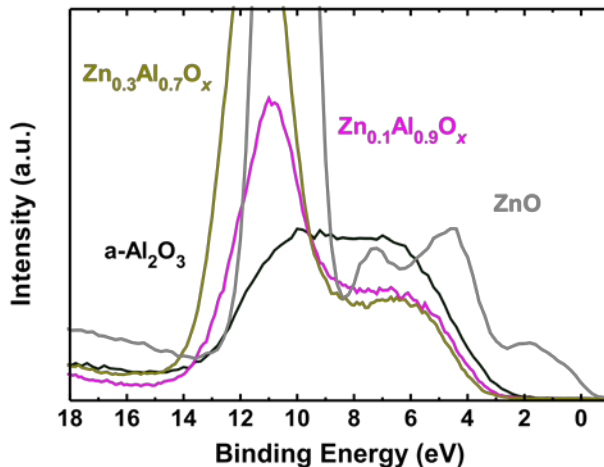
Figure A.13. VB-XPS of $Zn_yAl_{1-y}O_x$ films. Due to the crystalline nature of the ZnO film, the Ir substrate was not completely covered. Contributions from Ir to the valence band can be seen in the spectrum for ZnO on the low binding energy side.

XANES Analysis

Table A.1. Metal K-edge energy evaluated at the first peak in the first derivative of normalized $\mu(E)$ spectrum (after pre-edge feature).

Sample	E_0 (eV)	Sample	E_0 (eV)	Sample	E_0 (eV)
V foil	5465	Fe foil	7712	Cu foil	8979
V_2O_5	5481.1	Fe_2O_3	7123.4	CuO	8983.5
$V_{0.7}Al_{0.3}O_x$	5483.3	$Fe_{0.7}Al_{0.3}O_x$	7123	$Cu_{0.7}Al_{0.3}O_x$	8983.7
$V_{0.5}Al_{0.5}O_x$	5483.1	$Fe_{0.3}Al_{0.7}O_x$	7122.8	$Cu_{0.5}Al_{0.5}O_x$	8983.8
$V_{0.3}Al_{0.7}O_x$	5483.6	$Fe_{0.2}Al_{0.8}O_x$	7122.6	$Cu_{0.3}Al_{0.7}O_x$	8984.1
$V_{0.2}Al_{0.8}O_x$	5483.3	$Fe_{0.1}Al_{0.9}O_x$	7122.7	$Cu_{0.2}Al_{0.8}O_x$	8984.4
$V_{0.1}Al_{0.9}O_x$	5483.5	Co foil	7709	$Cu_{0.1}Al_{0.9}O_x$	8984.6
Cr foil	5989	Co_3O_4	7717.3	Zn foil	9659
Cr_2O_3	5999.6	$Co_{0.3}Al_{0.7}O_x$	7717.1	ZnO	9661.5
$Cr_{0.5}Al_{0.5}O_x$	6005.8	$Co_{0.2}Al_{0.8}O_x$	7717	$Zn_{0.7}Al_{0.3}O_x$	9662.2
$Cr_{0.3}Al_{0.7}O_x$	6006.3	$Co_{0.1}Al_{0.9}O_x$	7716.4	$Zn_{0.4}Al_{0.6}O_x$	9662.3
$Cr_{0.2}Al_{0.8}O_x$	6006.4	Ni foil	8333	$Zn_{0.3}Al_{0.7}O_x$	9662.3
$Cr_{0.1}Al_{0.9}O_x$	6006.4	NiO	8341	$Zn_{0.2}Al_{0.8}O_x$	9662.4
Mn foil	6539	$Ni_{0.3}Al_{0.7}O_x$	8341.1	$Zn_{0.1}Al_{0.9}O_x$	9662.4
Mn_2O_3	6548.1	$Ni_{0.2}Al_{0.8}O_x$	8341	Ta foil	9881
$Mn_{0.7}Al_{0.3}O_x$	6548.1	$Ni_{0.1}Al_{0.9}O_x$	8341.5	Ga_2O_3	10375.5
$Mn_{0.4}Al_{0.6}O_x$	6548.2			$Ga_{0.5}Al_{0.5}O_x$	10375.5
$Mn_{0.3}Al_{0.7}O_x$	6547.9			$Ga_{0.3}Al_{0.7}O_x$	10375.6
$Mn_{0.2}Al_{0.8}O_x$	6548			$Ga_{0.2}Al_{0.8}O_x$	10375.7
$Mn_{0.1}Al_{0.9}O_x$	6547.6				

84
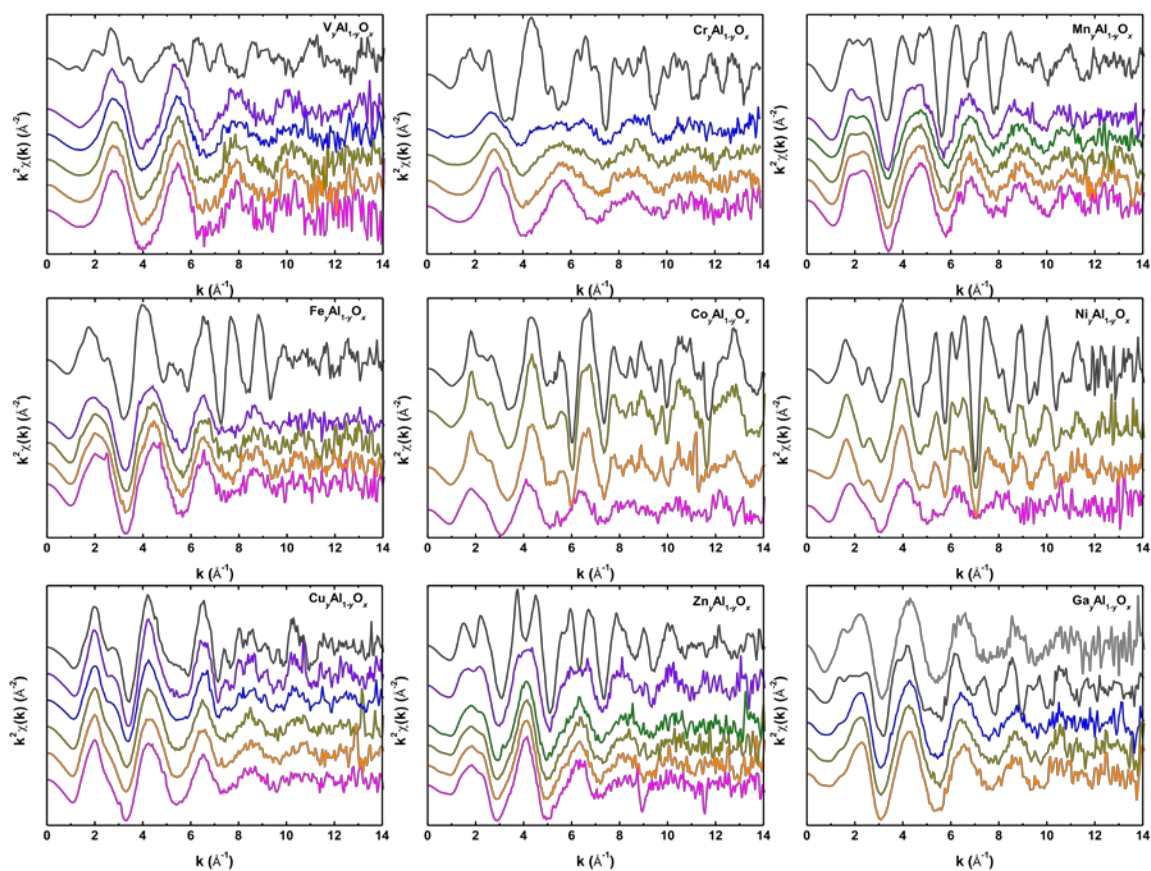
Figure A.14. k^2-weighted $\chi(k)$ data $M_yAl_{1-y}O_x$ films. Colors correspond to amounts of M as follows: $y = 0.1$ (magenta), 0.2 (orange), 0.3 (dark yellow), 0.4 (green), 0.5 (blue), 0.7 (violet), 1.0 crystalline (dark grey), and 1.0 amorphous (light grey).

EXAFS Fitting

All EXAFS data were fit using the Artemis software.[8] The EXAFS equation can generally be described by the sum of all scattering paths, i, according to

$$\chi(k) = \sum_i \frac{S_0^2 N_i f_i(k)}{k R_i^2} e^{-\frac{2R_i}{\lambda(k)}} e^{-2k^2 \sigma_i^2} \sin(2kR_i + \delta_i(k)) \qquad \text{(Eq. A.1)}$$

where

S_0^2 – amplitude reduction factor (intrinsic to absorber)
N – coordination number
$R = R_0 + \Delta R$, where R_0 is the distance between scatterer and absorber of the theoretical standard and ΔR is the change in distance (i.e. difference between standard and sample)
σ^2 – mean-square disorder parameter
$f(k)$ – effective scattering factor
$\delta(k)$ – effective scattering phase shift
$\lambda(k)$ – photoelectron mean free path
$k^2 = 2m_e(E - E_0)/\hbar$, where E_0 is difference in energy between standard and sample data.
The values of $f(k)$, $\delta(k)$, $\lambda(k)$, and R_0 were all calculated using theoretical standards (i.e. CIF files from ICSD) in the Artemis software/IFEFFIT.[9] The values of N, ΔR, E_0, and σ^2 were fit by the software. Uncertainties and r-factor values are directly from Artemis.

Table A.2. EXAFS fitting results for $V_yAl_{1-y}O_x$ films.

y in $V_yAl_{1-y}O_x$	V – O (Å)	N (atoms)	σ^2 (Å^2)	r-factor
1	1.60 (0.01)	2.0 (0.1)	0.003 (0.001)	0.007
1	1.85 (0.02)	2.9 (0.3)	0.003 (0.001)	0.007
0.7	1.71 (0.01)	4.4 (0.5)	0.004 (0.002)	0.008
0.5	1.70 (0.01)	4.5 (0.5)	0.006 (0.001)	0.008
0.3	1.70 (0.01)	4.5 (0.4)	0.004 (0.001)	0.006
0.2	1.71 (0.01)	4.3 (0.4)	0.003 (0.001)	0.006
0.1	1.71 (0.01)	4.5 (0.5)	0.003 (0.001)	0.009

S_0^2 value used for all fits was 0.73.

Table A.3. EXAFS fit results for $Cr_yAl_{1-y}O_x$ films.

y in $Cr_yAl_{1-y}O_x$	Cr – O (Å)	N (atoms)	σ^2 (Å^2)	r-factor	fraction Cr
1	1.99 (0.01)	6 (0.4)	0.002 (0.001)	0.006	1
0.5	1.60 (0.02)	4	0.008 (0.002)	0.026	0.7 (0.05)
0.5	1.88 (0.02)	6	0.003 (0.002)	0.026	0.2 (0.05)
0.3	1.61 (0.02)	4	0.008 (0.002)	0.02	0.75 (0.05)
0.3	1.88 (0.02)	6	0.001 (0.002)	0.02	0.25 (0.05)
0.2	1.62 (0.01)	4	0.006 (0.001)	0.0045	0.8 (0.05)
0.2	1.89 (0.02)	6	0.006 (0.003)	0.0045	0.2 (0.05)
0.1	1.62 (0.01)	4.0 (0.4)	0.008 (0.002)	0.01	1

S_0^2 value used for all fits was 0.76.

Table A.4. EXAFS fitting results for $Mn_yAl_{1-y}O_x$ films.

y in $Mn_yAl_{1-y}O_x$	Mn – O (Å)	N (atoms)	σ^2 (Å^2)	r-factor
1	1.90 (0.01)	6.0 (0.8)	0.004 (0.002)	0.009
0.7	1.90 (0.01)	4.4 (0.4)	0.005 (0.002)	0.01
0.4	1.88 (0.01)	3.2 (0.5)	0.005 (0.002)	0.01
0.3	1.88 (0.01)	4.0 (0.3)	0.004 (0.001)	0.004
0.2	1.88 (0.01)	4.0 (0.3)	0.004 (0.001)	0.004
0.1	1.88 (0.01)	3.9 (0.4)	0.004 (0.001)	0.008

S_0^2 value used for all fits was 0.7.

Table A.5. EXAFS fitting results for $Fe_yAl_{1-y}O_x$ films.

y in $Fe_yAl_{1-y}O_x$	Fe – O (Å)	N (atoms)	σ^2 (Å^2)	r-factor
1	1.93 (0.01)	3	0.003 (0.001)	0.008
1	2.10 (0.01)	3	0.003 (0.001)	0.008
0.7	1.93 (0.01)	4.4 (0.4)	0.007 (0.001)	0.001
0.3	1.92 (0.01)	4.6 (0.4)	0.007 (0.002)	0.002
0.2	1.93 (0.02)	4.1 (0.5)	0.005 (0.002)	0.003
0.1	1.93 (0.01)	4.4 (0.4)	0.006 (0.002)	0.002

S_0^2 value used for all fits was 0.75.

Table A.6. EXAFS fitting results for $Co_yAl_{1-y}O_x$ films.

y in $Co_yAl_{1-y}O_x$	Co – O (Å)	N (atoms)	σ^2 (Å^2)	r-factor
1	1.91 (0.02)	5.4 (0.8)	0.003(0.002)	0.018
0.3	1.91 (0.02)	5.3 (1.0)	0.004 (0.002)	0.03
0.2	1.92 (0.01)	5.8 (0.6)	0.005 (0.002)	0.01
0.1	1.97 (0.01)	4.9 (0.2)	0.006 (0.001)	0.002

S_0^2 value used for all fits was 0.75.

Table A.7. EXAFS fitting results for $Ni_yAl_{1-y}O_x$ films.

y in $Ni_yAl_{1-y}O_x$	Ni – O (Å)	N (atoms)	σ^2 (Å^2)	r-factor
1	2.07 (0.01)	5.6 (0.3)	0.004 (0.002)	0.01
0.3	2.04 (0.02)	6 (0.6)	0.009 (0.002)	0.002
0.2	2.03 (0.01)	5.7 (0.5)	0.009 (0.002)	0.002
0.1	2.01 (0.01)	3.7 (0.4)	0.006 (0.002)	0.003

S_0^2 value used for all fits was 0.85.

Table A.8. EXAFS fitting results for $Cu_yAl_{1-y}O_x$ films.

y in $Cu_yAl_{1-y}O_x$	Cu – O (Å)	N (atoms)	σ^2 (Å^2)	r-factor
1	1.94 (0.01)	3.9 (0.4)	0.002 (0.001)	0.008
0.7	1.94 (0.01)	4.2 (0.2)	0.002 (0.001)	0.01
0.5	1.93 (0.01)	3.7 (0.4)	0.004 (0.002)	0.009
0.3	1.92 (0.01)	4.0 (0.4)	0.004 (0.002)	0.01
0.2	1.92 (0.01)	4.0 (0.4)	0.005 (0.002)	0.01
0.1	1.91 (0.01)	4.2 (0.2)	0.006 (0.002)	0.013

S_0^2 value used for all fits was 0.8.

Table A.9. EXAFS fitting results for $Zn_yAl_{1-y}O_x$ films.

y in $Zn_yAl_{1-y}O_x$	Zn – O (Å)	N (atoms)	σ^2 (Å^2)	r-factor
1	1.97 (0.01)	4.0 (0.2)	0.004 (0.001)	0.0015
0.7	1.96 (0.01)	3.9 (0.2)	0.003 (0.001)	0.003
0.4	1.95 (0.01)	3.8 (0.4)	0.005 (0.002)	0.0035
0.3	1.95 (0.01)	3.9 (0.4)	0.005 (0.002)	0.005
0.2	1.97 (0.01)	3.9 (0.4)	0.005 (0.002)	0.003
0.1	1.97 (0.02)	4.2 (0.5)	0.006 (0.002)	0.007

S_0^2 value used for all fits was 0.8.

Table A.10. EXAFS fitting results for $Ga_yAl_{1-y}O_x$ films.

y in $Ga_yAl_{1-y}O_x$	Ga – O (Å)	N (atoms)	σ^2 (Å^2)	r-factor
1	1.89 (0.01)	4	0.003 (0.001)	0.011
1	2.08 (0.03)	6	0.007 (0.007)	0.011
0.5	1.88 (0.01)	4.3 (0.4)	0.005 (0.002)	0.008
0.3	1.88 (0.01)	4.2 (0.3)	0.004 (0.001)	0.004
0.2	1.88 (0.01)	4.2 (0.2)	0.004 (0.001)	0.002

S_0^2 value used for all fits was 0.8.

APPENDIX B

CHAPTER III SUPPORTING INFORMATION

Table B.1. Electrodeposition conditions for the electrodeposited $Ni_{1-z}M_zO_xH_y$ films.

Film ratio (XPS) Ni:M	Solution ratio Ni:M	Current density for deposition (mA cm^{-2})	Time of deposition (s)
Ni 87 : Ce 13	Ni 99 : Ce 1	-0.5	45
Ni 86 : La 14	Ni 90 : La 10	-1.0	55
Ni 92 : Mn 8	Ni 70 : Mn 30	-0.5	120
Ni 87 : Fe 13	Ni 97 : Fe 3	-0.1	38
Ni 60 : Ce 40	Ni 90 : Ce 10	-1.0	150
Ni 68 : La 32	Ni 70 : La 30	-2.0	90
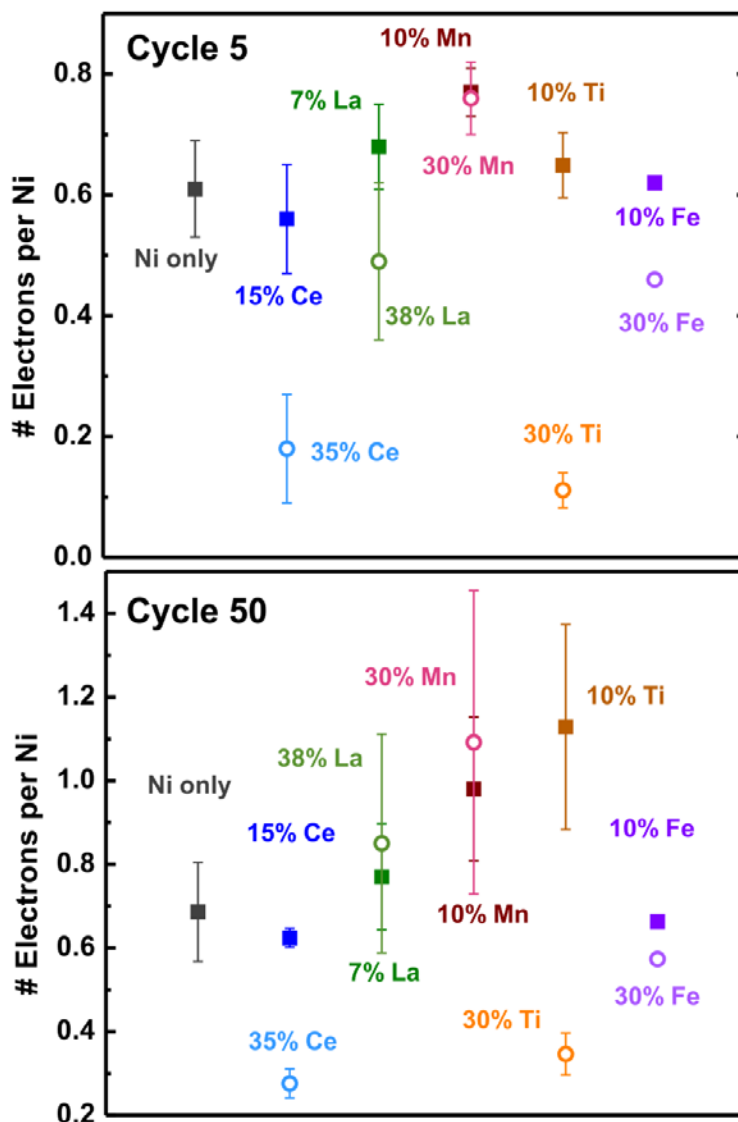
Figure B.1. Number of electrons removed per Ni atom during $Ni^{2+/3+}$ oxidation for spin-cast films, calculated from integration of the anodic peak. Total number of Ni atoms is obtained from the in situ mass determined by QCM. We find that for all the films synthesized, most only vary by a factor of 2, except films with higher content of Ce and Ti, which vary by a factor of 4. Since these differences are less than an order of magnitude, the films are nominally the same and differences in electrochemically active surface area do not affect the activity trends established in this work. We also note this calculation may be and underestimate of the number of electrons per Ni atom as the films likely suffer from lack of complete reversibility of oxidation, as has been shown for Ni-based (oxy)hydroxides.[1,2]
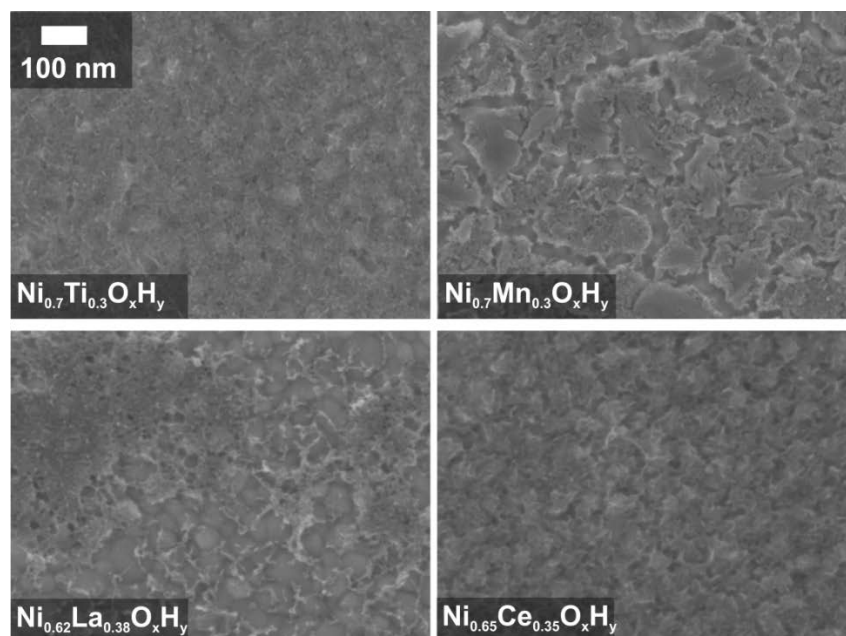
Figure B.2. Morphology of spin-cast $Ni_{1-z}M_zO_xH_y$ films where $z \sim 0.3$ after 50 cycles in 1 M Fe-free KOH at 20 mV s^{-1}.
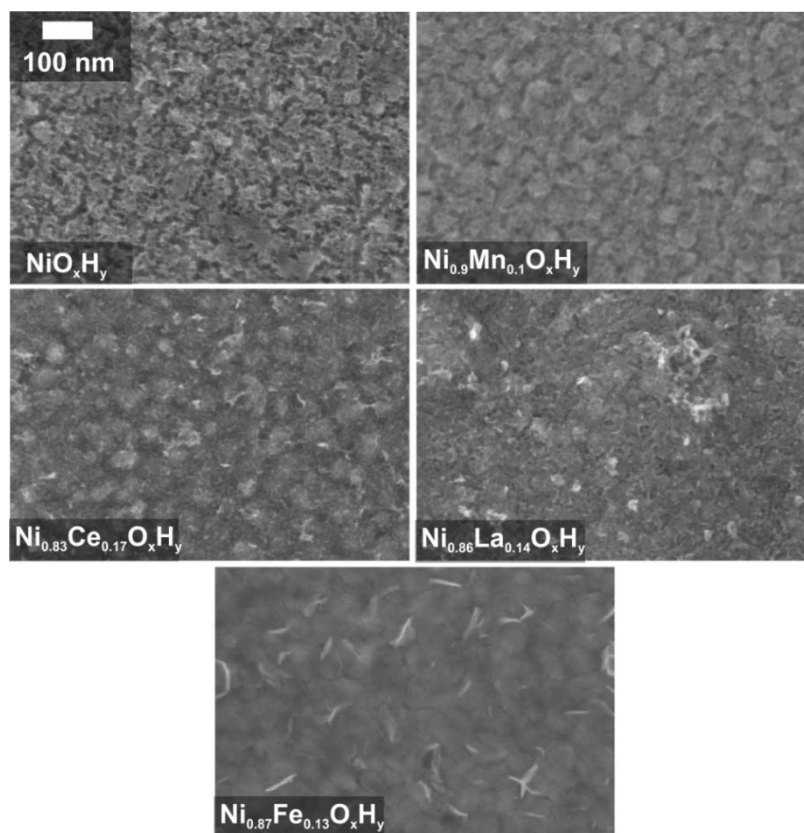
Figure B.3. Morphology of electrodeposited $Ni_{1-z}M_zO_xH_y$ films after 50 cycles in 1 M Fe-free KOH at 20 mV s^{-1}.

Table B.2. Overpotential at 0.5 mA cm^{-2} for spin-cast $Ni_{1-z}M_zO_xH_y$ films; this is referred to as the "OER onset potential" in Chapter III.

Composition	η @ j = 0.5 mA cm^{-2} (mV) cycle 5	η @ j = 0.5 mA cm^{-2} (mV) cycle 50	η @ j = 0.5 mA cm^{-2} (mV) Tafel
NiO_xH_y	389 ± 5	426 ± 2	419 ± 7
$Ni_{0.85}Ce_{0.15}O_xH_y$	315 ± 7	392 ± 6	430 ± 2
$Ni_{0.93}La_{0.7}O_xH_y$	369 ± 6	401 ± 5	428 ± 3
$Ni_{0.9}Mn_{0.1}O_xH_y$	385 ± 8	417 ± 7	432 ± 4
$Ni_{0.9}Ti_{0.1}O_xH_y$	402 ± 5	420 ± 7	434 ± 11
$Ni_{0.9}Fe_{0.1}O_xH_y$	277 ± 6	299 ± 3	297 ± 1
$Ni_{0.65}Ce_{0.35}O_xH_y$	322 ± 11	382 ± 11	-
$Ni_{0.62}La_{0.38}O_xH_y$	417 ± 7	436 ± 13	-
$Ni_{0.7}Mn_{0.3}O_xH_y$	402 ± 10	432 ± 10	-
$Ni_{0.7}Ti_{0.3}O_xH_y$	413 ± 12	403 ± 6	-
$Ni_{0.7}Fe_{0.3}O_xH_y$	248	279	-
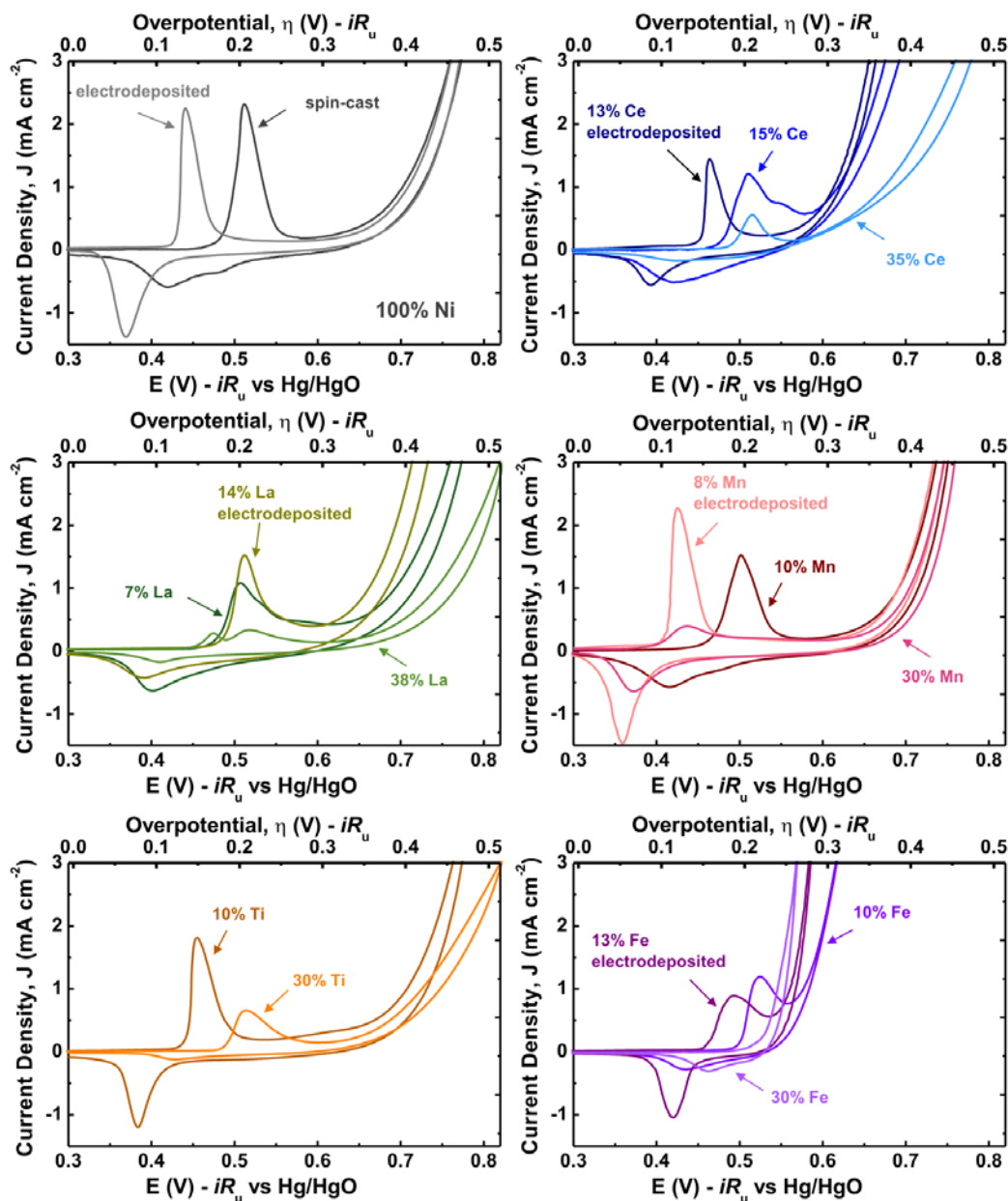
Figure B.4. Initial voltammograms (Cycle 1) of all spin-cast and electrodeposited film compositions taken at 20 mV s^{-1} in 1 M Fe-free KOH. Labels that do not specify preparation method are for spin-cast films. For most compositions, electrodeposited films show better redox reversibility, indicated by the similar area and sharpness of the anodic and cathodic redox waves.

93
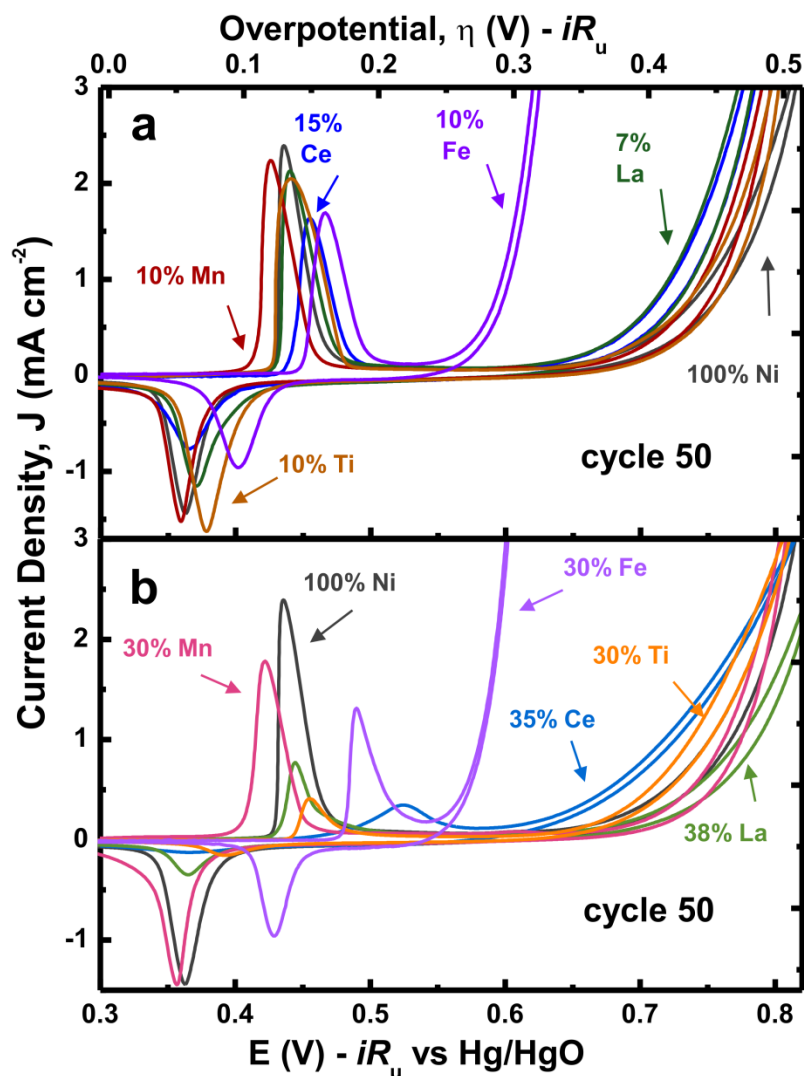
Figure B.5. Representative cyclic voltammograms of spin-cast $Ni_{1-z}M_zO_xH_y$ films at 20 mV s^{-1} in Fe-free 1 M KOH. Comparing cycle 5 (Figure 3.1 in the main text) to cycle 50 (Figure B.5) it is clear that all of the films exhibit a decrease in current density. As noted in the main text, the reduction in current density is most pronounced for $Ni(Ce)O_xH_y$ films.

Table B.3. Tafel slope and TOF_{tm} for spin-cast $Ni_{1-z}M_zO_xH_y$ films. Values marked with an asterisk (*) are extrapolated.

Composition	Tafel slope (mV dec^{-1})	TOF_{tm} (s^{-1}) @ η = 400 mV (Tafel)	TOF_{tm} (s^{-1}) @ η = 400 mV (CV cycle 5)	TOF_{tm} (s^{-1}) @ η = 400 mV (CV cycle 50)
NiO_xH_y	93 ± 2	0.02 ± 0.007	0.036 ± 0.004	0.016 ± 0.002
$Ni_{0.85}Ce_{0.15}O_xH_y$	126 ± 3	0.015 ± 0.006	0.26 ± 0.03	0.04 ± 0.01
$Ni_{0.93}La_{0.7}O_xH_y$	101 ± 2	0.022 ± 0.003	0.07 ± 0.01	0.04 ± 0.01
$Ni_{0.9}Mn_{0.1}O_xH_y$	92 ± 1	0.018 ± 0.002	0.05 ± 0.02	0.03 ± 0.01
$Ni_{0.9}Ti_{0.1}O_xH_y$	105 ± 2	0.021 ± 0.007	0.024 ± 0.003	0.019 ± 0.005
$Ni_{0.9}Fe_{0.1}O_xH_y$	40 ± 3	20 ± 6	7.02 ± 0.06*	7.01 ± 0.07*
$Ni_{0.65}Ce_{0.35}O_xH_y$	-	-	0.15 ± 0.05	0.03 ± 0.02
$Ni_{0.62}La_{0.38}O_xH_y$	-	-	0.035 ± 0.008	0.018 ± 0.006
$Ni_{0.7}Mn_{0.3}O_xH_y$	-	-	0.03 ± 0.01	0.02 ± 0.01
$Ni_{0.7}Ti_{0.3}O_xH_y$	-	-	0.019 ± 0.006	0.03 ± 0.01
$Ni_{0.7}Fe_{0.3}O_xH_y$	-	-	174 ± 86*	19 ± 5*
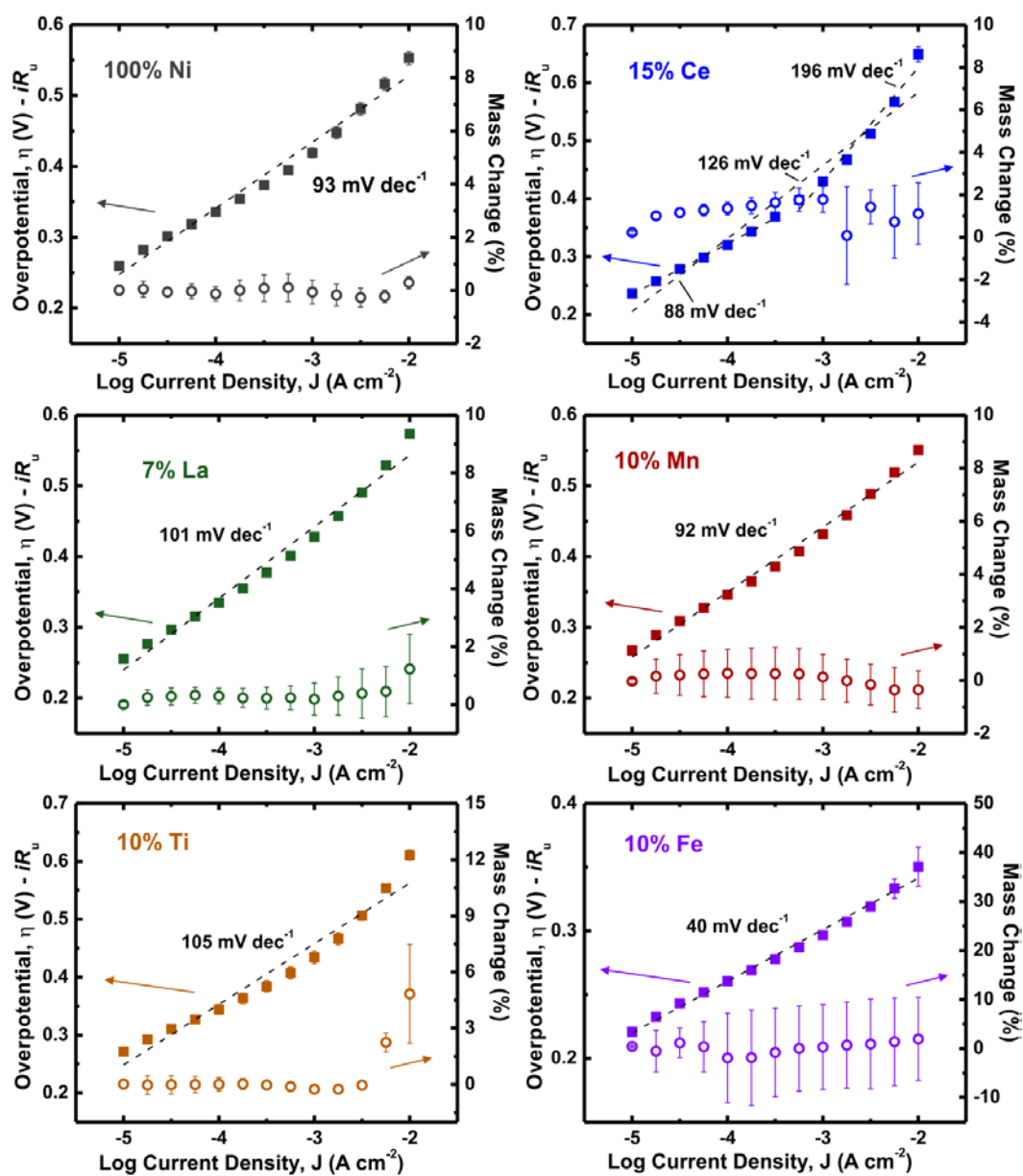
Figure B.6. Tafel plots for individual spin-cast $Ni_{1-z}M_zO_xH_y$ films along with *in situ* mass change. Symbols are the average and error bars represent the standard deviation of 3 individual samples.
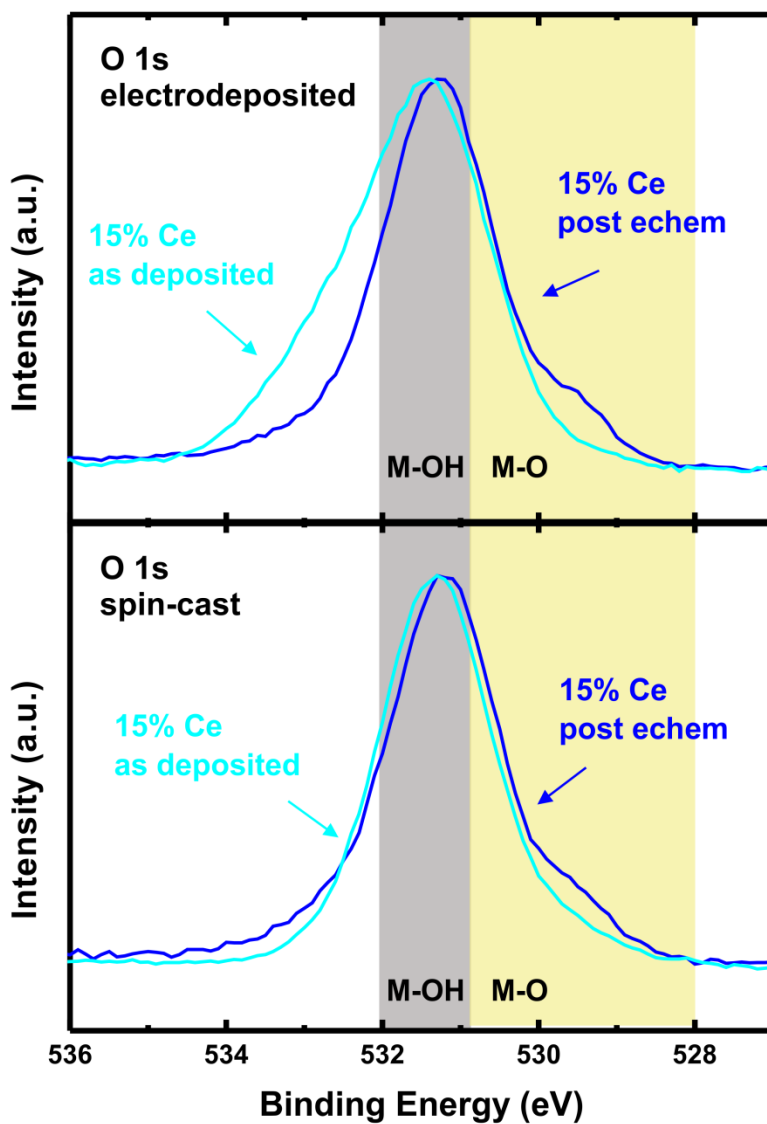
Figure B.7. O 1s XP spectra taken with Al Kα excitation of $Ni_{0.85}Ce_{0.15}O_xH_y$ films before and after 50 cycles at 20 mV s^{-1} in Fe-free 1 M KOH. All spectra were shifted so that the C 1s peak was centered at 284.8 eV with the exception of the spin-cast as-deposited spectrum which had significant charging issues likely due to residual H_2O and NO_3^- left in the film. It has been arbitrarily shifted in the figure (bottom) in order to compare peak shape.
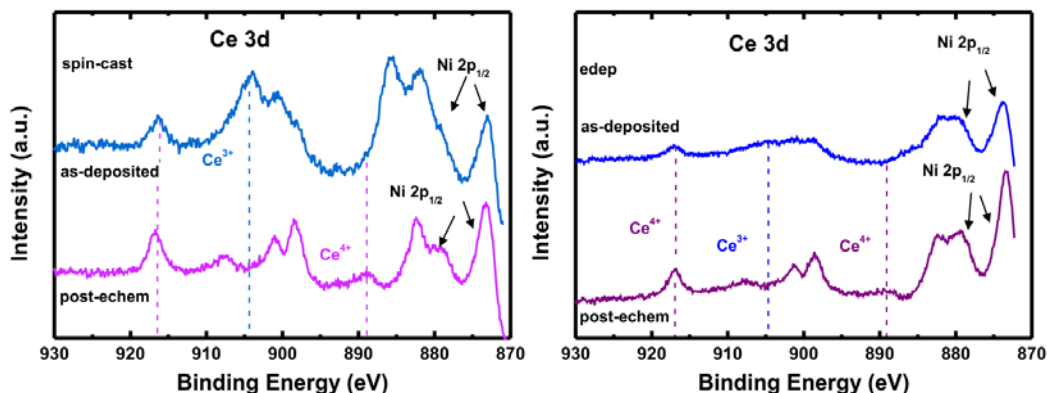
Figure B.8. Ce 3d XP spectra taken with Al Kα excitation for spin-cast (left) and electrodeposited (right) $Ni_{0.85}Ce_{0.15}O_xH_y$ films before and after 50 cycles at 20 mV s^{-1} in Fe-free 1 M KOH. The as-deposited films show evidence of both Ce^{3+} and Ce^{4+}, while the films after electrochemical analysis have only Ce^{4+}. Specifically, the distinct presence of the peak at ~905 eV corresponding to Ce^{3+} final states in as deposited $Ni_{0.85}Ce_{0.15}O_xH_y$ films suggests the film has a significant amount of Ce^{3+}. Conversely, the lack of this peak and the presence of a peak at ~889 eV, which corresponds to Ce^{4+} final states, indicate mainly Ce^{4+} in the $Ni_{0.85}Ce_{0.15}O_xH_y$ films after electrochemical cycling. Some of the distinct spectral features unique to Ce^{3+} (blue) or Ce^{4+} (purple) have been indicated by dashed lines.[3]
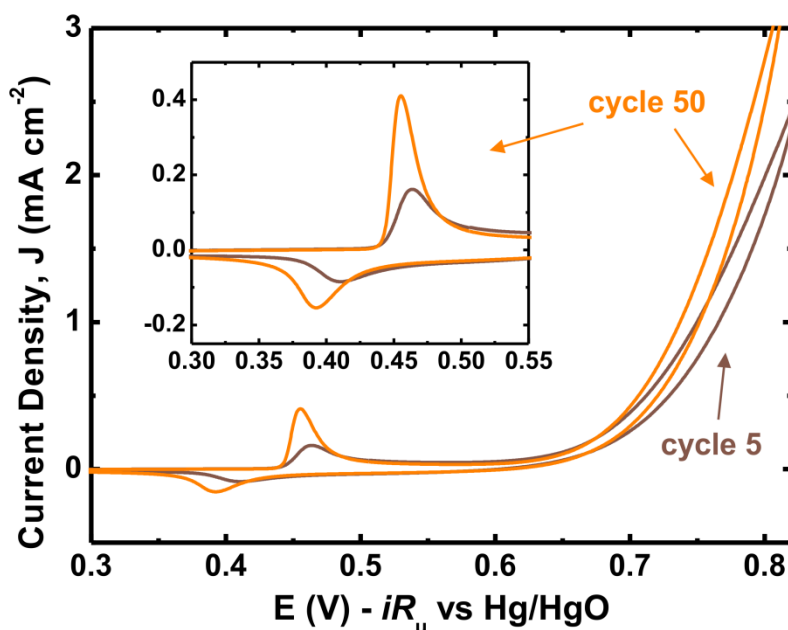
Figure B.9. Cyclic voltammetry of a representative $Ni_{0.7}Ti_{0.3}O_xH_y$ film in Fe-free 1 M KOH at 20 mV s^{-1}. Inset shows a magnification of the $Ni^{2+/3+}$ redox peaks. The increase in OER current from cycle 5 to cycle 50 is due to the increase in electrochemically active surface area as evident from the increase in the area of the $Ni^{2+/3+}$ oxidation peak.

98
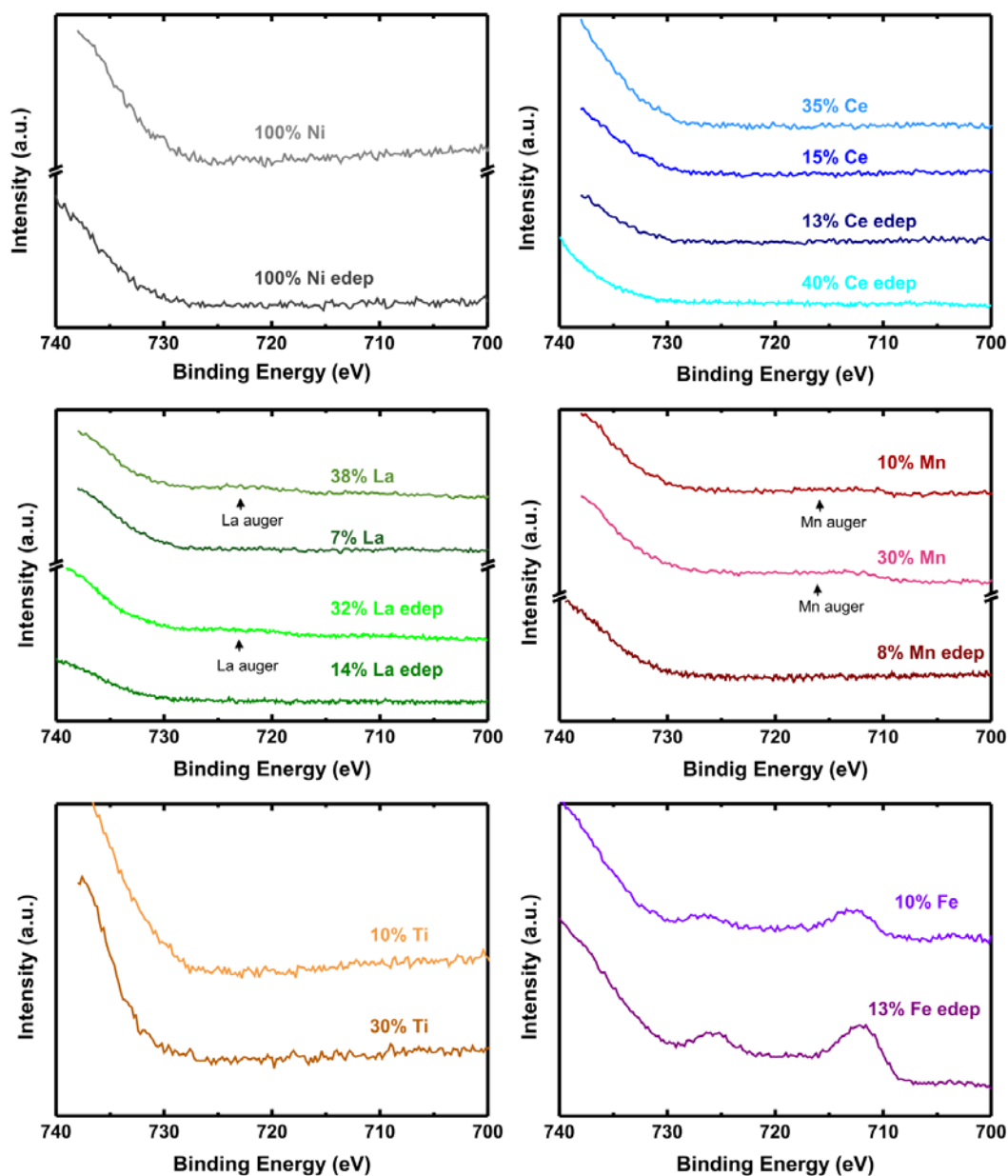
Figure B.10. XP spectra of Fe 2p region using Mg Kα excitation showing that there is no detectable Fe in the samples that do not intentionally contain Fe. The use of Mg Kα excitation is essential for Fe quantitation given interference from Ni auger peaks when the Al source is used.
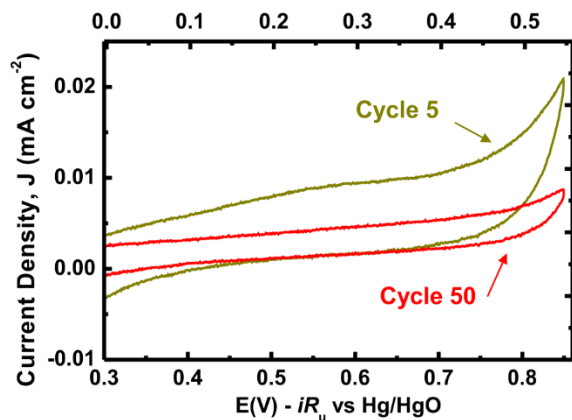
Figure B.11. Voltammetry of bare Au substrates at 20 mV s^{-1} in Fe-free 1 M KOH.
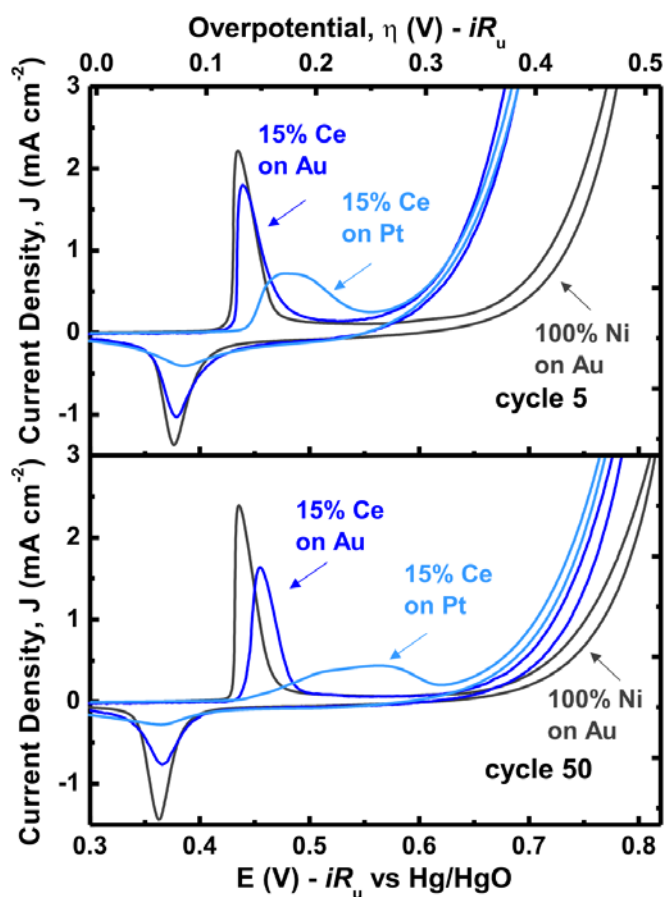
Figure B.12. Voltammetry comparison of spin-cast Ni$_{0.85}$Ce$_{0.15}$O$_x$H$_y$ on Au and Pt substrates. Ni$_{0.85}$Ce$_{0.15}$O$_x$H$_y$ shows similar current density at cycle 5 and 50 on either Pt or Au substrates. The activities at cycle 5 and 50 are also comparable: TOF$_{tm}$ cycle 5 = 0.26 s^{-1} (Au), 0.19 s^{-1} (Pt) TOF$_{tm}$ cycle 50 = 0.044 s^{-1} (Au), 0.038 s^{-1} (Pt). We note that the Ni$^{2+/3+}$ oxidation wave is significantly broader on Pt and attribute this to poorer

electrical connection of the film to Pt as well as higher resistance of the Pt QCM substrates.
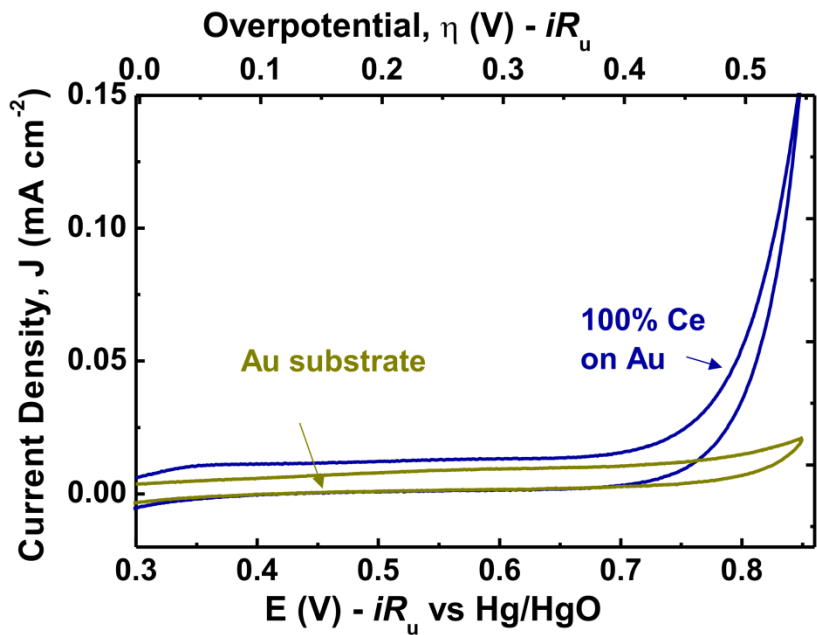
Figure B.13. Voltammetry (Cycle 5) of bare Au substrate and CeO_x film on Au substrate in 1 M Fe-free KOH at a scan rate of 20 mV s^{-1}.
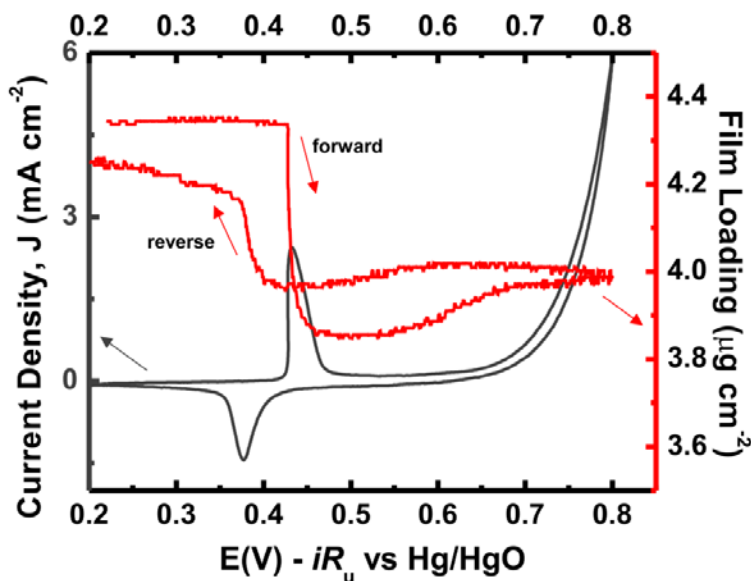
Figure B.14. Change in film loading during $Ni^{2+/3+}$ oxidation and reduction for a representative spin-cast NiO_xH_y film during cycle 5 at 20 mV s^{-1} in 1 M Fe-free KOH. Films in this work exhibit nominally β-Ni(OH)$_2$ behavior in that there is mass loss upon oxidation and mass gain upon reduction.[4] The exact ion/solvent movement responsible for these small mass changes is beyond the scope of this work.

101
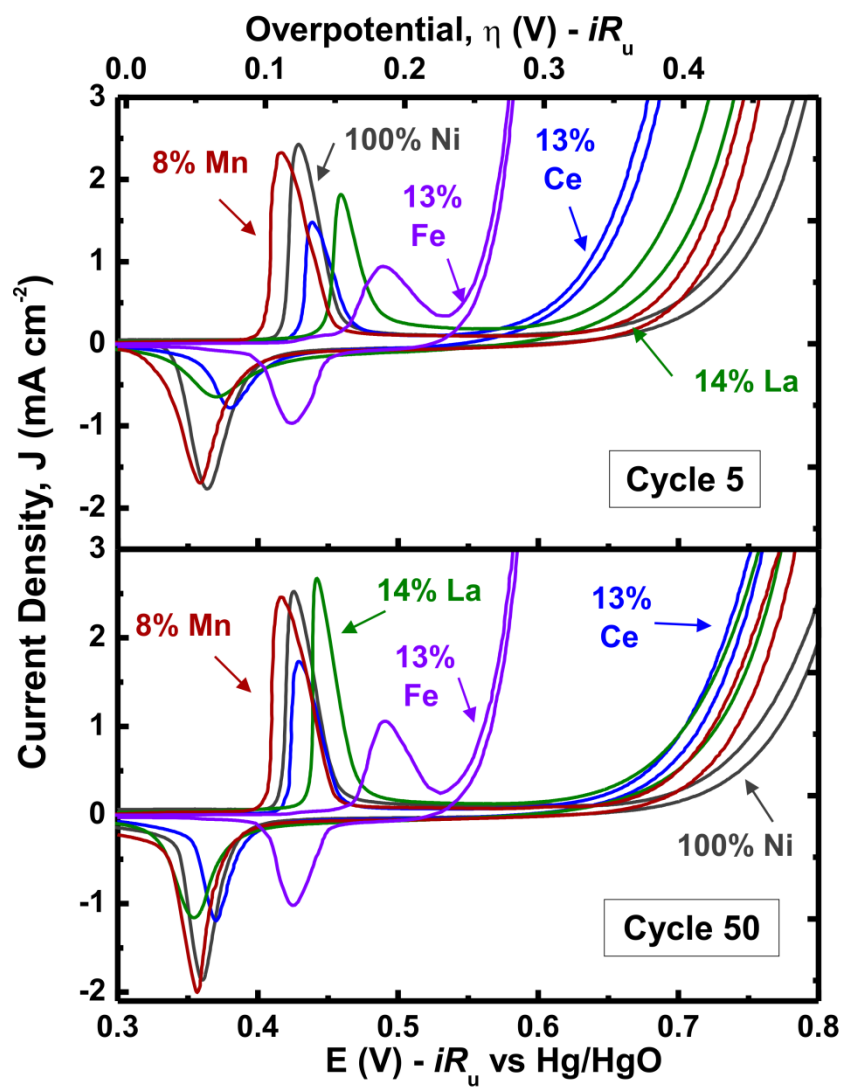
Figure B.15. Voltammetry of electrodeposited $Ni_{1-z}M_zO_xH_y$ films in 1 M Fe-free KOH at a scan rate of 20 mV s^{-1}.
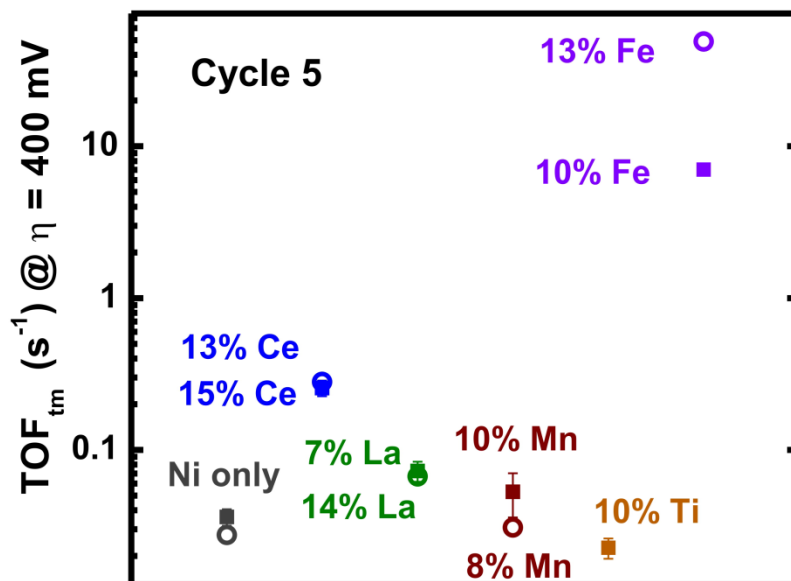
Figure B.16. Comparison of OER activity of electrodeposited (open circles) and spin-cast (solid squares) $Ni_{1-z}M_zO_xH_y$ films.
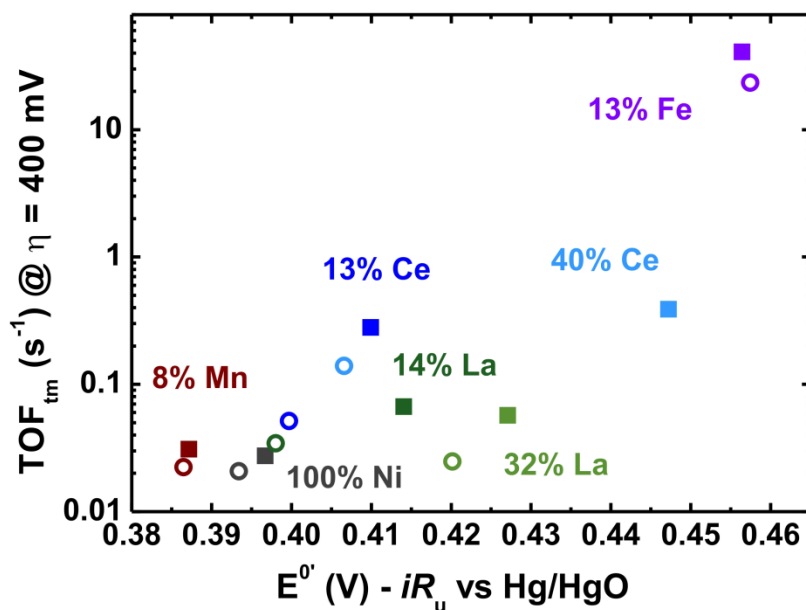
Figure B.17. TOF_{tm} vs. $E^{0'}$ of electrodeposited $Ni_{1-z}M_zO_xH_y$ films after 5 (solid squares) and 50 (open circles) cycles in Fe-free 1 M KOH at 20 mV s^{-1}.

Electrochemical Results
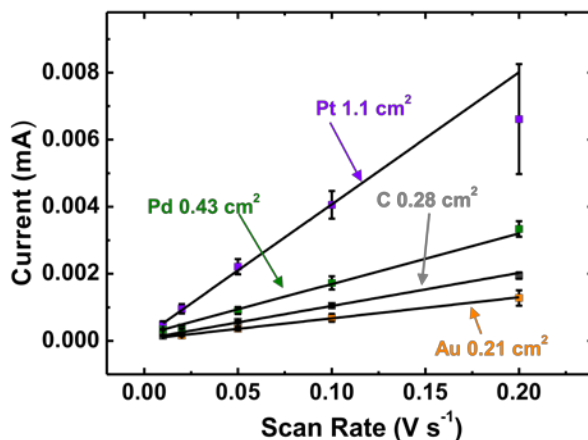
Figure C.1. Dependence of current response on scan rate for electrode substrates. Electrodes were cycled between 0.1 and 0.2 V vs Hg/HgO until current response was stable. The current plotted is the average of the absolute value of the anodic and cathodic current at 0.15 V vs Hg/HgO. Calculated surface areas are shown and are based on an average general capacitance of 0.035 mF cm^{-2}, adapted from Jaramillo et al.[1]
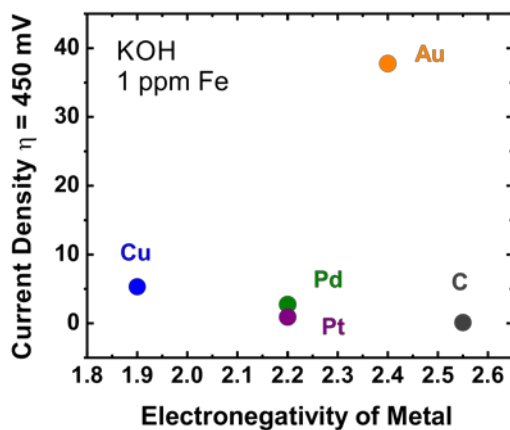
Figure C.2. Plot of current density at 450 mV overpotential vs Pauling's electronegativity of the electrode substrate material.
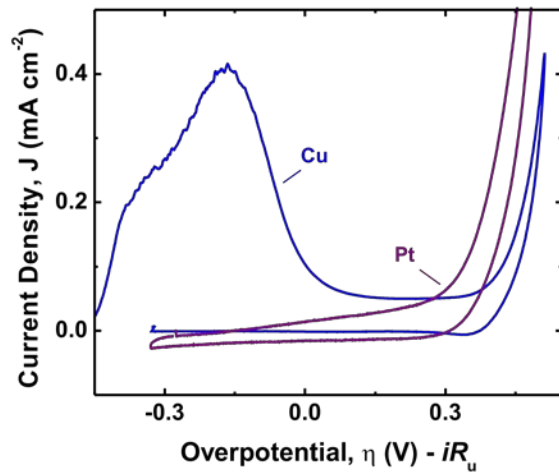
Figure C.3. Cyclic voltammetry at 20 mV s^{-1} of Pt (1 M KOH SC grade) and Cu (0.1 M KOH SC grade) electrodes showing irreversible oxidation of the surface. Cycle 1 is plotted for both.

Extended X-ray Absorption Fine Structure (EXAFS) Details

The EXAFS equation is described by the sum of all scattering paths, i, according to

$$\chi(k) = \sum_i \frac{S_0^2 N_i f_i(k)}{k R_i^2} e^{-\frac{2R_i}{\lambda(k)}} e^{-2k^2 \sigma_i^2} \sin(2kR_i + \delta_i(k)) \qquad \text{(Eq. D.1)}$$

where

S_0^2 – amplitude reduction factor (intrinsic to absorber)

N – coordination number

$R = R_0 + \Delta R$, where R_0 is the distance between scatterer and absorber of the theoretical standard and ΔR is the change in distance (i.e. difference between standard and sample)

σ^2 – mean-square disorder parameter

$f(k)$ – effective scattering factor

$\delta(k)$ – effective scattering phase shift

$\lambda(k)$ – photoelectron mean free path

$k^2 = 2m_e(E - E_0)/\hbar$, where E_0 is difference in energy between standard and sample data.

The values of $f(k)$, $\delta(k)$, $\lambda(k)$, and R_0 were all calculated using theoretical standards (i.e. CIF file from ICSD #556288) in the Artemis software/IFEFFIT.

The amplitude reduction factor, S_0^2, was set to 0.78 for Co and 0.75 for Fe, based on previous reports. The values of N, ΔR, E_0, and σ^2 were fit by the software. Uncertainties and r-factor values are directly from Artemis. The number of independent points ranged from 6.1 to 6.5, determined by the Nyquist criterion.
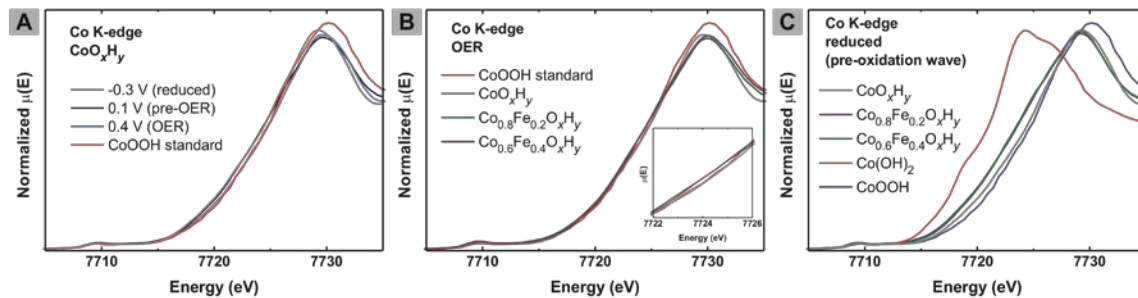
Figure D.1. Co K-edge XANES on Co(Fe)O_xH$_y$ films. A) Comparison of CoO$_x$H$_y$ films at various potentials with CoOOH standard. B) Comparison of films during the OER with CoOOH standard. C) Comparison of films held at potentials negative of the Co$^{2+/3+}$ oxidation wave (0 V or 0.05 V vs Hg/HgO) along with Co(OH)$_2$ and CoOOH standards.
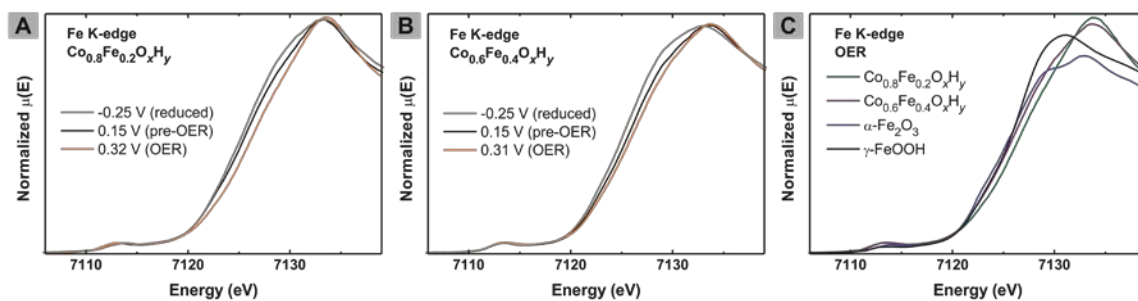
Figure D.2. Fe K-edge XANES of A) Co$_{0.8}$Fe$_{0.2}$O$_x$H$_y$ at various E_{app}, B) Co$_{0.6}$Fe$_{0.4}$O$_x$H$_y$ at various E_{app}, and C) Co(Fe)O$_x$H$_y$ films during the OER along with Fe standards.
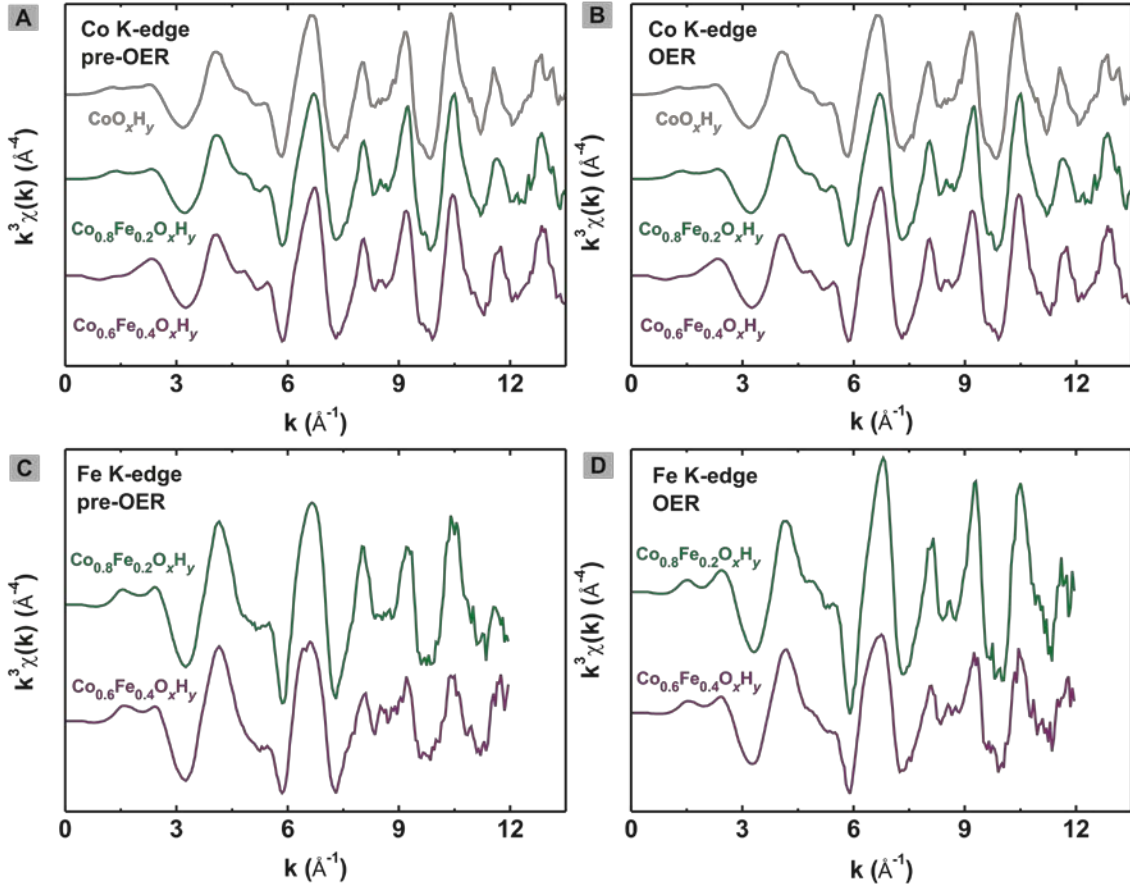
Figure D.3. k^3-weighted chi(k) data for Co(Fe)O$_x$H$_y$ films at A) the Co K-edge pre-OER, B) the Co-K-edge during OER, C) the Fe K-edge pre-OER, and D) the Fe K-edge during the OER in 1 M KOH.

Table D.1. Results of FT-EXAFS fitting for Co in Co(Fe)O$_x$H$_y$ films under applied potential in 1 M KOH.

Film Composition	pre-OER				OER			
	Co – O (Å)	N	σ^2 (Å^{-2})	R-factor	Co – O (Å)	N	σ^2 (Å^{-2})	R-factor
CoO$_x$H$_y$	1.90 (0.01)	5.5 (0.7)	0.003 (0.001)	0.014	1.90 (0.01)	5.7 (0.9)	0.002 (0.001)	0.021
Co$_{0.8}$Fe$_{0.2}$O$_x$H$_y$	1.90 (0.01)	5.3 (0.8)	0.002 (0.001)	0.019	1.90 (0.01)	5.4 (0.8)	0.002 (0.001)	0.018
Co$_{0.6}$Fe$_{0.4}$O$_x$H$_y$	1.90 (0.01)	5.6 (0.8)	0.003 (0.001)	0.018	1.90 (0.01)	5.6 (0.8)	0.002 (0.001)	0.014

Table D.2. Results of FT-EXAFS fitting for Fe in Co(Fe)O$_x$H$_y$ films under applied potential in 1 M KOH.

Film Composition	pre-OER				OER			
	Fe – O (Å)	N	σ^2 (Å^{-2})	R-factor	Fe – O (Å)	N	σ^2 (Å^{-2})	R-factor
Co$_{0.8}$Fe$_{0.2}$O$_x$H$_y$	1.93 (0.01)	5.0 (0.7)	0.005 (0.001)	0.012	1.90 (0.01)	4.7 (1.0)	0.002 (0.001)	0.018
Co$_{0.6}$Fe$_{0.4}$O$_x$H$_y$	1.93 (0.01)	5.4 (0.6)	0.007 (0.002)	0.009	1.90 (0.01)	4.8 (0.6)	0.005 (0.002)	0.011

Computational Details

The Vienna Ab-initio Simulation Package (VASP) program was used to perform spin-polarized DFT calculations[6,7] with the Perdew-Burke-Ernzerhof (PBE)[6] functional and the DFT+U formalism of Dudarev et al.[8] at a U-J term of 3.0 eV and 3.3 eV for Co and Fe, respectively, as usually for modeling catalysis of oxyhydroxides.[9–13] Projected-augmented wave (PAW) potentials replaced the core electrons of Co 1s2s2p3s3p, Fe 1s2s2p3s3p , and O 1s.[14,15]

The unit cell of CoOOH[10,16–19] was cleaved at the (0$\bar{1}$5) facet and the dopant was located at the active site as done previously for similar oxyhydroxides.[10,20] The energy cutoff and k-point Gamma-centered grid of 600 eV and 2×2×1, respectively were converged to within < 1 meV per atom. The ion positions convergence threshold was set until the force components on ions were less than 0.03 eV Å^{-1} while lattice vectors were held fixed for the surface in order to maintain the bulk geometry below.

The more commonly used reaction mechanism that has been proposed for several metal oxides includes these reaction steps:[21]

$$*OH_2 \rightarrow *OH + H^+ + e^- \tag{1}$$

$$*OH \rightarrow *O + H^+ + e^- \tag{2}$$

$$*O + H_2O \rightarrow * + 2H^+ + O_2 + 2e^- \tag{3}$$

$$* + H_2O \rightarrow *OH_2 \tag{4}$$
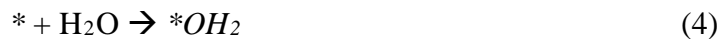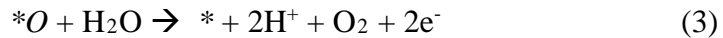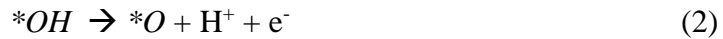
where intermediate "$*OH_2$" is the surface with a monolayer of adsorbed water molecules and intermediate "$*OH$" is the surface with an adsorbed hydroxyl group. Here intermediate "$*O$" has an oxygen termination, and "$*$" has a vacant termination. The

overpotential is defined as the applied voltage needed so that all reaction free energies are negative. The free energy for each reaction was calculated by subtracting reactants and products total energies and adding our calculated Zero Point Energy (ZPE) corrections and entropic contributions.

Our results support previous theoretical investigations that considered a different model and mechanism for pure and Fe-doped CoOOH.[19,22] Those models contained different number of transition metal ion layers and different facets. In addition, we did not include the *OOH surface reaction intermediate since we found in previous work that this reaction intermediate is unstable in some cases.[23] Nevertheless, we accounted for the *OH_2 surface since this intermediate was proposed for other oxides.[24] The free energy for the direct reaction of $* \rightarrow *OH$, which was obtained by summing the free energies of reactions 1 and 4 equals -0.57 eV and 0.26 eV for pure and Fe-doped CoOOH, respectively; hence, this route also a possibility that is included in the model. In agreement with previous studies,[22] we also find lower overpotential upon doping with Fe for CoOOH as detailed below.

Computational Results

Below is additional information on the calculation data, including bond lengths, atomic magnetization, free energies and overpotential, and optimized structures.
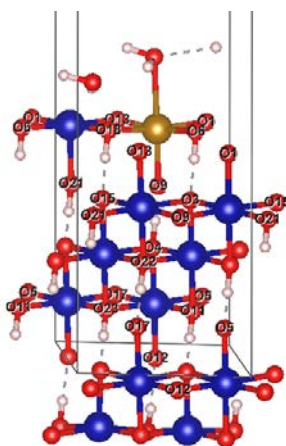
Figure D.4. Atomic position labelling for Fe-doped CoOOH demonstrated for intermediate *OH_2.

Table D.3. Fe-O bond distances around the Fe active site for Fe-doped CoOOH.

Termination	*OH₂	*OH	*O	*
d_Fe1-O1 [Å]	1.923	1.933	1.920	1.875
d_Fe1-O9 [Å]	1.962	1.913	2.058	1.933
d_Fe1-O13 [Å]	1.921	1.900	1.885	1.876
d_Fe1-O18 [Å]	1.964	1.911	1.904	1.892
d_Fe1-O6 [Å]	1.959	1.897	1.928	1.905
Average [Å]	1.946	1.911	1.939	1.896
Standard deviation [Å]	0.019	0.013	0.061	0.022

Table D.4. Co-O bond distances far away from the active site for Fe-doped CoOOH.

Termination	*OH₂	*OH	*O	*
d_Co4-O4 [Å]	1.951	1.972	1.974	1.926
d_Co4-O23 [Å]	1.917	1.918	1.915	1.898
d_Co4-O17 [Å]	1.895	1.909	1.899	1.882
d_Co4-O12 [Å]	1.903	1.904	1.898	1.912
d_Co4-O5 [Å]	1.893	1.884	1.894	1.918
d_Co4-O11 [Å]	1.916	1.907	1.914	1.926
Average [Å]	1.913	1.916	1.915	1.910
Standard deviation [Å]	0.021	0.030	0.030	0.015

Table D.5. Co-O bond distances close to the active site for Fe-doped CoOOH.

Termination	*OH₂	*OH	*O	*
d_Co7-O9 [Å]	1.918	1.920	1.909	1.905
d_Co7-O3 [Å]	1.913	1.912	1.912	1.912
d_Co7-O15 [Å]	1.915	1.897	1.915	1.918
d_Co7-O13 [Å]	1.916	1.892	1.865	1.927
d_Co7-O21 [Å]	1.914	1.916	1.919	1.910
d_Co7-O22 [Å]	1.926	1.957	1.963	1.915
Average [Å]	**1.917**	**1.916**	**1.914**	**1.915**
Standard deviation [Å]	0.002	0.011	0.020	0.008

Table D.6. Co-O bond distances around the Co active site for pure CoOOH.

Termination	$*OH_2$	$*OH$	$*O$	$*$
d_Co12-O1 [Å]	1.903	1.885	1.917	1.913
d_Co12-O6 [Å]	1.909	1.895	1.911	1.897
d_Co12-O18 [Å]	1.913	1.854	1.886	1.878
d_Co12-O13 [Å]	1.891	1.910	1.893	1.867
d_Co12-O9 [Å]	1.881	1.929	2.007	2.021
Average [Å]	**1.900**	**1.895**	**1.923**	**1.915**
Standard deviation [Å]	0.073	0.022	0.102	0.017

The atomic oxidation states at the active site were estimated according to the calculated atomic magnetization. The magnetic moments on Fe^{2+}, Fe^{3+}, Fe^{4+}, and Fe^{5+} are anticipated to be M = 4, 5, 4, and 3, respectively, at high-spin valence configurations of $3d^6$, $3d^5$, $3d^4$, and $3d^3$. The magnetic moments on Co^{2+}, Co^{3+}, and Co^{4+} are anticipated to be M = 3, 4, and 5, respectively, at high-spin valence configurations of $3d^7$, $3d^6$, and $3d^5$. The corresponding low-spin configurations for Co^{2+}, Co^{3+}, and Co^{4+} can be associated with M = 1, (0 or 2), and (1 or 3), respectively. At DFT+U calculations the magnetic moments are typically smaller due to the slightly delocalized nature of the atomic orbitals. The expected oxidation state of Fe or Co in CoOOH is 3+ according to the material's stoichiometry, but the metals may have a distribution of oxidation states. Furthermore, during the reaction the oxidation state of the active site may increase upon deprotonation. Taking all of these into consideration, we provide estimate the oxidation state of the active site as given in Table D.7.

Table D.7. Atomic magnetization and estimated oxidation state (in parenthesis) at the Fe and Co active sites for pure and Fe-doped CoOOH, respectively.

	$*OH_2$	$*OH$	$*O$	$*$
Fe-doped CoOOH	3.9 (3+)	3.3 (4+)	2.6 (5+)	3.6 (3+)
pure CoOOH	0.0 (3+)	1.0 (4+)	1.2 (4+)	1.9 (3+)

Table D.8. Free energies for water oxidation reaction intermediates for pure and Fe-doped CoOOH. The free energies are normalized per electron participating in the reaction. Hence, the free energy of reaction $*O \rightarrow *$ is divided by two. The largest free energy is indicated in bold.

				Reaction
pure CoOOH	ΔG_4 [eV]		-1.97	$* \rightarrow *OH_2$
	ΔG_1 [eV]		1.40	$*OH_2 \rightarrow *OH$
	ΔG_2 [eV]		**2.29**	$*OH \rightarrow *O$
	$\Delta G_3/2$ [eV]		1.37	$*O \rightarrow *$
	Overpotential [eV]		1.19	
Fe-doped CoOOH	ΔG_4 [eV]		-1.22	$* \rightarrow *OH_2$
	ΔG_1 [eV]		1.48	$*OH_2 \rightarrow *OH$
	ΔG_2 [eV]		**1.60**	$*OH \rightarrow *O$
	$\Delta G_3/2$ [eV]		1.30	$*O \rightarrow *$
	Overpotential [eV]		0.59	

Table D.9. Zero-point energy (ZPE) and entropy corrections at each reaction step for pure and Fe-doped CoOOH.

Doped	Pure	
-0.364	-0.385	$\left(\Delta(ZPE) - T\Delta(S)\right)_1$
-0.360	-0.362	$\left(\Delta(ZPE) - T\Delta(S)\right)_2$
-0.665	-0.636	$\left(\Delta(ZPE) - T\Delta(S)\right)_3$
0.790	0.792	$\left(\Delta(ZPE) - T\Delta(S)\right)_4$

REFERENCES CITED

CHAPTER II

(1)   Hennek, J. W.; Kim, M. G.; Kanatzidis, M. G.; Facchetti, A.; Marks, T. J. Exploratory Combustion Synthesis: Amorphous Indium Yttrium Oxide for Thin-Film Transistors. *J. Am. Chem. Soc.* **2012**, *134*, 9593–9596.

(2)   Nadarajah, A.; Carnes, M. E.; Kast, M. G.; Johnson, D. W.; Boettcher, S. W. Aqueous Solution Processing of F-Doped SnO_2 Transparent Conducting Oxide Films Using a Reactive Tin(II) Hydroxide Nitrate Nanoscale Cluster. *Chem. Mater.* **2013**, *25*, 4080–4087.

(3)   Nadarajah, A.; Wu, M. Z. B.; Archila, K.; Kast, M. G.; Smith, A. M.; Chiang, T. H.; Keszler, D. A.; Wager, J. F.; Boettcher, S. W. Amorphous In–Ga–Zn Oxide Semiconducting Thin Films with High Mobility from Electrochemically Generated Aqueous Nanocluster Inks. *Chem. Mater.* **2015**, *27*, 5587–5596.

(4)   Kim, S.; Gil, Y.; Choi, Y.; Kim, K.-K.; Yun, H. J.; Son, B.; Choi, C.; Kim, H. Carrier Transport at Metal/Amorphous Hafnium–Indium–Zinc Oxide Interfaces. *ACS Appl. Mater. Interfaces* **2015**, *7*, 22385–22393.

(5)   Leong, W. L.; Ren, Y.; Seng, H. L.; Huang, Z.; Chiam, S. Y.; Dodabalapur, A. Efficient Polymer Solar Cells Enabled by Low Temperature Processed Ternary Metal Oxide as Electron Transport Interlayer with Large Stoichiometry Window. *ACS Appl. Mater. Interfaces* **2015**, *7*, 11099–11106.

(6)   Qin, P.-L.; Lei, H.-W.; Zheng, X.-L.; Liu, Q.; Tao, H.; Yang, G.; Ke, W.-J.; Xiong, L.-B.; Qin, M.-C.; Zhao, X.-Z.; et al. Copper-Doped Chromium Oxide Hole-Transporting Layer for Perovskite Solar Cells: Interface Engineering and Performance Improvement. *Adv. Mater. Interfaces* **2016**, *3*, No. 1500799.

(7)   Moriceau, P.; Lebouteiller, A.; Bordes, E.; Courtine, P. A New Concept Related to Selectivity in Mild Oxidation Catalysis of Hydrocarbons: The Optical Basicity of Catalyst Oxygen. *Phys. Chem. Chem. Phys.* **1999**, *1*, 5735–5744.

(8)   Routray, K.; Zhou, W.; Kiely, C. J.; Wachs, I. E. Catalysis Science of Methanol Oxidation over Iron Vanadate Catalysts: Nature of the Catalytic Active Sites. *ACS Catal.* **2011**, *1*, 54–66.

(9)   Getsoian, A.; Zhai, Z.; Bell, A. T. Band-Gap Energy as a Descriptor of Catalytic Activity for Propene Oxidation over Mixed Metal Oxide Catalysts. *J. Am. Chem. Soc.* **2014**, *136*, 13684–13697.

(10)   Smith, R. D. L.; Prévot, M. S.; Fagan, R. D.; Zhang, Z.; Sedach, P. A.; Siu, M. K. J.; Trudel, S.; Berlinguette, C. P. Photochemical Route for Accessing Amorphous Metal Oxide Materials for Water Oxidation Catalysis. *Science* **2013**, *340*, 60–63.

(11)   Velu, S.; Suzuki, K.; Osaki, T. Oxidative Steam Reforming of Methanol over

CuZnAl(Zr)-Oxide Catalysts; a New and Efficient Method for the Production of CO-Free Hydrogen for Fuel Cells. *Chem. Commun.* **1999**, *0*, 2341–2342.

(12) Subramanian, V.; Gnanakumar, E. S.; Jeong, D.-W.; Han, W.-B.; Gopinath, C. S.; Roh, H.-S. A Rationally Designed $CuFe_2O_4$–mesoporous Al_2O_3 Composite towards Stable Performance of High Temperature Water–gas Shift Reaction. *Chem. Commun.* **2013**, *49*, 11257–11259.

(13) Li, D.; Li, X.; Gong, J. Catalytic Reforming of Oxygenates: State of the Art and Future Prospects. *Chem. Rev.* **2016**, *116*, 11529–11653.

(14) Zhou, N.; Kim, M.-G.; Loser, S.; Smith, J.; Yoshida, H.; Guo, X.; Song, C.; Jin, H.; Chen, Z.; Yoon, S. M.; et al. Amorphous Oxide Alloys as Interfacial Layers with Broadly Tunable Electronic Structures for Organic Photovoltaic Cells. *Proc. Natl. Acad. Sci.* **2015**, *112*, 7897–7902.

(15) May, K. J.; Carlton, C. E.; Stoerzinger, K. A.; Risch, M.; Suntivich, J.; Lee, Y. L.; Grimaud, A.; Shao-Horn, Y. Influence of Oxygen Evolution during Water Oxidation on the Surface of Perovskite Oxide Catalysts. *J. Phys. Chem. Lett.* **2012**, *3*, 3264–3270.

(16) Trudel, S.; Daryl Crozier, E.; Gordon, R. A.; Budnik, P. S.; Hill, R. H. X-Ray Absorption Fine Structure Study of Amorphous Metal Oxide Thin Films Prepared by Photochemical Metalorganic Deposition. *J. Solid State Chem.* **2011**, *184*, 1025–1035.

(17) Arhammar, C.; Pietzsch, A.; Bock, N.; Holmstrom, E.; Araujo, C. M.; Grasjo, J.; Zhao, S.; Green, S.; Peery, T.; Hennies, F.; et al. Unveiling the Complex Electronic Structure of Amorphous Metal Oxides. *Proc. Natl. Acad. Sci.* **2011**, *108*, 6355–6360.

(18) Medvedeva, J. E.; Buchholz, D. B.; Chang, R. P. H. Recent Advances in Understanding the Structure and Properties of Amorphous Oxide Semiconductors. *Adv. Electron. Mater.* **2017**, *3*, No. 1700082.

(19) Zimmermann, R.; Steiner, P.; Claessen, R.; Reinert, F.; Hüfner, S.; Blaha, P.; Dufek, P. Electronic Structure of 3d-Transition-Metal Oxides: On-Site Coulomb Repulsion versus Covalency. *J. Phys. Condens. Matter* **1999**, *11*, 1657–1682.

(20) Biswas, P.; Tafen, D. N.; Inam, F.; Cai, B.; Drabold, D. A. Materials Modeling by Design: Applications to Amorphous Solids. *J. Phys. Condens. Matter* **2009**, *21*, No. 084207.

(21) Lee, S. K.; Lee, S. B.; Park, S. Y.; Yi, Y. S.; Ahn, C. W. Structure of Amorphous Aluminum Oxide. *Phys. Rev. Lett.* **2009**, *103*, 4–7.

(22) Lee, S. K.; Park, S. Y.; Yi, Y. S.; Moon, J. Structure and Disorder in Amorphous Alumina Thin Films: Insights from High-Resolution Solid-State NMR. *J. Phys. Chem. C* **2010**, *114*, 13890–13894.

(23) Sarou-Kanian, V.; Gleizes, A. N.; Florian, P.; Samélor, D.; Massiot, D.; Vahlas, C.

Temperature-Dependent 4-, 5- and 6-Fold Coordination of Aluminum in MOCVD-Grown Amorphous Alumina Films: A Very High Field ^{27}Al-NMR Study. *J. Phys. Chem. C* **2013**, *117*, 21965–21971.

(24) Machala, L.; Zboril, R.; Gedanken, A. Amorphous Iron(III) Oxide - A Review. *J. Phys. Chem. B* **2007**, *111*, 4003–4018.

(25) Nomura, K.; Kamiya, T.; Ohta, H.; Uruga, T.; Hirano, M.; Hosono, H. Local Coordination Structure and Electronic Structure of the Large Electron Mobility Amorphous Oxide Semiconductor In-Ga-Zn-O: Experiment and Ab Initio Calculations. *Phys. Rev. B - Condens. Matter Mater. Phys.* **2007**, *75*, 2–6.

(26) Filatova, E. O.; Konashuk, A. S. Interpretation of the Changing the Band Gap of Al_2O_3 Depending on Its Crystalline Form: Connection with Different Local Symmetries. *J. Phys. Chem. C* **2015**, *119*, 20755–20761.

(27) Kast, M. G.; Cochran, E. A.; Enman, L. J.; Mitchson, G.; Ditto, J.; Siefe, C.; Plassmeyer, P. N.; Greenaway, A. L.; Johnson, D. C.; Page, C. J.; et al. Amorphous Mixed-Metal Oxide Thin Films from Aqueous Solution Precursors with Near-Atomic Smoothness. *J. Am. Chem. Soc.* **2016**, *138*, 16800–16808.

(28) Velu, S.; Suzaki, K.; Gopinath, C. S. Photoemission and in Situ XRD Investigations on CuCoZnAl-Mixed Metal Oxide Catalysts for the Oxidative Steam Reforming of Methanol. *J. Phys. Chem. B* **2002**, *106*, 12737–12746.

(29) Velu, S.; Suzuki, K.; Vijayaraj, M.; Barman, S.; Gopinath, C. S. In Situ XPS Investigations of $Cu_{1-x}Ni_x$ZnAl-Mixed Metal Oxide Catalysts Used in the Oxidative Steam Reforming of Bio-Ethanol. *Appl. Catal. B Environ.* **2005**, *55*, 287–299.

(30) Fu, L. J.; Li, X. Y.; Liu, M. Z.; Yang, H. M. Insights into the Nature of Cu Doping in Amorphous Mesoporous Alumina. *J. Mater. Chem. A* **2013**, *1*, 14592–14605.

(31) Fu, L.; Yang, H.; Hu, Y.; Wu, D.; Navrotsky, A. Tailoring Mesoporous γ-Al_2O_3 Properties by Transition Metal Doping: A Combined Experimental and Computational Study. *Chem. Mater.* **2017**, *29*, 1338–1349.

(32) Mathew, T.; Sivaranjani, K.; Gnanakumar, E. S.; Yamada, Y.; Kobayashi, T.; Gopinath, C. S. γ-$Al_{2-x}M_xO_{3\pm y}$ (M = Ti^{4+} through Ga^{3+}): Potential Pseudo-3D Mesoporous Materials with Tunable Acidity and Electronic Structure. *J. Mater. Chem.* **2012**, *22*, 13484–13493.

(33) Lin, Q.; Su, Y.; Zhang, M.-J.; Yang, X.; Yuan, S.; Hu, J.; Lin, Y.; Liang, J.; Pan, F. A Novel P-Type and Metallic Dual-Functional Cu–Al_2O_3 Ultra-Thin Layer as the Back Electrode Enabling High Performance of Thin Film Solar Cells. *Chem. Commun.* **2016**, *52*, 10708–10711.

(34) Wang, W.; Liu, W.; Chang, I.-Y.; Wills, L. A.; Zakharov, L. N.; Boettcher, S. W.; Cheong, P. H.-Y.; Fang, C.; Keszler, D. A. Electrolytic Synthesis of Aqueous Aluminum Nanoclusters and in Situ Characterization by Femtosecond Raman

Spectroscopy and Computations. *Proc. Natl. Acad. Sci.* **2013**, *110*, 18397–18401.

(35) Ravel, B.; Newville, M. ATHENA, ARTEMIS, HEPHAESTUS: Data Analysis for X-Ray Absorption Spectroscopy Using IFEFFIT. *J. Synchrotron Radiat.* **2005**, *12*, 537–541.

(36) Bachmann, H. G.; Ahmed, F. R.; Barnes, W. H. The Crystal Structure of Vanadium Pentoxide. *Zeitschrift für Krist. - Cryst. Mater.* **1961**, *115*, 110–131.

(37) Sawada, H. Residual Electron Density Study of Chromium Sesquioxide by Crystal Structure and Scattering Factor Refinement. *Mater. Res. Bull.* **1994**, *29*, 239–245.

(38) Stephens, J. S.; Cruickshank, D. W. J. The Crystal Structure of $(CrO_3)\infty$. *Acta Crystallogr. Sect. B Struct. Crystallogr. Cryst. Chem.* **1970**, *26*, 222–226.

(39) Geller, S. Structure of α-Mn_2O_3, $(Mn_{0.983}Fe_{0.017})_2O_3$ and $(Mn_{0.37}Fe_{0.63})_2O_3$ and Relation to Magnetic Ordering. *Acta Crystallogr. Sect. B Struct. Crystallogr. Cryst. Chem.* **1971**, *27*, 821–828.

(40) Blake, R. L.; Hessevick, R. E.; Zoltai, T.; Finger, L. W. Refinement of the Hematite Structure. *Am. Mineral.* **1966**, *51*, 123–129.

(41) Will, G.; Masciocchi, N.; Parrish, W.; Hart, M. Refinement of Simple Crystal Structures from Synchrotron Radiation Powder Diffraction Data. *J. Appl. Crystallogr.* **1987**, *20*, 394–401.

(42) Sasaki, S.; Fujino, K.; Takeuchi, Y. X-Ray Determination of Electron-Density Distributions in Oxides, MgO, MnO, CoO, and NiO, and Atomic Scattering Factors of Their Constituent Atoms. *Proc. Jpn. Acad.* **1979**, *55*, 43–48.

(43) Åsbrink, S.; Norrby, L. J. A Refinement of the Crystal Structure of Copper(II) Oxide with a Discussion of Some Exceptional E.s.d.'s. *Acta Crystallogr. Sect. B Struct. Crystallogr. Cryst. Chem.* **1970**, *26*, 8–15.

(44) Abrahams, S. C.; Bernstein, J. L. Remeasurement of the Structure of Hexagonal ZnO. *Acta Crystallogr. Sect. B Struct. Crystallogr. Cryst. Chem.* **1969**, *25*, 1233–1236.

(45) Geller, S. Crystal Structure of β-Ga_2O_3. *J. Chem. Phys.* **1960**, *33*, 676–684.

(46) Ravel, B. ATOMS: Crystallography for the X-Ray Absorption Spectroscopist. *J. Synchrotron Radiat.* **2001**, *8*, 314–316.

(47) Newville, M. IFEFFIT : Interactive XAFS Analysis and FEFF Fitting. *J. Synchrotron Radiat.* **2001**, *8*, 322–324.

(48) Buchholz, D. B.; Liu, J.; Marks, T. J.; Zhang, M.; Chang, R. P. H. Control and Characterization of the Structural, Electrical, and Optical Properties of Amorphous Zinc-Indium-Tin Oxide Thin Films. *ACS Appl. Mater. Interfaces* **2009**, *1*, 2147–2153.

(49) Tauc, J.; Menth, A. States in the Gap. *J. Non. Cryst. Solids* **1972**, *8–10*, 569–585.

(50)   Wulfsberg, G. *Inorganic Chemistry*; University Science Books: Sausalito, CA, 2000.

(51)   Hammann, B. A.; Kast, M. G.; Plassmeyer, P. N.; Ma, Z. L.; Woods, K. N.; Keszler, D. A.; Page, C. J.; Boettcher, S. W.; Hayes, S. E. Elucidation of Structure-Property Relationships in Aqueous-Processed Aluminum Oxide Thin Films: Insights from Solid-State NMR and Dielectric Response. *Chem. Mater.* **2018**, submitted for publication.

(52)   Pauling, L. The Principles Determining the Structure of Complex Ionic Crystals. *J. Am. Chem. Soc.* **1929**, *51*, 1010–1026.

(53)   Zachariasen, W. H. The Atomic Arrangement in Glass. *J. Am. Chem. Soc.* **1932**, *196*, 3841–3851.

(54)   Thimsen, E.; Biswas, S.; Lo, C. S.; Biswas, P. Predicting the Band Structure of Mixed Transition Metal Oxides: Theory and Experiment. *J. Phys. Chem. C* **2009**, *113*, 2014–2021.

(55)   Dunitz, J. D.; Orgel, L. E. Electronic Properties of Transition-Metal Oxides-II. **1957**, *3*, 318–323.

(56)   Gao, X.; Wachs, I. E. Investigation of Surface Structures of Supported Vanadium Oxide Catalysts by UV−vis−NIR Diffuse Reflectance Spectroscopy. *J. Phys. Chem. B* **2000**, *104*, 1261–1268.

(57)   Akl, A. A. Effect of Solution Molarity on the Characteristics of Vanadium Pentoxide Thin Film. *Appl. Surf. Sci.* **2006**, *252*, 8745–8750.

(58)   Lee, C.-H.; Lin, T.-S.; Mou, C.-Y. Preparation and Characterization of Vanadium Oxide Species Supported on Mesoporous Silica for the Hydroxylation of Benzene. *J. Phys. Chem. C* **2007**, *111*, 3873–3882.

(59)   Schweitzer, G. K.; Pesterfield, L. L. *The Aqueous Chemistry of the Elements*; Oxford University Press: New York, 2009.

(60)   Peterson, M. L.; Brown, G. E.; Parks, G. A.; Stein, C. L. Differential Redox and Sorption of Cr(III/VI) on Natural Silicate and Oxide Minerals: EXAFS and XANES Results. *Geochim. Cosmochim. Acta* **1997**, *61*, 3399–3412.

(61)   Shriver, D.; Atkins, P. *Shriver & Atkins' Inorganic Chemistry*, 5th ed.; W. H. Freeman and Company: New York, 2009.

(62)   Murata, T.; Torisaka, M.; Takebe, H.; Morinaga, K. Compositional Dependence of the Valency State of Cr Ions in Oxide Glasses. *J. Non. Cryst. Solids* **1997**, *220*, 139–146.

(63)   Bondioli, F.; Ferrari, A. M.; Leonelli, C.; Manfredini, T.; Linati, L.; Mustarelli, P. Reaction Mechanism in Alumina/chromia (Al_2O_3-Cr_2O_3) Solid Solutions Obtained by Coprecipitation. *J. Am. Ceram. Soc.* **2000**, *83*, 2036–2040.

(64)   Gaudry, É.; Sainctavit, P.; Juillot, F.; Bondioli, F.; Ohresser, P.; Letard, I. From

the Green Color of Eskolaite to the Red Color of Ruby: An X-Ray Absorption Spectroscopy Study. *Phys. Chem. Miner.* **2006**, *32*, 710–720.

(65) Duret, A.; Grätzel, M. Visible Light-Induced Water Oxidation on Mesoscopic α-Fe_2O_3 Films Made by Ultrasonic Spray Pyrolysis. *J. Phys. Chem. B* **2005**, *109*, 17184–17191.

(66) Shinde, S. S.; Bansode, R. A.; Bhosale, C. H.; Rajpure, K. Y. Physical Properties of Hematite α-Fe_2O_3 Thin Films: Application to Photoelectrochemical Solar Cells. *J. Semicond.* **2011**, *32*, No. 013001.

(67) Biesinger, M. C.; Payne, B. P.; Grosvenor, A. P.; Lau, L. W. M.; Gerson, A. R.; Smart, R. S. C. Resolving Surface Chemical States in XPS Analysis of First Row Transition Metals, Oxides and Hydroxides: Cr, Mn, Fe, Co and Ni. *Appl. Surf. Sci.* **2011**, *257*, 2717–2730.

(68) Chalmin, E.; Farges, F.; Brown, G. E. A Pre-Edge Analysis of Mn K-Edge XANES Spectra to Help Determine the Speciation of Manganese in Minerals and Glasses. *Contrib. to Mineral. Petrol.* **2009**, *157*, 111–126.

(69) Eisenberger, P.; Brown, G. S. The Study of Disordered Systems by EXAFS: Limitations. *Solid State Commun.* **1979**, *29*, 481–484.

(70) McKeown, D. A.; Kot, W. K.; Gan, H.; Pegg, I. L. X-Ray Absorption Studies of Manganese Valence and Local Environment in Borosilicate Waste Glasses. *J. Non. Cryst. Solids* **2003**, *328*, 71–89.

(71) Hålenius, U.; Bosi, F.; Skogby, H. Galaxite, $MnAl_2O_4$, a Spectroscopic Standard for Tetrahedrally Coordinated Mn^{2+} in Oxygen-Based Mineral Structures. *Am. Mineral.* **2007**, *92*, 1225–1231.

(72) Smith, W. L.; Hobson, A. D. The Structure of Cobalt Oxide, Co_3O_4. *Acta Crystallogr. Sect. B Struct. Crystallogr. Cryst. Chem.* **1973**, *29*, 362–363.

(73) Rangappa, D.; Naka, T.; Kondo, A.; Ishii, M.; Kobayashi, T.; Adschiri, T. Transparent $CoAl_2O_4$ Hybrid Nano Pigment by Organic Ligand-Assisted Supercritical Water. *J. Am. Chem. Soc.* **2007**, *129*, 11061–11066.

(74) Cheng, C.-S.; Serizawa, M.; Sakata, H.; Hirayama, T. Electrical Conductivity of Co_3O_4 Films Prepared by Chemical Vapour Deposition. *Mater. Chem. Phys.* **1998**, *53*, 225–230.

(75) Gulino, A.; Fiorito, G.; Fragala, I. Deposition of Thin Films of Cobalt Oxides by MOCVD. *J. Mater. Chem.* **2003**, *13*, 861–865.

(76) Mahmoud, S. A.; Akl, A. A.; Kamal, H.; Abdel-Hady, K. Opto-Structural, Electrical and Electrochromic Properties of Crystalline Nickel Oxide Thin Films Prepared by Spray Pyrolysis. *Phys. B Condens. Matter* **2002**, *311*, 366–375.

(77) Kamal, H.; Elmaghraby, E. K.; Ali, S. A.; Abdel-Hady, K. Characterization of Nickel Oxide Films Deposited at Different Substrate Temperatures Using Spray

Pyrolysis. *J. Cryst. Growth* **2004**, *262*, 424–434.

(78) Praliaud, H.; Mikhailenko, S.; Chajar, Z.; Primet, M. Surface and Bulk Properties of Cu-ZSM-5 and Cu/Al$_2$O$_3$ Solids during Redox Treatments. Correlation with the Selective Reduction of Nitric Oxide by Hydrocarbons. *Appl. Catal. B Environ.* **1998**, *16*, 359–374.

(79) Mindru, I.; Gingasu, D.; Patron, L.; Marinescu, G.; Calderon-Moreno, J. M.; Preda, S.; Oprea, O.; Nita, S. Copper Aluminate Spinel by Soft Chemical Routes. *Ceram. Int.* **2016**, *42*, 154–164.

(80) Koffyberg, F. P.; Benko, F. A. A Photoelectrochemical Determination of the Position of the Conduction and Valence Band Edges of P-Type CuO. *J. Appl. Phys.* **1982**, *53*, 1173–1177.

(81) Marabelli, F.; Parravicini, G. B.; Salghetti-Drioli, F. Optical Gap of CuO. *Phys. Rev. B* **1995**, *52*, 1433–1436.

(82) Meyer, B. K.; Polity, A.; Reppin, D.; Becker, M.; Hering, P.; Klar, P. J.; Sander, T.; Reindl, C.; Benz, J.; Eickhoff, M.; et al. Binary Copper Oxide Semiconductors: From Materials towards Devices. *Phys. Status Solidi* **2012**, *249*, 1487–1509.

(83) Anufrienko, V. F.; Yashnik, S. A.; Bulgakov, N. N.; Larina, T. V.; Vasenin, N. T.; Ismagilov, Z. R. A Study of Linear Copper Oxide Structures in the Channels of the ZSM-5 Zeolite by Electronic Diffuse Reflectance Spectroscopy. *Dokl. Phys. Chem.* **2003**, *392*, 207–211.

(84) Miron, I.; Enache, C.; Vasile, M.; Grozescu, I. Optical Properties of ZnAl$_2$O$_4$ Nanomaterials Obtained by the Hydrothermal Method. *Phys. Scr.* **2012**, *T149*, 14064.

(85) Hoffman, R. *Solids and Surfaces: A Chemist's View of Bonding in Extended Structures*, 1st ed.; Wiley-VCH Inc.: New York, 1988.

(86) Liu, Z.; Zhu, J.; Li, J.; Ma, L.; Woo, S. I. Novel Mn-Ce-Ti Mixed-Oxide Catalyst for the Selective Catalytic Reduction of NO$_x$ with NH$_3$. *ACS Appl. Mater. Interfaces* **2014**, *6*, 14500–14508.

(87) Zhang, C.; Fagan, R. D.; Smith, R. D. L.; Moore, S. A.; Berlinguette, C. P.; Trudel, S. Mapping the Performance of Amorphous Ternary Metal Oxide Water Oxidation Catalysts Containing Aluminium. *J. Mater. Chem. A* **2015**, *3*, 756–761.

(88) Kim, H. S.; Park, J. S.; Jeong, H. K.; Son, K. S.; Kim, T. S.; Seon, J. B.; Lee, E.; Chung, J. G.; Kim, D. H.; Ryu, M.; et al. Density of States-Based Design of Metal Oxide Thin-Film Transistors for High Mobility and Superior Photostability. *ACS Appl. Mater. Interfaces* **2012**, *4*, 5416–5421.

(89) Grzybowska, B.; Słoczyński, J.; Grabowski, R.; Wcisło, K.; Kozłowska, A.; Stoch, J.; Zieliński, J. Chromium Oxide/Alumina Catalysts in Oxidative Dehydrogenation of Isobutane. *J. Catal.* **1998**, *178*, 687–700.

(90) Rida, K.; Benabbas, A.; Bouremmad, F.; Peña, M. A.; Martínez-Arias, A. Surface Properties and Catalytic Performance of $La_{1-x}Sr_xCrO_3$ Perovskite-Type Oxides for CO and C_3H_6 Combustion. *Catal. Commun.* **2006**, *7*, 963–968.

(91) Smith, J.; Zeng, L.; Khanal, R.; Stallings, K.; Facchetti, A.; Medvedeva, J. E.; Bedzyk, M. J.; Marks, T. J. Cation Size Effects on the Electronic and Structural Properties of Solution-Processed In–X–O Thin Films. *Adv. Electron. Mater.* **2015**, *1*, 1–11.

(92) Choi, C.-H.; Han, S.-Y.; Su, Y.-W.; Fang, Z.; Lin, L.-Y.; Cheng, C.-C.; Chang, C. Fabrication of High-Performance, Low-Temperature Solution Processed Amorphous Indium Oxide Thin-Film Transistors Using a Volatile Nitrate Precursor. *J. Mater. Chem. C* **2015**, *3*, 854–860.

CHAPTER III

(1) Lewis, N. S.; Nocera, D. G. *Proc. Natl. Acad. Sci.* **2006**, *103*, 15729–15735.

(2) Ursua, A.; Gandia, L. M.; Sanchis, P. *Proc. IEEE* **2012**, *100*, 410–426.

(3) Pinaud, B. A.; Benck, J. D.; Seitz, L. C.; Forman, A. J.; Chen, Z.; Deutsch, T. G.; James, B. D.; Baum, K. N.; Baum, G. N.; Ardo, S.; Wang, H.; Miller, E.; Jaramillo, T. F. *Energy Environ. Sci.* **2013**, *6*, 1983–2002.

(4) Walter, M. G.; Warren, E. L.; McKone, J. R.; Boettcher, S. W.; Mi, Q.; Santori, E. A.; Lewis, N. S. *Chem. Rev.* **2010**, *110*, 6446–6473.

(5) Trotochaud, L.; Boettcher, S. W. *Scr. Mater.* **2014**, *74*, 25–32.

(6) Rossmeisl, J.; Logadottir, A.; Nørskov, J. K. *Chem. Phys.* **2005**, *319*, 178–184.

(7) Galán-Mascarós, J. R. *ChemElectroChem* **2015**, *2*, 37–50.

(8) Dau, H.; Limberg, C.; Reier, T.; Risch, M.; Roggan, S.; Strasser, P. *ChemCatChem* **2010**, *2*, 724–761.

(9) Rossmeisl, J.; Qu, Z.-W.; Zhu, H.; Kroes, G.-J.; Nørskov, J. K. *J. Electroanal. Chem.* **2007**, *607*, 83–89.

(10) Man, I. C.; Su, H.-Y.; Calle-Vallejo, F.; Hansen, H. A.; Martínez, J. I.; Inoglu, N. G.; Kitchin, J.; Jaramillo, T. F.; Nørskov, J. K.; Rossmeisl, J. *ChemCatChem* **2011**, *3*, 1159–1165.

(11) Ruetschi, P.; Delahay, P. *J. Chem. Phys.* **1955**, *23*, 556–560.

(12) Sabatier, F. *La catalyse en chimie organique*; Berauge: Paris, 1920; pp. 48-57.

(13) Trotochaud, L.; Ranney, J. K.; Williams, K. N.; Boettcher, S. W. *J. Am. Chem. Soc.* **2012**, *134*, 17253–17261.

(14) Trotochaud, L.; Young, S. L.; Ranney, J. K.; Boettcher, S. W. *J. Am. Chem. Soc.* **2014**, *136*, 6744–6753.

(15) Burke, M. S.; Kast, M. G.; Trotochaud, L.; Smith, A. M.; Boettcher, S. W. *J. Am. Chem. Soc.* **2015**, *137*, 3638–3648.

(16) Smith, A. M.; Trotochaud, L.; Burke, M. S.; Boettcher, S. W. *Chem. Commun.* **2015**, *51*, 5261–5263.

(17) Hong, W. T.; Risch, M.; Stoerzinger, K. A.; Grimaud, A.; Suntivich, J.; Shao-Horn, Y. *ENERGY Environ. Sci.* **2015**, *8*, 1404–1427.

(18) Suntivich, J.; May, K. J.; Gasteiger, H. A.; Goodenough, J. B.; Shao-Horn, Y. *Science* **2011**, *334*, 1383–1385.

(19) Smith, R. D. L.; Prévot, M. S.; Fagan, R. D.; Zhang, Z.; Sedach, P. A.; Siu, M. K. J.; Trudel, S.; Berlinguette, C. P. *Science* **2013**, *340*, 60–63.

(20) Matsumoto, Y.; Sato, E. *Mater. Chem. Phys.* **1986**, *14* (5), 397–426.

(21) Burke, M. S.; Enman, L. J.; Batchellor, A. S.; Zou, S.; Boettcher, S. W. *Chem. Mater.* **2015**, *27* (22), 7549–7558.

(22) Burke, M. S.; Zou, S.; Enman, L. J.; Kellon, J. E.; Gabor, C. A.; Pledger, E.; Boettcher, S. W. *J. Phys. Chem. Lett.* **2015**, *6*, 3737–3742.

(23) Batchellor, A. S.; Boettcher, S. W. *ACS Catal.* **2015**, *5*, 6680–6689.

(24) Lu, X.; Zhao, C. *Nat. Commun.* **2015**, *6*, No. 6616.

(25) Ma, W.; Ma, R.; Wang, C.; Liang, J.; Liu, X.; Zhou, K.; Sasaki, T. *ACS Nano* **2015**, *9*, 1977–1984.

(26) Hunter, B. M.; Blakemore, J. D.; Deimund, M.; Gray, H. B.; Winkler, J. R.; Müller, A. M. *J. Am. Chem. Soc.* **2014**, *136*, 13118–13121.

(27) Gong, M.; Li, Y.; Wang, H.; Liang, Y.; Wu, J. Z.; Zhou, J.; Wang, J.; Regier, T.; Wei, F.; Dai, H. *J. Am. Chem. Soc.* **2013**, *135*, 8452–8455.

(28) Corrigan, D. A.; Bendert, R. M. *J. Electrochem. Soc.* **1989**, *136*, 723–728.

(29) Landon, J.; Demeter, E.; İnoğlu, N.; Keturakis, C.; Wachs, I. E.; Vasić, R.; Frenkel, A. I.; Kitchin, J. R. *ACS Catal.* **2012**, *2*, 1793–1801.

(30) Louie, M. W.; Bell, A. T. *J. Am. Chem. Soc.* **2013**, *135* (33), 12329–12337.

(31) Cordoba, S. I.; Carbonio, R. E.; Teijelo, M. L.; Macagno, V. A. *Electrochim. Acta* **1986**, *31*, 1321–1332.

(32) Lu, P. W. T.; Srinivasan, S. *J. Electrochem. Soc.* **1978**, *125*, 265–270.

(33) McCrory, C. C. L.; Jung, S.; Ferrer, I. M.; Chatman, S. M.; Peters, J. C.; Jaramillo, T. F. *J. Am. Chem. Soc.* **2015**, *137*, 4347–4357.

(34) McCrory, C. C. L.; Jung, S.; Peters, J. C.; Jaramillo, T. F. *J. Am. Chem. Soc.* **2013**, *135*, 16977–16987.

(35) Qian, L.; Lu, Z.; Xu, T.; Wu, X.; Tian, Y.; Li, Y.; Huo, Z.; Sun, X.; Duan, X. *Adv. Energy Mater.* **2015**, *5*, No. 1500245.

(36) Niu, K.-Y.; Lin, F.; Jung, S.; Fang, L.; Nordlund, D.; McCrory, C. C. L.; Weng, T.-C.; Ercius, P.; Doeff, M. M.; Zheng, H. *Nano Lett.* **2015**, *15*, 2498–2503.

(37) Haber, J. A.; Guevarra, D.; Jung, S.; Jin, J.; Gregoire, J. M. *ChemElectroChem* **2014**, *1*, 1613–1617.

(38) Diaz-Morales, O.; Ledezma-Yanez, I.; Koper, M. T. M.; Calle-Vallejo, F. *ACS Catal.* **2015**, *5*, 5380–5387.

(39) Yeo, B. S.; Bell, A. T. *J. Phys. Chem. C* **2012**, *116*, 8394–8400.

(40) Lyons, M. E. G.; Brandon, M. P. *J. Electroanal. Chem.* **2010**, *641*, 119–130.

(41) Miles, M. H. *J. Electroanal. Chem. Interfacial Electrochem.* **1975**, *60*, 89–96.

(42) Dincă, M.; Surendranath, Y.; Nocera, D. G. *Proc. Natl. Acad. Sci. U. S. A.* **2010**, *107*, 10337–10341.

(43) Corrigan, D. A. *J. Electrochem. Soc.* **1987**, *134*, 377–384.

(44) Lu, P. W. T.; Srinivasan, S. *J. Electrochem. Soc.* **1978**, *125*, 1416–1422.

(45) Wehrens-Dijksma, M.; Notten, P. H. L. *Electrochim. Acta* **2006**, *51*, 3609–3621.

(46) Godwin, I. J.; Lyons, M. E. G. *Electrochem. Commun.* **2013**, *32*, 39–42.

(47) Klaus, S.; Cai, Y.; Louie, M. W.; Trotochaud, L.; Bell, A. T. *J. Phys. Chem. C* **2015**, *119*, 7243–7254.

(48) Haber, J. A.; Xiang, C.; Guevarra, D.; Jung, S.; Jin, J.; Gregoire, J. M. *ChemElectroChem* **2014**, *1*, 524–528.

(49) Corrigan, D. A.; Conell, R. S.; Fierro, C. A.; Scherson, D. A. *J. Phys. Chem.* **1987**, *91*, 5009–5011.

(50) Friebel, D.; Louie, M. W.; Bajdich, M.; Sanwald, K. E.; Cai, Y.; Wise, A. M.; Cheng, M.-J.; Sokaras, D.; Weng, T.-C.; Alonso-Mori, R.; Davis, R. C.; Bargar, J. R.; Nørskov, J. K.; Nilsson, A.; Bell, A. T. *J. Am. Chem. Soc.* **2015**, *137*, 1305–1313.

(51) Zou, S.; Burke, M. S.; Kast, M. G.; Fan, J.; Danilovic, N.; Boettcher, S. W. *Chem. Mater.* **2015**, *27*, 8011–8020.

(52) Chen, J. Y. C.; Dang, L.; Liang, H.; Bi, W.; Gerken, J. B.; Jin, S.; Alp, E. E.; Stahl, S. S. *J. Am. Chem. Soc.* **2015**, *137*, 15090–15093.

(53) Oliver-Tolentino, M. A.; Vázquez-Samperio, J.; Manzo-Robledo, A.; González-Huerta, R. de G.; Flores-Moreno, J. L.; Ramírez-Rosales, D.; Guzmán-Vargas, A. *J. Phys. Chem. C* **2014**, *118*, 22432–22438.

(54) Seitz, L. C.; Pinaud, B. A.; Nordlund, D.; Jaramillo, T. F. *ECS Trans.* **2013**, *58*, 285–291.

(55) Seitz, L. C.; Pinaud, B. A.; Nordlund, D.; Gorlin, Y.; Gallo, A.; Jaramillo, T. F. *J. Electrochem. Soc.* **2015**, *162*, H841–H846.

(56)   Trasatti, S.; Petrii, O. A. *J. Electroanal. Chem.* **1992**, *327*, 353–376.

(57)   Sauerbrey, G. *Zeitschrift für Phys. A Hadron. Nucl.* **1959**, *155*, 206–222.

(58)   Klaus, S.; Louie, M. W.; Trotochaud, L.; Bell, A. T. *J. Phys. Chem. C* **2015**, *119*, 18303–18316.

(59)   Pourbaix, M. *Atlas of Electrochemical Equilibria in Aqueous Solutions*; Pergamon Press: Oxford, 1966; pp. 194.

(60)   Schweitzer, G. K.; Pesterfield, L. L. *The Aqueous Chemistry of the Elements*; Oxford University Press, 2009; pp. 269.

(61)   Balasubramanian, M.; Melendres, C. A.; Mansour, A. N. *J. Electrochem. Soc.* **1999**, *146*, 607–614.

(62)   Balasubramanian, M.; Melendres, C. A.; Mansour, A. N. *Thin Solid Films* **1999**, *347*, 178–183.

(63)   Haber, J. A.; Anzenburg, E.; Yano, J.; Kisielowski, C.; Gregoire, J. M. *Adv. Energy Mater.* **2015**, *5*, No.1402307.

(64)   Moulder, J. F.; Stickle, W. F.; Sobol, P. E.; Bomben, K. D. *Handbook of X-ray photoelectron spectroscopy: a reference book of standard spectra for identification and interpretation of XPS data*; Chastain, J., Ed.; Perkin-Elmer: Eden Prairie, MN, 1992; pp. 45

(65)   Klaus, S.; Trotochaud, L.; Cheng, M.-J.; Head-Gordon, M.; Bell, A. T. *ChemElectroChem* **2016**, *3*, 66–73.

(66)   Doyle, R. L.; Godwin, I. J.; Brandon, M. P.; Lyons, M. E. G. *Phys. Chem. Chem. Phys.* **2013**, *15*, 13737–13783.

(67)   Bard, A. J.; Faulkner, L. R. *Electrochemical Methods: Fundamentals and Applications*, second.; John Wiley & Sons: New York, 2001; pp. 108-115.

(68)   Trześniewski, B. J.; Diaz-Morales, O.; Vermaas, D. A.; Longo, A.; Bras, W.; Koper, M. T. M.; Smith, W. A. *J. Am. Chem. Soc.* **2015**, *137*, 15112–15121.

(69)   Tung, C.-W.; Hsu, Y.-Y.; Shen, Y.-P.; Zheng, Y.; Chan, T.-S.; Sheu, H.-S.; Cheng, Y.-C.; Chen, H. M. *Nat. Commun.* **2015**, *6*, No. 8106.

(70)   Bergmann, A.; Martinez-Moreno, E.; Teschner, D.; Chernev, P.; Gliech, M.; de Araújo, J. F.; Reier, T.; Dau, H.; Strasser, P. *Nat. Commun.* **2015**, *6*, No. 8625.

CHAPTER IV

(1)   Lewis, N. S. *Science* **2016**, *351*, aad1920.

(2)   Pinaud, B. A.; Benck, J. D.; Seitz, L. C.; Forman, A. J.; Chen, Z.; Deutsch, T. G.; James, B. D.; Baum, K. N.; Baum, G. N.; Ardo, S.; Wang, H.; Miller, E.; Jaramillo, T. F. *Energy Environ. Sci.* **2013**, *6*, 1983.

(3)   Burke, M. S.; Enman, L. J.; Batchellor, A. S.; Zou, S.; Boettcher, S. W. *Chem. Mater.* **2015**, *27*, 7549.

(4)   Armaroli, N.; Balzani, V. *Chem. - A Eur. J.* **2016**, *22*, 32.

(5)   Zou, S.; Burke, M. S.; Kast, M. G.; Fan, J.; Danilovic, N.; Boettcher, S. W. *Chem. Mater.* **2015**, *27*, 8011.

(6)   Burke, M. S.; Zou, S.; Enman, L. J.; Kellon, J. E.; Gabor, C. A.; Pledger, E.; Boettcher, S. W. *J. Phys. Chem. Lett.* **2015**, *6*, 3737.

(7)   Lee, J.; Lee, H.; Lim, B. *J. Ind. Eng. Chem.* **2018**, *58*, 100.

(8)   Luo, W.; Jiang, C.; Li, Y.; Shevlin, S. A.; Han, X.; Qiu, K.; Cheng, Y.; Guo, Z.; Huang, W.; Tang, J. *J. Mater. Chem. A* **2017**, *5*, 2021.

(9)   Vassalini, I.; Borgese, L.; Mariz, M.; Polizzi, S.; Aquilanti, G.; Ghigna, P.; Sartorel, A.; Amendola, V.; Alessandri, I. *Angew. Chemie - Int. Ed.* **2017**, *56*, 6589.

(10)   Zhao, Q.; Li, D.; Gao, G.; Yuan, W.; Hao, G.; Li, J. *Int. J. Hydrogen Energy* **2016**, *41*, 17193.

(11)   Doyle, R. L.; Lyons, M. E. G. *J. Electrochem. Soc.* **2013**, *160*, H142.

(12)   Burke, M. S.; Kast, M. G.; Trotochaud, L.; Smith, A. M.; Boettcher, S. W. *J. Am. Chem. Soc.* **2015**, *137*, 3638.

(13)   Trotochaud, L.; Young, S. L.; Ranney, J. K.; Boettcher, S. W. *J. Am. Chem. Soc.* **2014**, *136*, 6744.

(14)   Benck, J. D.; Pinaud, B. A.; Gorlin, Y.; Jaramillo, T. F. *PLoS One* **2014**, *9*, 1.

(15)   Klaus, S.; Trotochaud, L.; Cheng, M.-J.; Head-Gordon, M.; Bell, A. T. *ChemElectroChem* **2016**, *3*, 66.

(16)   Chakthranont, P.; Kibsgaard, J.; Gallo, A.; Park, J.; Mitani, M.; Sokaras, D.; Kroll, T.; Sinclair, R.; Mogensen, M. B.; Jaramillo, T. F. *ACS Catal.* **2017**, *7*, 5399.

(17)   Frydendal, R.; Busch, M.; Halck, N. B.; Paoli, E. A.; Krtil, P.; Chorkendorff, I.; Rossmeisl, J. *ChemCatChem* **2015**, *7*, 149.

(18)   Hou, Y.; Liu, Y.; Gao, R.; Li, Q.; Guo, H.; Goswami, A.; Zboril, R.; Gawande, M. B.; Zou, X. *ACS Catal.* **2017**, *7*, 7038.

(19)   Kim, H.; Kim, Y.; Noh, Y.; Kim, W. B. *Dalt. Trans.* **2016**, *45*, 13686.

(20)   Sidhureddy, B.; Thiruppathi, A. R.; Chen, A. *J. Electroanal. Chem.* **2017**, *794*, 28.

(21)   Strickler, A. L.; Escudero-Escribano, M.; Jaramillo, T. F. *Nano Lett.* **2017**, *17*, 6040.

(22)   Qu, Q.; Zhang, J.-H.; Wang, J.; Li, Q.-Y.; Xu, C.-W.; Lu, X. *Sci. Rep.* **2017**, *7*, 41542.

(23) Yu, L.; Zhou, H.; Sun, J.; Qin, F.; Yu, F.; Bao, J.; Yu, Y.; Chen, S.; Ren, Z. *Energy Environ. Sci.* **2017**, *10*, 1820.

(24) Zhou, Y.; Zeng, H. C. *J. Phys. Chem. C* **2016**, *120*, 29348.

(25) Sayeed, M. A.; Herd, T.; O'Mullane, A. P. *J. Mater. Chem. A* **2016**, *4*, 991.

(26) Yeo, B. S.; Bell, A. T. *J. Phys. Chem. C* **2012**, *116*, 8394.

(27) Yeo, B. S.; Bell, A. T. *J. Am. Chem. Soc.* **2011**, *133*, 5587.

(28) Gorlin, Y.; Chung, C. J.; Benck, J. D.; Nordlund, D.; Seitz, L.; Weng, T. C.; Sokaras, D.; Clemens, B. M.; Jaramillo, T. F. *J. Am. Chem. Soc.* **2014**, *136*, 4920.

(29) Seitz, L. C.; Hersbach, T. J. P.; Nordlund, D.; Jaramillo, T. F. *J. Phys. Chem. Lett.* **2015**, *6*, 4178.

(30) Corrigan, D. A. *J. Electrochem. Soc.* **1987**, *134*, 377.

(31) Stevens, M. B.; Enman, L. J.; Batchellor, A. S.; Cosby, M. R.; Vise, A. E.; Trang, C. D. M.; Boettcher, S. W. *Chem. Mater.* **2017**, *29*, 120.

(32) Roger, I.; Symes, M. D. *J. Am. Chem. Soc.* **2015**, *137*, 13980.

(33) Gorlin, M.; De Araujo, J. F.; Schmies, H.; Bernsmeier, D.; Dresp, S.; Gliech, M.; Jusys, Z.; Chernev, P.; Kraehnert, R.; Dau, H.; Strasser, P. *J. Am. Chem. Soc.* **2017**, *139*, 2070.

(34) Ng, J. W. D.; García-Melchor, M.; Bajdich, M.; Chakthranont, P.; Kirk, C.; Vojvodic, A.; Jaramillo, T. F. *Nat. Energy* **2016**, *1*, 1.

(35) Frydendal, R.; Seitz, L. C.; Sokaras, D.; Weng, T. C.; Nordlund, D.; Chorkendorff, I.; Stephens, I. E. L.; Jaramillo, T. F. *Electrochim. Acta* **2017**, *230*, 22.

(36) Lu, A.; Peng, D. L.; Chang, F.; Skeete, Z.; Shan, S.; Sharma, A.; Luo, J.; Zhong, C. J. *ACS Appl. Mater. Interfaces* **2016**, *8*, 20082.

CHAPTER V

[1] M. S. Burke, L. J. Enman, A. S. Batchellor, S. Zou, S. W. Boettcher, *Chem. Mater.* **2015**, *27*, 7549–7558.

[2] N. Armaroli, V. Balzani, *Chem. - A Eur. J.* **2016**, *22*, 32–57.

[3] J. H. Montoya, L. C. Seitz, P. Chakthranont, A. Vojvodic, T. F. Jaramillo, J. K. Nørskov, *Nat. Mater.* **2016**, *16*, 70–81.

[4] L. Trotochaud, J. K. Ranney, K. N. Williams, S. W. Boettcher, *J. Am. Chem. Soc.* **2012**, *134*, 17253–61.

[5] M. S. Burke, S. Zou, L. J. Enman, J. E. Kellon, C. A. Gabor, E. Pledger, S. W. Boettcher, *J. Phys. Chem. Lett.* **2015**, *6*, 3737–3742.

[6] D. Friebel, M. W. Louie, M. Bajdich, K. E. Sanwald, Y. Cai, A. M. Wise, M.-J. Cheng, D. Sokaras, T.-C. Weng, R. Alonso-Mori, et al., *J. Am. Chem. Soc.* **2015**, *137*, 1305–1313.

[7] M. Gorlin, J. F. De Araujo, H. Schmies, D. Bernsmeier, S. Dresp, M. Gliech, Z. Jusys, P. Chernev, R. Kraehnert, H. Dau, et al., *J. Am. Chem. Soc.* **2017**, *139*, 2070–2082.

[8] M. Görlin, P. Chernev, J. Ferreira de Araújo, T. Reier, S. Dresp, B. Paul, R. Krähnert, H. Dau, P. Strasser, *J. Am. Chem. Soc.* **2016**, *138*, 5603–5614.

[9] R. D. L. Smith, C. Pasquini, S. Loos, P. Chernev, K. Klingan, P. Kubella, M. R. Mohammadi, D. Gonzalez-Flores, H. Dau, *Nat. Commun.* **2017**, *8*, 2022.

[10] M. K. Bates, Q. Jia, H. Doan, W. Liang, S. Mukerjee, *ACS Catal.* **2016**, *6*, 155–161.

[11] L. Gong, X. Y. E. Chng, Y. Du, S. Xi, B. S. Yeo, *ACS Catal.* **2018**, *8*, 807–814.

[12] N. Li, D. K. Bediako, R. G. Hadt, D. Hayes, T. J. Kempa, F. von Cube, D. C. Bell, L. X. Chen, D. G. Nocera, *Proc. Natl. Acad. Sci.* **2017**, *114*, 1486–1491.

[13] J. Y. C. Chen, L. Dang, H. Liang, W. Bi, J. B. Gerken, S. Jin, E. E. Alp, S. S. Stahl, *J. Am. Chem. Soc.* **2015**, *137*, 15090–15093.

[14] B. M. Hunter, N. B. Thompson, A. M. Müller, G. R. Rossman, M. G. Hill, J. R. Winkler, H. B. Gray, *Joule* **2018**, 747–763.

[15] M. S. Burke, M. G. Kast, L. Trotochaud, A. M. Smith, S. W. Boettcher, *J. Am. Chem. Soc.* **2015**, *137*, 3638–3648.

[16] L. Trotochaud, S. L. Young, J. K. Ranney, S. W. Boettcher, *J. Am. Chem. Soc.* **2014**, *136*, 6744–53.

[17] B. M. Hunter, W. Hieringer, J. Winkler, H. B. Gray, A. M. Müller, *Energy Environ. Sci.* **2016**, *23*, 1–22.

[18] M. B. Stevens, C. D. M. Trang, L. J. Enman, J. Deng, S. W. Boettcher, *J. Am. Chem. Soc.* **2017**, *139*, 11361–11364.

[19] H. Yang, Y. Liu, S. Luo, Z. Zhao, X. Wang, Y. Luo, Z. Wang, J. Jin, J. Ma, *ACS Catal.* **2017**, *7*, 5557–5567.

[20] F. Song, X. Hu, *Nat. Commun.* **2014**, *5*, 4477.

[21] J. Fester, M. García-Melchor, A. S. Walton, M. Bajdich, Z. Li, L. Lammich, A. Vojvodic, J. V. Lauritsen, L. R. Merte, M. A. Henderson, et al., *Nat. Commun.* **2017**, *8*, 14169.

[22] B. Hunter, J. Winkler, H. Gray, *Molecules* **2018**, *23*, 903.

[23] M. Favaro, J. Yang, S. Nappini, E. Magnano, F. M. Toma, E. J. Crumlin, J. Yano, I. D. Sharp, *J. Am. Chem. Soc.* **2017**, *139*, 8960–8970.

[24] E. Fabbri, M. Nachtegaal, T. Binninger, X. Cheng, B. J. Kim, J. Durst, F. Bozza, T. Graule, R. Schäublin, L. Wiles, et al., *Nat. Mater.* **2017**, *16*, 925–931.

[25] L. Calvillo, F. Carraro, O. Vozniuk, V. Celorrio, L. Nodari, A. E. Russell, D. Debellis, D. Fermin, F. Cavani, S. Agnoli, et al., *J. Mater. Chem. A* **2018**, *6*, 7034-7041.

[26] B. Ravel, M. Newville, *J. Synchrotron Radiat.* **2005**, *12*, 537–541.

[27] B. Ravel, *J. Synchrotron Radiat.* **2001**, *8*, 314–316.

[28] M. Newville, *J. Synchrotron Radiat.* **2001**, *8*, 322–324.

[29] M. Deliens, H. Goethals, *Miner. Mag.* **1973**, *39*, 152–157.

[30] D. Gonzáles-Flores, K. Klingan, P. Chernev, S. Loos, M. R. Mohammadi, C. Pasquini, P. Kubella, I. Zaharieva, R. Smith, H. Dau, *Sustain. Energy Fuels* **2018**, DOI 10.1039/C8SE00114F.

[31] J. G. McAlpin, Y. Surendranath, M. Dinca, T. A. Stich, S. A. Stoian, W. H. Casey, D. G. Nocera, R. D. Britt, *J. Am. Chem. Soc.* **2010**, *132*, 6882–6883.

[32] R. G. Hadt, D. Hayes, C. N. Brodsky, A. M. Ullman, D. M. Casa, M. H. Upton, D. G. Nocera, L. X. Chen, *J. Am. Chem. Soc.* **2016**, *138*, 11017–11030.

[33] M. Balasubramanian, C. A. Melendres, S. Mini, *J. Phys* **2000**, *104*, 4300–4306.

[34] S. P. Cramer, T. K. Eccles, F. W. Kutzler, K. O. Hodgson, L. E. Mortenson, *J. Am. Chem. Soc.* **1976**, *98*, 1287–1288.

[35] R. L. Blake, R. E. Hessevick, T. Zoltai, L. W. Finger, *Am. Mineral.* **1966**, *51*, 123–129.

[36] H. Christensen, A. N. Christensen, U. Turpeinen, A. F. Andresen, O. Smidsrød, C.-O. Pontchour, P. Phavanantha, S. Pramatus, B. N. Cyvin, S. J. Cyvin, *Acta Chem. Scand.* **1978**, *32a*, 87–88.

[37] G. Kresse, J. Hafner, *Phys. Rev. B* **1993**, *47*, 558–561.

[38] G. Kresse, J. Furthmüller, *Comput. Mater. Sci.* **1996**, *6*, 15–50.

[39] S. Dudarev, G. Botton, *Phys. Rev. B - Condens. Matter Mater. Phys.* **1998**, *57*, 1505–1509.

[40] I. C. Man, H.-Y. Su, F. Calle-Vallejo, H. A. Hansen, J. I. Martínez, N. G. Inoglu, J. Kitchin, T. F. Jaramillo, J. K. Nørskov, J. Rossmeisl, *ChemCatChem* **2011**, *3*, 1159–1165.

[41] K. Momma, F. Izumi, *J. Appl. Crystallogr.* **2011**, *44*, 1272–1276.

APPENDIX A

(1)   Moulder, J. F.; Stickle, W. F.; Sobol, P. E.; Bomben, K. D. *Handbook of X-Ray Photoelectron Spectroscopy: A Reference Book of Standard Spectra for Identification and Interpretation of XPS Data*; Chastain, J., Ed.; Perkin-Elmer: Eden Prairie, MN, 1992.

(2)   Biesinger, M. C.; Lau, L. W. M.; Gerson, A. R.; Smart, R. S. C. Resolving Surface Chemical States in XPS Analysis of First Row Transition Metals, Oxides and Hydroxides: Sc, Ti, V, Cu and Zn. *Appl. Surf. Sci.* **2010**, *257*, 887–898.

(3)   Aronniemi, M.; Sainio, J.; Lahtinen, J. Chemical State Quantification of Iron and Chromium Oxides Using XPS: The Effect of the Background Subtraction Method. *Surf. Sci.* **2005**, *578*, 108–123.

(4)   Biesinger, M. C.; Brown, C.; Mycroft, J. R.; Davidson, R. D.; McIntyre, N. S. X-Ray Photoelectron Spectroscopy Studies of Chromium Compounds. *Surf. Interface Anal.* **2004**, *36*, 1550–1563.

(5)   Biesinger, M. C.; Payne, B. P.; Grosvenor, A. P.; Lau, L. W. M.; Gerson, A. R.; Smart, R. S. C. Resolving Surface Chemical States in XPS Analysis of First Row Transition Metals, Oxides and Hydroxides: Cr, Mn, Fe, Co and Ni. *Appl. Surf. Sci.* **2011**, *257*, 2717–2730.

(6)   Yamashita, T.; Hayes, P. Analysis of XPS Spectra of Fe^{2+} and Fe^{3+} Ions in Oxide Materials. *Appl. Surf. Sci.* **2008**, *254*, 2441–2449.

(7)   Biesinger, M. C.; Payne, B. P.; Lau, L. W. M.; Gerson, A.; Smart, R. S. C. X-Ray Photoelectron Spectroscopic Chemical State Quantification of Mixed Nickel Metal, Oxide and Hydroxide Systems. *Surf. Interface Anal.* **2009**, *41*, 324–332.

(8)   Ravel, B.; Newville, M. ATHENA, ARTEMIS, HEPHAESTUS: Data Analysis for X-Ray Absorption Spectroscopy Using IFEFFIT. *J. Synchrotron Radiat.* **2005**, *12*, 537–541.

(9)   Newville, M. IFEFFIT : Interactive XAFS Analysis and FEFF Fitting. *J. Synchrotron Radiat.* **2001**, *8*, 322–324.

APPENDIX B

(1)   Batchellor, A. S.; Boettcher, S. W. *ACS Catal.* **2015**, *5*, 6680–6689.

(2)   Corrigan, D. A.; Knight, S. L. *J. Electrochem. Soc.* **1989**, *136*, 613–619.

(3)   Mullins, D. R.; Overbury, S. H.; Huntley, D. R. *Surf. Sci.* **1998**, *409*, 307–319.

(4)   Wehrens-Dijksma, M.; Notten, P. H. L. *Electrochim. Acta* **2006**, *51*, 3609–3621.

APPENDIX D

[1]   M. S. Burke, M. G. Kast, L. Trotochaud, A. M. Smith, S. W. Boettcher, *J. Am. Chem. Soc.* **2015**, *137*, 3638–3648.

[2]   B. Ravel, M. Newville, *J. Synchrotron Radiat.* **2005**, *12*, 537–541.

[3]   B. Ravel, *J. Synchrotron Radiat.* **2001**, *8*, 314–316.

[4]   M. Newville, *J. Synchrotron Radiat.* **2001**, *8*, 322–324.

[5]   M. Deliens, H. Goethals, *Miner. Mag.* **1973**, *39*, 152–157.

[6]   G. Kresse, J. Hafner, *Phys. Rev. B* **1993**, *47*, 558–561.

[7]   G. Kresse, J. Furthmüller, *Comput. Mater. Sci.* **1996**, *6*, 15–50.

[8]   S. Dudarev, G. Botton, *Phys. Rev. B - Condens. Matter Mater. Phys.* **1998**, *57*, 1505–1509.

[9]   Y. F. Li, A. Selloni, *J. Phys. Chem. Lett.* **2014**, *5*, 3981–3985.

[10]   Y. Li, A. Selloni, *ACS Catal.* **2014**, *4*, 1148–1153.

[11]   A. J. Tkalych, K. Yu, E. A. Carter, *J. Phys. Chem. C* **2015**, *119*, 24315–24322.

[12]   V. Fidelsky, M. Caspary Toroker, *J. Phys. Chem. C* **2016**, *120*, 8104–8108.

[13]   J. Zaffran, M. Caspary Toroker, *J. Chem. Theory Comput.* **2016**, *12*, 3807–3812.

[14]   P. E. Blöchl, *Phys. Rev. B* **1994**, *50*, 17953–17979.

[15]   G. Kresse, D. Joubert, *Phys. Rev. B* **1999**, *59*, 1758–1775.

[16]   M. Casas-Cabanas, J. Canales-Vázquez, J. Rodríguez-Carvajal, M. R. Palacín, *J. Am. Chem. Soc.* **2007**, *129*, 5840–5842.

[17]   P. Oliva, J. Leonardi, J. F. Laurent, C. Delmas, J. J. Braconnier, M. Figlarz, F. Fievet, A. d. Guibert, *J. Power Sources* **1982**, *8*, 229–255.

[18]   R. G. Delaplane, J. A. Ibers, J. R. Ferraro, J. J. Rush, *J. Chem. Phys.* **1969**, *50*, 1920–1927.

[19]   J. Chen, A. Selloni, *J. Phys. Chem. C* **2013**, *117*, 20002–20006.

[20]   D. Friebel, M. W. Louie, M. Bajdich, K. E. Sanwald, Y. Cai, A. M. Wise, M.-J. Cheng, D. Sokaras, T.-C. Weng, R. Alonso-Mori, et al., *J. Am. Chem. Soc.* **2015**, *137*, 1305–1313.

[21]   I. C. Man, H.-Y. Su, F. Calle-Vallejo, H. A. Hansen, J. I. Martínez, N. G. Inoglu, J. Kitchin, T. F. Jaramillo, J. K. Nørskov, J. Rossmeisl, *ChemCatChem* **2011**, *3*, 1159–1165.

[22]   M. Bajdich, M. García-Mota, A. Vojvodic, J. K. Nørskov, A. T. Bell, *J. Am. Chem. Soc.* **2013**, *135*, 13521–13530.

[23] C. Hareli, M. C. Toroker, *J. Chem. Theory Comput.* **2018**, *14*, 2380–2385.

[24] M. C. Toroker, *J. Phys. Chem. C* **2014**, *118*, 23162–23167.